ALMA MATER STUDIORUM · UNIVERSITÀ DI BOLOGNA

DOTTORATO DI RICERCA IN FISICA
Ciclo XXX

Settore Concorsuale: 02/A1
Settore Scientifico Disciplinare: FIS/01

Experimental study of the time resolution for particle detectors based on MRPC, SiPM and UFSD technologies

Presentata da: Francesca Carnesecchi

Coordinatore Dottorato:
Prof.ssa Silvia Arcelli

Supervisore:
Prof.ssa Gilda Scioli
Co-Supervisore:
Dott. Rosario Nania

Esame finale anno 2018

Abstract

The work here presented describes in details an extensive study of the time resolution of various detectors. Precise time measurements are of fundamental importance both in particle and in medical physics; even more, an excellent time resolution (tens of ps) will be necessary for the next generation of colliders in high energy physics, facing also the challenging request of a high rate capability.
Several detectors have been studied, spanning several technologies from gaseous to silicon: Multigap Resistive Plate Chamber (MRPC), Silicon PhotoMultiplier (SiPM) and a new prototype of silicon detectors, the Ultra Fast Silicon Detector (UFSD). These studies have been performed both in a cosmic ray setup, at the INFN Bologna laboratories, and in a beam test setup, in the T10 and H8 beam lines at CERN. The *R&D* on time resolution for all the three technologies has been performed with different detector designs. The study showed promising results; indeed all the detectors reached a final time resolution smaller than 70 *ps*, with a minimum value of 35 *ps*. For the MRPC, an attempt to improve also the rate capability has been successfully realised. Moreover, a study based on data analysis has been performed for the ALICE TOF detector (based on the MRPC technology); possible degradations of the time resolution related to signals in two adjacent readout pads have been investigated and corrected, allowing an improvement of the final TOF time resolution.

Sommario

Il lavoro qui presentato riguarda uno studio approfondito sulla risoluzione temporale in cui sono stati presi in esame vari rivelatori. Elevate risoluzioni temporali sono di fondamentale importanza sia in fisica delle particelle che in fisica medica; nella prossima generazione di acceleratori saranno ancora più determinanti. Risoluzioni temporali eccellenti (decine di ps) saranno necessarie con la difficoltà aggiunta di dover operare a livelli di *rate* e radiazione elevati.

Sono stati studiati vari rivelatori, spaziando tra diverse tecnologie, a partire da quelli a gas fino a quelli al silicio: Multigap Resistive Plate Chamber (MRPC), Silicon PhotoMultiplier (SiPM) ed un nuovo prototipo di sensore al silicio, gli Ultra Fast Silicon Detector (UFSD). Le attività di ricerca sono state portate avanti sia tramite raggi cosmici che tramite test su fascio al T8 e H8 al CERN. Attività di ricerca e sviluppo sono state svolte per tutti e tre i tipi di rivelatori con diverse modalità di costruzione. Lo studio mostra risultati promettenti in quanto tutti i sensori hanno raggiunto risoluzioni temporali inferiori a 70 *ps*, con un valore minimo di 35 *ps*. Per le MRPC, oltre alla risoluzione temporale, sono stati esplorati con successo accorgimenti di costruzione al fine di aumentare il *rate* sostenibile.

Inoltre è stata realizzata un'analisi dati per il rivelatore TOF di ALICE (basato su tecnologia MRPC) incentrata sullo studio della risoluzione temporale legata a coppie di segnali adiacenti nei pad di lettura: le correzioni emerse hanno portato ad un miglioramento della risoluzione temporale finale del TOF.

Contents

Introduction

Traditionally the development of precision timing detectors was mainly aimed at improving the particle identification (PID) capability in particle physics experiments. This is still true, one of the most recent (in the last twenty years) example is the development of a large-area Time Of Flight (TOF) detector for the ALICE experiment at the LHC based on the new Multigap Resistive Plate Chambers (MRPC) technology, later employed also in other experiments. The next generation (both at short- and medium-term) hadron colliders, like the HL-LHC and the FCC, will shift the main purpose of *R&D* in the field of high-resolution timing detectors from PID to *tracking and timing* (also called 4-D tracking).

At the peak luminosity foreseen for the HL-LHC ($5 \cdot 10^{34}\ cm^{-2}s^{-1}$) the average number of events per bunch crossing (Pile-up) will be about 140, and much worse for the FCC where, at a peak luminosity 6 times higher than HL-LHC, the pile-up should go up to about 1000 (with a bunch spacing of 25 ns).

Till now (at the LHC) the problem of pile-up rejection has been tackled and solved with success by building tracking detectors with a finer segmentation, but at the next colliders, where the line-density (along the z coordinate) of interaction vertices will be of several per millimetre, the probability of *merged* vertices will be greater than 10% even with small-size sensor elements. This high pile-up density would have a significant impact on the physics reach of the experiments through the degradation of track reconstruction and assignment to the true primary vertex, and the rejection of non-interesting events. Therefore, if the spatial information alone will not help, the idea is to use a *precise* time information associated to each track, and possibly to each hit of a track on the tracking layers (a real 4-D tracker!). Taking for example the HL-LHC, with a beamspot time spread of $150 - 180\ ps$, the required time resolution of the tracker would be of the order of a few tens of picoseconds per layer. Another requirement for these detectors is the capability of the sensor/electronics to withstand the very high radiation levels expected at the future hadron colliders, especially in the inner/forward layers.

Last but not least, Research and Development, *R&D*, on high-resolution timing detectors could also be beneficial to other fields than particle physics, e.g. in medical facilities like the TOF-PET scanners.

This thesis regards the *R&D* and the optimisation of the time resolution of various sensors, from silicon to gaseous detectors.
The first chapter of the thesis is dedicated to the review of particle interactions with matter and to general properties of particle detectors. The second chapter is devoted to the description of the detectors studied and tested in this work, focusing on time resolution: MPRC, scintillators coupled to SiPMs and UFSD. The study performed on MRPCs is reported in Chapter 3; here the results obtained both on existing and fully operational MRPCs, the ALICE-TOF MRPCs, and the results obtained on new chambers are reported. The first part regards the data analysis dedicated to the understanding of effects that can affect the time resolution of the ALICE-TOF MRPCs. This study also provided important information that can be included in the Monte Carlo simulation of the detector. The second part is dedicated to the description of two *R&Ds* on MRPCs: one dedicated to the improvement of the already excellent time resolution and the other to the improvement of the rate capability. The study performed on SiPMs is reported in Chapter 4; here results on time resolution obtained with SiPMs coupled to scintillators are presented. The detector has been studied in several setups, both in cosmic ray (at the INFN Bologna lab.) and beam test setup (at T10 at CERN), and using a different coupling to the scintillator: direct or by means of fibers. Finally, the study performed on UFSDs is reported in Chapter 5; the time resolution of detectors from different manufacturers has been studied: CNM, FBK and Hamamatsu. These detectors have been studied both in a cosmic ray setup (at the INFN Bologna lab.) and in a beam test setup (at H8 beam line at CERN).

Chapter 1

Passage of particles through matter and detectors general properties

In this chapter the phenomena at the base of the passage of particles through matter and the general properties of detectors are laid out, focusing on time resolution.

1.1 Energy loss of particles

Crossing matter particles lose their energy; this energy loss can occur gradually (like for charged particles) or in a single collision (like for photons or neutrons). Another effect of the passage through matter is the deflection of the particle from its original direction.

1.1.1 Heavy charged particles

In this section we begin by describing the manner in which heavy charged particles (such as α particles) interact with matter [1–4]. The interaction is mostly through Coulomb force with the orbital electrons of the absorber atom. The electron involved receives an impulse that can displace it to a higher energy level (*excitation*) or even (if the energy is big enough) remove it from the atom (*ionisation*). The average energy required to remove the electron from the atom and creating in this way an electron-ion pair depends on the material ($\sim 30\ eV$ in gaseous detectors and a few eV in semiconductors).
In some types of detectors, the probability that the electron is recaptured

by the ion (recombination) is suppressed; in this way the ion pairs can be used as the basis for the operation of the detector itself. Moreover the newly free electrons may have an impulse big enough to cause secondary ionisations (*δ rays*). The delta rays range is small compared with the incident particle range; this ensures that the various ionisations are formed close to the primary track.

The maximum energy (W_{max}) that can be transferred from a charged particle of mass M to an electron of mass m_e in a single collision is:

$$W_{max} \simeq 2m_e\beta^2c^2\gamma^2 \qquad , \qquad M >> m_e \tag{1.1}$$

with $\gamma = 1/\sqrt{1-\beta^2}$ and $\beta = v/c$ of incident particle. Because this is a small fraction of the initial energy ($\sim 1/500$ of the particle energy per nucleon) the primary particle loses its energy in many interactions so the net effect is to decrease its velocity continuously until the particle is stopped or escapes from the material.

The expression that describes the mean rate of energy loss (*stopping power*, S) in a given absorber is known as Bethe-Bloch formula:

$$S = -\frac{dE}{dx} = K\ \frac{Z}{A}\ \frac{z^2}{\beta^2}\left(\ln\left(\frac{2m_e\gamma^2v^2W_{max}}{I^2}\right) - 2\beta^2 - \delta - 2\frac{C}{Z}\right) \tag{1.2}$$

$$K = 2\pi N_a r_e^2 m_e c^2 = 0.1535\ MeV cm^2/g$$

with r_e and m_e electron classical radius and mass, N_a Avogadro's number, I average excitation and ionisation potential of the absorber (normally treated as an experimentally determined parameter for each element), Z and A atomic number and mass of absorbing material, z charge of incident particle in units of e, W_{max} maximum energy transfer in a single collision. The unit of measurement of S is $[MeV\ cm^2/g]$; indeed it is an energy over meter multiplied by a factor $1/\rho$, with ρ the density of the absorbing material.

The shell (C) and density (δ) corrections are important at low and high energies respectively. The shell correction takes into account that when the incident particle velocity becomes comparable with the orbital velocity of the bound electron, the assumption that the electron is stationary with respect to the incident particle is no longer valid. The density effect takes into account that as the particle energy increases, its electric field flattens and extends, so that the distant-collision contribution increases. However, real media become polarised, limiting the field extension. Collisions with these outer lying electrons will therefore contribute less to the total energy loss.
In Figure 1.1 the stopping power of a positive muon passing through copper

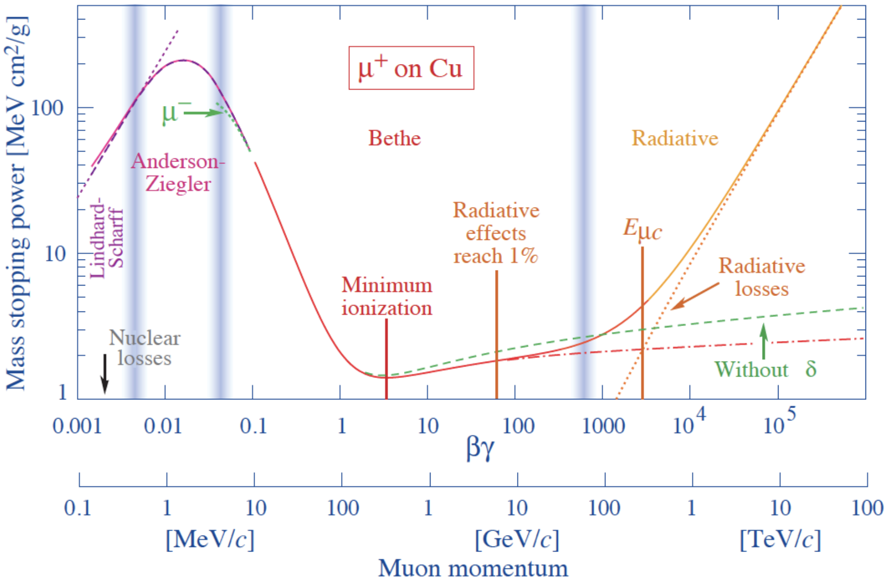

Figure 1.1: Stopping power for μ^+ in Copper as a function of $\beta\gamma = p/Mc$.

is shown.
The energy loss, at non-relativistic energies, is dominated by the $1/\beta^2$ factor and decreases with increasing velocity until about $v = 0.96\ c$ where a minimum is reached (Minimum Ionising Particle (MIP)), at about $\beta\gamma = 3$. The minimum value of dE/dx in various materials is almost the same, for particles of the same charge. Most relativistic particles (e.g. cosmic-ray muons) have mean energy loss rates close to the MIP.

For energies below MIP each particle exhibits a curve which, in most cases, is distinct from the other particles. This characteristic is often exploited in particle physics to identify particles in this energy range.

As the energy increases, $1/\beta^2$ becomes almost constant and dE/dx rises again due to the logarithmic (γ) dependence (see Eq.1.2).

Figure 1.2 shows the stopping power curve for different materials, 1.2(a), and the mass stopping power at minimum ionisation in several chemical elements, 1.2(b).

Equation 1.2 is only valid in the energy interval corresponding to approximately $0.1 < \beta\gamma < 1000$. At low energies the particle speed is comparable to the orbital speed of the atomic electrons so that a, possibly large, fraction of the energy loss is due to the excitation of atomic and molecular levels, rather than to ionisation. At even lower energies, the positively charged par-

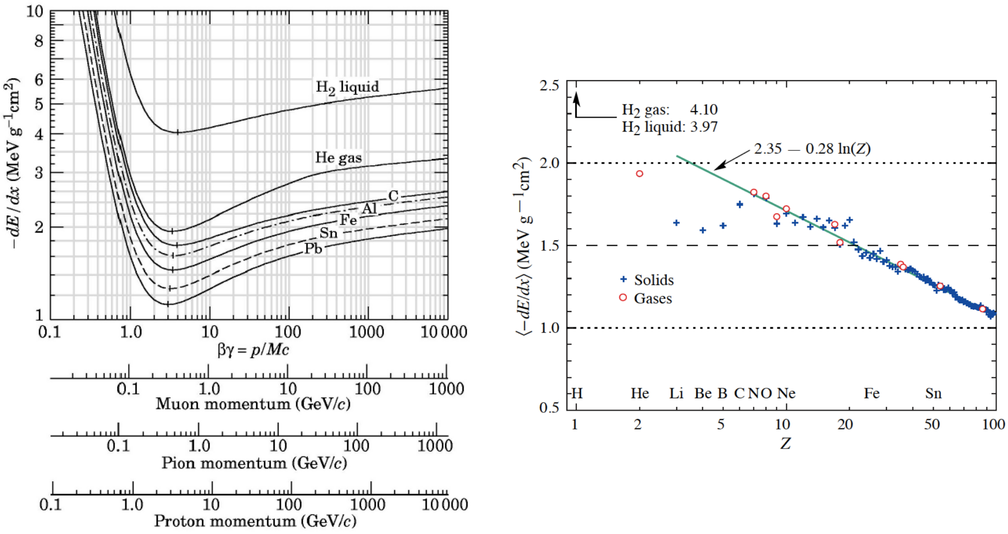

(a) (b)

Figure 1.2: Stopping power curve for different materials versus momentum of various particles (a) and mass stopping power for Minimum Ionising Particle in several chemical elements (b).

ticle starts to pick up electrons from the absorber; in this way its charge is reduced and from Eq.1.2, the energy loss becomes linear. The process continues until the charged particle has picked up Z electrons, becoming a neutral particle.

Figure 1.3(a) shows qualitatively the energy loss of particles as function of the depth of crossed materials (Bragg curve).

At energies higher than a few hundred GeV for π or μ (larger for protons) the bremsstrahlung losses in the nuclear fields becomes more important than ionisation. So the energy loss, dE/dx, of muons and pions grows dramatically at energies around 1 TeV.

To know how far the particles will penetrate the material (*range*) before they lose all their energy, the Bethe-Bloch formula should be integrated. The range depends on the material type, the particle type and its energy. In Figure 1.3(b) the typical range curve is reported. The corresponding time needed to stop a charged particle, for typical range values, is about few ps in solids (or liquids) and few ns in gases.

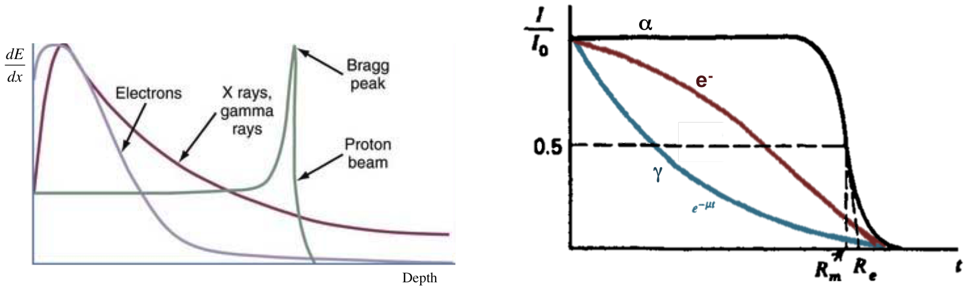

(a) (b)

Figure 1.3: Qualitative profile of the energy loss of e^-, γ and heavy charged (here proton) particles as a function of the depth of crossed materials (Bragg curve) (a); qualitative profile of the range for e^-, γ and heavy charged (here α) particles (b).

1.1.2 Energy loss distribution

A particle traversing an absorber undergoes a number of single interactions; each one contributes to the total energy loss.
The energy loss distribution of a particle passing through a thick detector follows (almost) a Gauss distribution; indeed, since the thickness of the material allows to have many collisions with atomic electrons, we can apply the Central Limit Theorem. For thinner absorbers the Central Limit Theorem stands no more, since the number of collisions is too small; the distribution is not gaussian. Interactions with atoms are less probable and produce a tail in the distribution. These tails are due to the possibility of large energy transfer in a single collision that, w.r.t. thicker absorber, are more relevant. The energy loss distribution of a particle passing through a moderate thickness detector or gas is well described by the Landau curve.
The Landau curve can be approximated using a parameter, λ, which represents the distance from the most probable energy loss [5]:

$$L(\lambda) = \frac{1}{\sqrt{2\pi}} e^{-\frac{1}{2}(\lambda + e^{-\lambda})} \tag{1.3}$$

$$\lambda = \frac{\Delta E - \Delta E^W}{\Delta_p} \tag{1.4}$$

$$\Delta_p = K\rho \, \frac{Z}{A} \, \frac{z^2}{\beta^2} \, x \tag{1.5}$$

where ΔE is the value of energy loss, ΔE^W is the most probable energy loss and Δ_p is the mean energy loss which can be approximated by taking the first multiplicative term of Eq.1.2.

The Landau distribution fails to describe energy loss in very thin absorbers, the most probable value decreases as the thickness decreases, while the distribution width spreads. In Figure 1.4 the energy loss distribution for 500 MeV pions incident on thin silicon detectors of different thickness is shown.

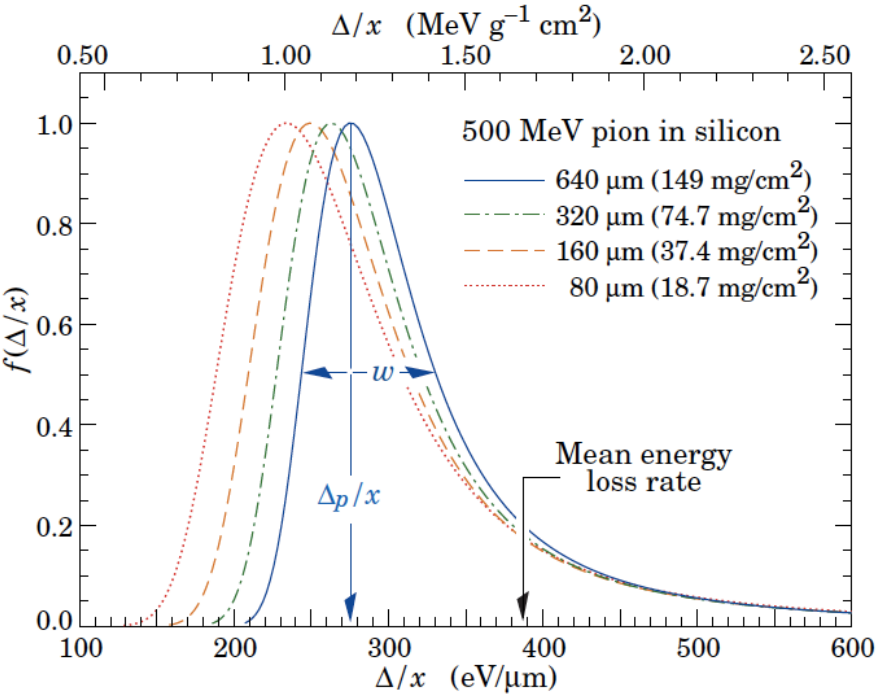

Figure 1.4: Energy loss distribution in silicon for 500 MeV pions, normalised to unity at the most probable value Δ_p/x, for different sensor thicknesses.

Depending on the thickness of the detector there are different theories to describe the distribution; to distinguish them, a κ parameter is defined as the ratio between the mean energy loss (Δ_p) and the maximum energy transfer in a single collision (W_{max}):

$$\kappa = \Delta_p/W_{max} \tag{1.6}$$

A thin absorber region is then considered if $\kappa < 10$, although for $\kappa > 1$ the distribution already begins to approach the Gaussian limit.

As an example the mean energy loss of a MIP in a silicon detector (density $\rho \sim 2.33\ gcm^{-3}$) is 1.66 $MeVcm^2g^{-1}$, so that the energy loss (ΔE) is 387 $eV/\mu m$.

1.1.2.1 Pair creation

Since we are concerned with detectors it is relevant to investigate deeper into the amount of energy that gets invested in creating pairs. Passing through silicon the particle looses energy creating n_p positive-negative pairs; n_p can be calculated as:

$$n_p = \frac{\Delta E}{W_{pair}} \tag{1.7}$$

where W_{pair} is the mean energy required to form an electron-positive charge pair. To generate a hole-electron pair in silicon an energy of 3.6 eV is needed (see Chapter 2); it follows that a MIP creates $\sim 2.7 \cdot 10^4$ pairs per 250 μm in silicon. In a gas detector, the energy required to form an electron-ion pair exceeds the ionisation potential because also inner shells can be involved and so a fraction of the energy of the particle can be dissipated by excitation.

For a commonly used gas, Freon $C_2H_2F_4$, the energy to generate an ion-electron pair is about 37 eV; for 250 μm, a MIP creates $\sim$ 2 electron-ion pairs.

The average charge carrier number N produced for a given energy loss follows a Poisson distribution; the error is then $\sqrt{N}$ and has to be corrected by the Fano Factor F [6] (see Section 1.4.1.1), depending on the material, reducing the fluctuation around average by $\sqrt{F}$. The statistical fluctuations in the number of produced charge carriers for a given energy loss is much smaller in solid-state detectors than in gaseous detectors.

1.2 Electrons

In this section we describe the manner in which electrons interact with matter. The interaction is mostly through Coulomb force with the orbital electrons of the absorber atom; since their mass is equal to the orbital electrons mass, when they interact they can lose a greater amount of energy (if compared to heavy particles) and be deviated from their path in a more significant way. Moreover their small mass causes the emission of electromagnetic radiation (*bremsstrahlung*) to be a significant term in the energy loss. This radiation comes from the acceleration of the incoming electron when it is deflected via its electromagnetic interaction with the nucleus.

The total energy loss for electrons is then composed of two parts:

$$\frac{dE}{dx} = \left(\frac{dE}{dx}\right)_{coll} + \left(\frac{dE}{dx}\right)_{bremss} \tag{1.8}$$

The radiative loss for the electrons becomes significant when the energies increase over a certain critical energy E_c:

$$E_c \sim \frac{(610 - 700)MeV}{Z} \tag{1.9}$$

which is the critical value at which collision energy loss and radiative loss are the same. For electrons of a few MeV the radiative losses are a small fraction of the total energy losses; the radiative term is more significant in materials with high atomic number (it varies as Z^2).
Introducing a quantity dependent on the the material, the radiation length X_0 (usually g/cm^2), the radiative term can be written as:

$$-\left(\frac{dE}{dx}\right)_{bremss} = \frac{E}{X_0} \tag{1.10}$$

with E energy of the incident particle. The radiation length is defined as the mean distance over which the electron energy is reduced by a factor $1/e$ by bremsstrahlung.

The energy loss by bremsstrahlung, varies as the inverse of the particle squared mass:

$$-\left(\frac{dE}{dx}\right)_{bremss} \propto \frac{1}{m^2} \tag{1.11}$$

This explains the negligibility of radiative term as the mass increases (as for heavy charged particles); for muons, the radiative loss is $4 \cdot 10^4$ times smaller than that of electrons.

Due to a greater susceptibility of electrons to multiple scattering by nuclei, their range is really different from that of heavy charged particles. In particular, the concept of range itself is under question; indeed the electron total path length is considerably greater than the distance defined by how deep the electron goes into the material. Again in Figure 1.3 a qualitative plot of the energy loss as function of the depth of crossed material and the range curve of electrons, compared with other radiations, are reported.

1.3 Photons

Photons mainly interact with matter in three ways, depending on their energy: photoelectric effect, Compton scattering, and pair production. Photon interaction is deeply different from charged particles; they are much more penetrating in the matter and a beam of photons, passing through a thickness, is just attenuated in intensity, keeping the same energy. The intensity of the beam I related to the initial intensity I_0, as a function of the crossed thickness of the material x is:

$$\frac{I}{I_0} = e^{-\alpha x} \tag{1.12}$$

with α absorption coefficient, which is characteristic of the absorbing material and can be defined as:

$$\alpha = \frac{\sigma N_A \rho}{A} = \frac{1}{\lambda} \tag{1.13}$$

with $\sigma = \sigma_{photoelectric} + \sigma_{compton} + \sigma_{pair}$ the total cross section, N_A Avogadro's number, ρ the density of the material and λ the mean free path; λ is defined as the average distance traveled in the absorber before an interaction takes place.

Again, in Fig 1.3 photon energy loss along depth and range curve are shown qualitatively for comparison with other radiation.

1.3.1 Photoelectric effect

An important effect which regards photons in matter is the photoelectric effect; this is exploited e.g. in Photomultipliers detectors (see Section 2.2.1) and arises in the absorption of a photon by an atom of the absorber material; due to conservation laws the effect can take place only on electrons bounded to the atom; the impinging photon disappears and is replaced by a photo-electron (the emitted electron) and the atomic nucleus recoils (due to momentum conservation). This process is defined by an energy threshold equal to the binding energy of the electron $E_{binding}$ so that the final energy of the electron E is:

$$E = h\nu - E_{binding} \tag{1.14}$$

with $h\nu$ photon energy.

The photoelectric cross section is dominant for low energy photons and is enhanced by high atomic number Z :

$$\sigma_{photoelectric} \propto \frac{Z^k}{(h\nu)^n} \tag{1.15}$$

with k between 4 and 5 and $n \sim 3.5$.

1.3.2 Compton scattering

The Compton scattering is instead characterised by the presence of the photon at the end of the interaction. The photon is scattered and deviated from its original direction of an angle θ. If $h\nu$ and $h\nu'$ are the photon energy before and after the collision:

$$\frac{h\nu'}{h\nu} = \frac{1}{1 + \frac{h\nu}{m_e c^2}(1 - \cos\theta)} \tag{1.16}$$

with $m_e c^2$ the rest mass energy of the electron.
The cross section is in general enhanced at lower energy and is proportional to Z:

$$\sigma_{compton} \propto Z \tag{1.17}$$

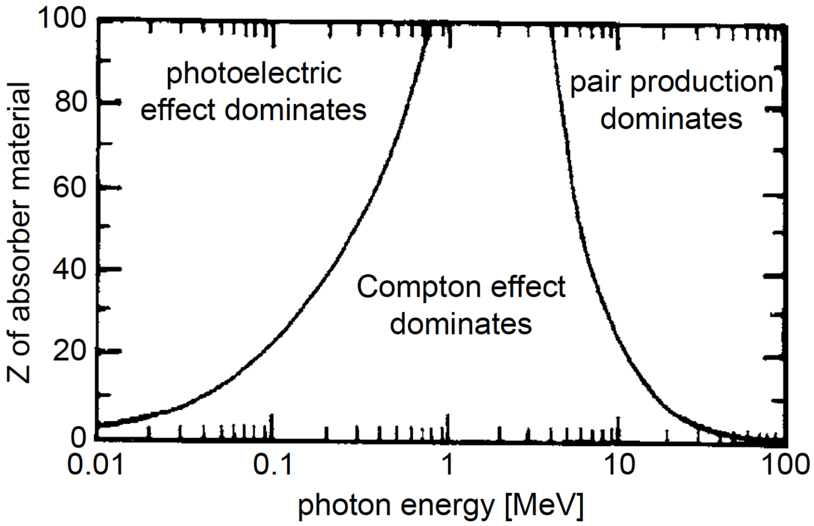

Figure 1.5: The three major types of photon interactions for different absorber materials and photon energy.

1.3.3 Pair production

The last dominant effect of photon interaction in matter is the pair production. This process has an energy threshold equal to 1.022 MeV which is twice the mass of an electron; indeed this effect involves the transformation of a photon in an electron-positron pair:

$$h\nu > 2m_e c^2 \sim 1.022\ MeV \tag{1.18}$$

The pair production cross section is dominant at high energy and, above the energy threshold, is proportional to Z^2 :

$$\sigma_{pair} \propto Z^2 \tag{1.19}$$

The positron emitted in this process quickly annihilates in two γ.
In Fig.1.5 a comprehensive illustration of the relative importance of the three processes described for different absorber materials and photon energies is shown.

1.4 Detector properties

The knowledge of the interaction of particles with matter represents the basics for the development of particle detectors whose main properties are reviewed in the following. In this section we introduce and explain some general characteristics common to particle detectors. Many particle detectors have been developed for various applications but they rely on a basic principle: the transfer of part or all of the radiation energy to the detector and its conversion to a measurable signal [1,3].

1.4.1 Generalities

The quality of a detector is determined by its resolution on the measure of a designed quantity. So we refer to energy, time and spatial resolution depending on the measurement we are considering [1,3,5].
In general the measured quantity turns out to be described by a distribution function $F(x)$ with a true value x_0 and a standard deviation σ. For example suppose you want to use a photo sensor to detect from a side of a scintillator detector the light produced by the scintillator itself and you want to measure the time resolution depending on the position in which the particle hits the scintillator. The distribution function is constant along the scintillator. Indeed it follows a rectangular distribution $F(x) = 1$ from t_{min} to t_{max}, the minimum and maximum time requested by the photon to reach the pick up point. The time resolution is then given by:

$$\sigma = \frac{t_{max} - t_{min}}{\sqrt{12}} \tag{1.20}$$

In many other cases, e.g. for time measurement, the distribution function follows a Gaussian distribution:

$$F(x) = \frac{1}{\sigma\sqrt{2\pi}} e^{-\frac{(x-x_0)^2}{2\sigma^2}} \tag{1.21}$$

For the normal distribution, the resolution of a detector can be expressed in terms of Full Width at Half Maximum (FWHM) defined as:

$$FWHM = 2\sqrt{2\ln 2}\;\sigma = 2.3548\;\sigma \tag{1.22}$$

Observing a particle going through a detector, the distribution of ionisation events produced is well describe by a Poisson distribution:

$$P(n) = \frac{\nu^n}{n!} e^{-\nu} \tag{1.23}$$

with ν the mean value and n the number of events; the distribution is characterised by a standard deviation:

$$\sigma = \sqrt{\nu} \tag{1.24}$$

The fluctuation in this number is the main reason of the width of the energy distribution.

In the following section we will focus on the energy resolution of particle detectors. Later on we will focus on time resolution which is the main topic of this work.

1.4.1.1 Energy resolution

A detector with good energy resolution (R) is able to distinguish two close lying energies; two peaks are considered to be resolved if they are separated by a distance greater than their FWHM.
The response of many detectors is approximately linear, so that, on average, the energy E is related to the average number of ionisation N by Eq.1.7. As mentioned, the formation of ionisation events follows a Poisson distribution, so, from Eq.1.24 the standard deviation is $\sigma = W_{pair}\sqrt{N}$. Then, using Eq.1.22, the energy resolution is:

$$R = \frac{FWHM}{E} = \frac{2.3548\;W_{pair}\sqrt{N}}{W_{pair}N} = \frac{2.3548}{\sqrt{N}} \tag{1.25}$$

If the full energy of the radiation is absorbed, the distribution can not be described anymore by Poisson statistics. Indeed the total number of ionisations which can occur and the energy lost in each ionisation are thus constrained by the fixed total energy deposited. The energy resolution is then better or rather reduced by a factor $\sqrt{F}$:

$$\sigma = \sqrt{FN} \tag{1.26}$$

F is called the Fano factor (~ 1 for scintillator detector, < 1 for silicon and gaseous detector). This reduce the final energy resolution to:

$$R = 2.3548\sqrt{\frac{F}{N}} \tag{1.27}$$

1.4.1.2 Efficiency

One of the most important parameter of a detector is the efficiency, which represents its capability to detect a particle emitted by a source. In particular the total efficiency ϵ, involves both the intrinsic efficiency of the detector ϵ_d (intrinsic capability to reveal a particle) and the geometrical efficiency ϵ_g. So:

$$\epsilon = \frac{n^\circ\ particle\ detected}{n^\circ\ particle\ emitted\ by\ a\ source} = \epsilon_d\ \epsilon_g \tag{1.28}$$

Quite often a trade off between efficiency and resolution has to be found, for practical reasons.

A really common method to measure the efficiency of a detector is by means of a telescope like the one in Fig. 1.6: in the middle the detector under study and two trigger counters on top and bottom, with their own efficiency ϵ_1 and ϵ_2. If there are N particles passing through the detector, the efficiency is

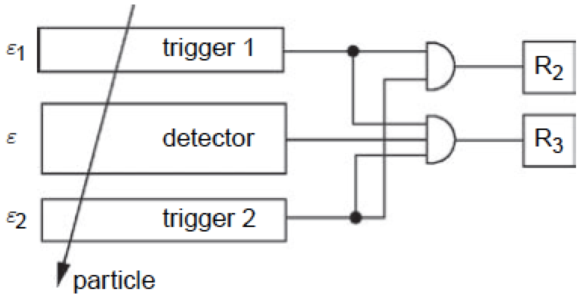

Figure 1.6: Simple scheme of a telescope to measure the efficiency ϵ of a detector.

given by the ratio between the threefold (R_3) and the twofold (R_2) number of coincidences:

$$\frac{R_3}{R_2} = \frac{\epsilon_1 \; \epsilon_2 \; \epsilon \; N}{\epsilon_1 \; \epsilon_2 \; N} = \epsilon \tag{1.29}$$

In first approximation, the efficiency follows a Bernoulli statistic, so the standard deviation is defined as:

$$\sigma_{eff} = \sqrt{n \; p \; q} \tag{1.30}$$

where n is the total number of experiments and p and $q = 1 - p$ are the only two possible outcomes, which define a Bernouilli distribution.
In this particular case:

$$\sigma_{eff} = \sqrt{R_2 \; \epsilon \; (1 - \epsilon)} \tag{1.31}$$

The intrinsic efficiency of the detector is strongly dependent on the detector material and on energy and type of particles. The efficiency usually also depends on the point where the particle has passed through the detector (homogeneity, uniformity) and on the angle of incidence (isotropy).

1.4.1.3 Dead time

Another element to be taken into account when designing a detector is the dead time, that is the time frame after each event during which the detector is insensitive to incoming particles. In an environment with a high rate of particles, like the *LHC*[1], dead time can become an important issue. These losses affect the observed count rates and distort the distribution between the arrival of events; it can really affect some detector properties such as the efficiency.

The dead time is indeed defined as the minimum time to record two separated pulses by the detector. During this amount of time the detector is insensitive and other events are lost. This limit time can be due both to processes in the detector itself or to the associated electronics. To avoid losses, the counting rate of the detector must be kept sufficiently low so that the probability of a second event occurring during a dead time period is small.

Moreover the dead time of the elements could be variable depending on the count rate, the pulse shapes, etc.

---

[1] Large Hadron Collider

1.4.1.4 Ageing

A detector and his capability to reconstruct the event might also suffer from deterioration properties. For example, in a gas detector like MRPC (see Section 2.4), filled with a mixture of $C_2H_2F_4$ and SF_6, particular attention should be given to the gas purification itself; otherwise some ageing effect can been observed. These are mostly associated to the production of fluorine, which etches the MRPC glass sheets; fluorine can be produced in the breakdown of gas molecules during streamer or avalanche discharges. In ALICE-TOF MRPC (see Section 2.5), where there is an ad hoc system for gas controlling, no ageing effect has been observed [7]. Anyway, recently, some ageing effect have been observed in an MRPC with a different design, that had been used for ten years in a cosmic ray study, with a less controlled gas system.

In high energy physics an important ageing cause is due to the harsh radiation environment in which detectors work. So the radiation hardness becomes an important characteristic, especially in silicon detectors (see Section 2.6). Here the main damage is caused by the bulk (or rather displacement) effect [8] caused by radiation; it consists in a displacement of atoms from their position due to Non Ionising Energy loss (NIEL), via electromagnetic and strong force. In this way the radiation creates some defects in the lattice, called interstitials and vacancies. Usually the damage caused by different particles is normalised to the 1 MeV neutron equivalent fluence (n_{eq/cm^2}). The consequences of these damage are a formation of forbidden energy levels with a change in the number of dopants (donors/acceptor); the donors/acceptor can indeed be inactivated. This can be particularly critical in a gain silicon detector (like SiPM, see Section 2.7, or UFSD, see Section 2.8); with a high fluence the gain layer can indeed be dramatically reduced. The macroscopic results can be several: increase of the leakage voltage, change of the operation voltage, decrease of Charge Collection Efficiency (CCE). In particular the bulk effects are bigger for higher fluence of particle and for larger volume.

1.4.2 Signal formation

As described above, charged particles transfer their energy to matter through direct collisions with the atomic electrons, thus inducing excitation or ionisation of the atoms. The form in which the converted energy appears depends on the detector and its design; in a wide category of detectors, the net result of radiation interaction is the appearance of an electric charge Q.

In silicon diode or gas detectors the signals from detectors arise because of the motion of charge carriers after they are formed by ionisation. Indeed,

when an external electric field is applied, the signal is given by the induced current due to the movement of the positive and negative charges as they drift towards the cathode and anode [3, 9–12].
The Shockley-Ramo theorem states that the instantaneous current i and the charge Q induced on a given electrode are:

$$i = -(nq)\mathbf{v} \cdot \mathbf{E}_w(x) \tag{1.32}$$

$$Q = -qV_w(x) \tag{1.33}$$

, where nq and $\mathbf{v}$ are the charge and drift velocity of the carriers and $\mathbf{E}_w(x)$ and $V_w(x)$ are called *weighting field* and *weighting potential*. They are the electric potential and field that would exist at instantaneous position x with some artificial boundary conditions: the voltage on the electrode for which the induced charge is to be calculated is set equal to unity, all other electrodes are set to zero; even if a trapped charge is present within the detector volume, it is ignored in the calculation (i.e. the Laplace equation is used rather than the Poisson equation).

While the path of the charge q is determined by the actual operating electric field, the induced charge Q can be calculated much easier with the help of the weighting field.

As an example, the weighting field for a parallel plate detector (capacitor), with two infinite plates, separated by a distance d, is:

$$\mathbf{E}_w(x) = -\frac{1}{d}\overrightarrow{\mathbf{e}}_x \tag{1.34}$$

with $\overrightarrow{\mathbf{e}}_x$ the unit vector along x. Once the last of the carriers arrives at its collecting electrode, the process of charge induction ends and the pulse is fully developed. The time evolution of the signal is of fundamental importance in understanding the timing properties of detectors as well as in predicting the effects of changes in the location of the radiation interaction on the shape of the pulse.
In conclusion, the induced currents are only weakly sensitive to the charge position but depend strongly on the charge velocity magnitude and direction.

So the particle, passing through the detector deposits its energy creating positive and negative pairs; this charge moving under an applied electric field, induces a charge Q on the electrode and creates an output signal, a current, $i(t)$. The current flows for a time equal to the charge collection time, t_c ($\sim ms$ for gas detector, $\sim ns$ for silicon detector):

$$Q = \int_0^{t_C} i(t)dt \tag{1.35}$$

1.5 Time resolution

In many applications time measurement is of primary importance. This is basically correlated to two key parameters [13–16]: the signal to noise ratio (S/N) and the slew rate (dV/dt), i.e. how fast the signal rises.

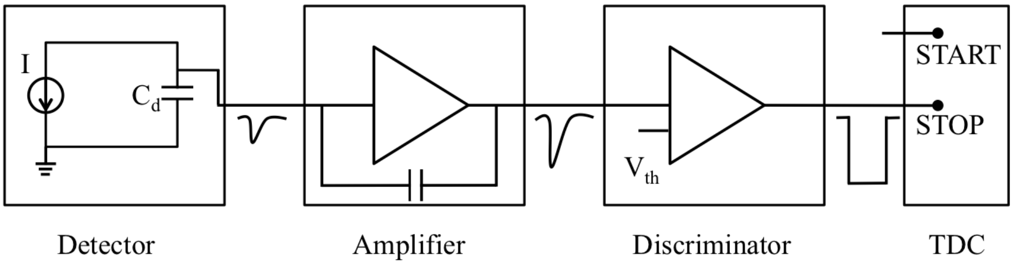

Figure 1.7: Schematic view of the basic elements of a time measurement chain.

Figure 1.7 reports a schematic view of the basic elements used to perform time measurements. The detector can be, in general, represented as a current generator (I) in parallel to a capacitance (C_d). The measurement chain typically foresees an *Amplifier*, used as signal shaper, a *Discriminator*, used to compare the signal to a reference level (V_{th}) and to convert it to a logic signal, and a time digitiser (Time to Digital Converter, *TDC*) to measure time intervals.
Taking into account these basic elements the time resolution (σ_t^2) of the system can be expressed as:

$$\sigma_t^2 = \sigma_{TDC}^2 + \sigma_{current}^2 + \sigma_{time\ slewing}^2 + \sigma_{jitter}^2 \tag{1.36}$$

where the terms of the equation will be explained in the following.

1.5.1 TDC

To measure time intervals typically a Time to Digital Converter (TDC) is used. The simplest version of such devices can be considered as a counter of internal clock cycles. So the time delay between a start event and a stop event is given by an integer n representing the number of clock cycles between the two events. Depending on the clock frequency the time is then $n\ \Delta t$, being Δt the duration of a clock cycle (related to the internal clock frequency).

From Eq.1.20 the time resolution associated with TDC is then:

$$\sigma_t = \frac{\Delta t}{\sqrt{12}} \tag{1.37}$$

The contribution of TDC is usually small, indeed for a $\Delta t = 25\ ps$ the contribution to the time resolution due to the TDC is $7\ ps$.

1.5.2 Current

As reported in Section 1.4.2, the signal from the detector arises from an induced current, as the Shockley-Ramo theorem (Eq 1.32) stands. If this current undergoes variations the signal shape is modified, spoiling the time resolution. These fluctuations can be due to different effects related to fluctuation of variables in the just quoted formula:

- n: the nature of the energy deposition process is a statistic process of creation of a certain number n of positive-negative pairs in the detector which can dramatically change event by event (Landau fluctuations), see Section 1.1.2.1. This fluctuations also affect the signal amplitude (see following section).

- v: the velocity of the particle not only has to be high, to reduce the rise time (increase the slew rate) but also has to be as uniform as possible, to avoid fluctuations. The method used for the detector which we focused on in this thesis, is to saturate the drift velocity by means of a high electric field inside the detector; the field has to be the same in each point of the detector. The goal is to have a time measurement independent of the position of impinging.

- E_w: the weighting field has to be as uniform as possible, to couple with the electrode in a position independent way; the uniformity of E_w is strictly related to the geometry of the detector.

1.5.3 Time slewing

The time measurement depends also on the pulse amplitude, which is related to the amount of energy deposition in the detector. The time slewing effect (in literature also called time walk) is due to the comparison of the signal with a fixed threshold voltage V_{th}, usually related to the nature of the analog to digital conversion of the signals.

Looking at the Figure 1.8 (considering linear signals) the signal of amplitude S and rise time t_{rise} crosses the threshold at $t = t_0 + t_d$, where:

$$t_d \propto \frac{t_{rise} V_{th}}{S} = \frac{V_{th}}{dV/dt} \tag{1.38}$$

with:

$$\frac{dV}{dt} = \frac{S}{t_{rise}} \tag{1.39}$$

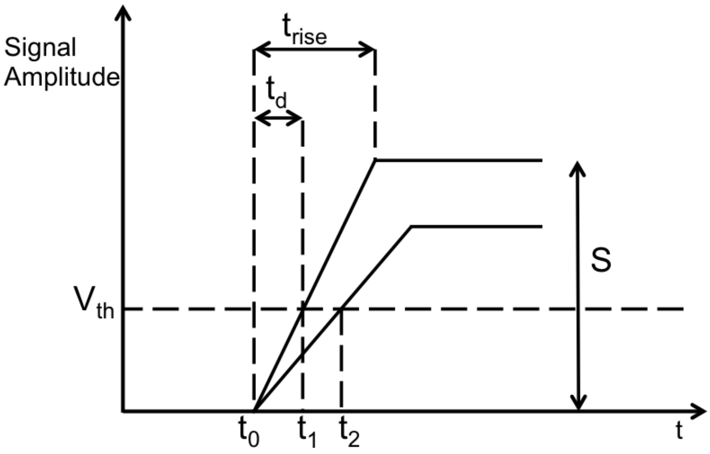

Figure 1.8: Sketch of the signal rise time explaining the time slewing effect; this is an intrinsic effect that arises in the comparison of the signal with a fixed threshold voltage V_{th}. Two signals of different amplitude, arriving at the same time t_0, are detected at two different times $t_1,\ t_2$.

V_{th} is chosen to avoid the noise; it must be greater than the voltage noise amplitude N: $V_{th} \sim 5 - 10\ N$. The time resolution due to the time slewing effect is then the RMS of the t_d distribution:

$$\sigma_{time\ slewing} = \left[t_d\right]_{RMS} \propto \left[\frac{N}{dV/dt}\right]_{RMS} \tag{1.40}$$

This effect is broadened by Landau fluctuations; the fluctuations also affect the shape of the current signal (see previous section).
A direct consequence of a threshold can be understood looking at Figure 1.8; signals of different amplitudes, starting at the same time t_0, overcome V_{th} at different times t_1 and t_2. Amplitude variations then lead to a *walk* (Δt) in timing.

From Eq. 1.40, the *time slewing* effect can be reduced both by increasing the slew rate and reducing the threshold (if the noise allows to do so). Anyway, as we will see in Section 1.5.5, the choice of the threshold is a trade off between several effects.
However the time slewing effect can be corrected by measuring also a quantity proportional to the amplitude, e.g. by means of a Charge Integrator ADC[2], which measures the charge of the signal integrating it, or with the Time Over Threshold (TOT) method, which measures the time interval during which the signal is above the threshold by measuring also the trailing edge of the signal or with a Constant Fraction Discriminator (CFD), which works looking at the whole signal and emits the logic pulse when the input signal reaches a certain fraction of the peak value.

1.5.4 Jitter

For a fixed amplitude, the signal level is still modulated by noise, due to both electronics or detector itself; because of this intrinsic noise, the time of threshold crossing (t_d) fluctuates. The timing jitter can be expressed by:

$$\sigma_{jitter} = \frac{N}{\left(dV/dt\right)_{V_{th}}} = \frac{t_{rise}}{S/N} \tag{1.41}$$

where dV/dt is evaluated at the threshold level V_{th}, N is the rms noise voltage. High dV/dt is then of fundamental importance to have a good time resolution.

From the previous arguments it is clear that choosing the right value for the threshold is not trivial; a detailed discussion is reported in the next section.

1.5.5 Choice of the threshold

The choice of the threshold to improve the time resolution is a trade off between several effects; to minimise the time slewing effect the threshold, by definition, should be as low as possible (best for $V_{th} = 0$) but should also be bigger than the noise (best for $V_{th} \sim 5N$). Furthermore, the time resolution is directly dependent on the slew rate, so the threshold should be set at the value of maximum dV/dt. The rise time is strictly correlated to the time constant ($\tau = RC$) of the system, depending both on the amplifier rise time, t_{ra}, and detector rise time, t_{rd}; the total rise time t_{rise} is indeed:

$$t_{rise} = \sqrt{t_{rd}^2 + t_{ra}^2} \tag{1.42}$$

---

[2] Analog to Digital Converter

For a system with a single RC integrator[3], the maximum slope of the signal (dV/dt) is at $t_{rise} = 0$. Indeed, for small t:

$$V(t) = V_0(1 - e^{-t/\tau}) \tag{1.43}$$

$$\sim \frac{V_0}{\tau} t \tag{1.44}$$

, with V_0 the signal amplitude. So the slew rate is then maximum for $t = 0$ (see Eq.1.43) and the output of the signal, for small time, is linear (see Eq. 1.44). This is no longer true for more than one RC constant; this can be understood by the following. For two time constants, the output signal for small t can be obtained solving the differential equation:

$$\frac{V_0}{\tau_1} t = \tau_2 \frac{dV(t)}{dt} + V(t) \tag{1.45}$$

For small t:

$$V(t) \sim \frac{V_0 \tau_2}{\tau_1} e^{-t/\tau_2} + \frac{V_0}{\tau_1}(t - \tau_2) \tag{1.46}$$

The output signal is then delayed by τ_2 and a curvature is introduced at small times; the slew rate is no longer optimised for $t = 0$.

To understand how to maximise the slew rate, the t_{ra} can be expressed in amplifier bandwith (f_μ); the rise time of the signal is indeed usually defined as the difference between the 10% and 90% of the signal. Using Eq.1.43 and $\tau = 1/(2\pi f_\mu)$:

$$t_{ra} = t_{90\%} - t_{10\%} = 2.2\ \tau = \frac{0.35}{f_\mu} \tag{1.47}$$

So from Eq. 1.39:

$$\frac{dV}{dt} \propto f_\mu \tag{1.48}$$

So to get large dV/dt and then improve time resolution (see Eq.1.40 and 1.41) a solution seems to be a wide bandwidth. Actually this is not totally true, indeed the electronic noise is proportional to the bandwidth $N \propto \sqrt{f_\mu}$. So, to maximise the slew rate without increasing too much the noise, the amplifier rise time is equal to the signal rise time. This can be understood from Eq.1.41 using Eq.1.42:

$$\sigma_{jitter} \propto \frac{\sqrt{t_{rd}}}{S} \sqrt{\frac{t_{rd}}{t_{ra}} + \frac{t_{ra}}{t_{rd}}} \tag{1.49}$$

---

[3] In a RC circuit $i(t) = C\ \frac{dV}{dt}$ so that $V_0 = \tau \frac{dV}{dt} + V$, with $\tau = RC$. The solution of this differential equation can be obtained by separation of variables and is reported in Eq.1.43.

The minimum of the second term in the equation is obtained for $t_{rd} = t_{ra}$. Hence, a current mode amplifier (Broad Band Amplifier , BBA) takes full advantage from a detector with a very fast slew rate (even thought with a higher noise); it has a large bandwidth and by not shaping the signal it has a $dV/dt \sim di/dt$. To maintain a good time resolution with a large bandwidth however it's important to keep the input capacitance low and a high output one.

Chapter 2

Particle detectors for time applications

In this chapter we describe the properties of the detectors used for our *R&D* on time measurements. In particular we review the properties of scintillator detectors, photodetectors (standard and MCP PMs), gaseous detectors, focusing on MRPC, and semiconductor detectors, focusing both on Silicon PhotoMultiplier (SiPM) and on a new prototype, Ultra Fast Silicon Detector (UFSD). The properties of these detectors are presented with particular attention on their application for time measurements.

2.1 Scintillator detectors

A scintillator is a luminescence material [1–3,5,17]. When a charged particle passes through this kind of material the energy loss is converted into a number of photons in the visible or near visible range; these photons have then to be collected by a photodetector.

This twofold function, of luminescence and collection, has an obvious disadvantage: the generation of one photoelectron needs much more energy than what is necessary for example to create a positive-negative pair in silicon detectors, 3.65 eV; the scintillator plus photodetector require not less than 50 eV. None the less this is balanced by the possibility of building detectors of large size at a relative low cost.

The main features that a good scintillator should have are :

- good efficiency, in translating kinetic energy to detectable light output,
- linearity of the light output with the energy lost by the incident particle,
- emission spectrum that should be transparent to its absorption,

- decay time that should be short in order to have a fast signal,
- refraction index that should couple to the window of the photodetector (see Section 2.2). A dopant is often added in the scintillator for a better coupling.

There are several scintillator materials (inorganic, organic, gas); for the purpose of this thesis only the main characteristics of organic scintillators will be treated.

2.1.1 Organic scintillators

Compared with other kind of scintillators, organic scintillators generally yield less light; however they are faster with a decay time in the order of ns and a rise time even faster. Plastic scintillator are by far the most widely used; the best ones are based on polyvinyltoluene and polystyrene.

The light output of the scintillator has two different contributions: fluorescence (faster) and phosphorescence (slower), with a longer wavelength. The explanation of these phenomena lies in the molecular structure: the scintillation is produced by the excitation of electrons and their following decay to the ground state. The ground state is a singlet state S_0 (spin=0); the kinetic energy of the impinging particle can then be absorbed by excitation in one of the singlet excited state $S_1, S_2, \dots$ (see Figure 2.1). As shown, there is also a set of triplet state (spin=1) $T_1, T_2, \dots$.
The energy required for excitation is in the order of eV, for the $S_0 \rightarrow S_1$ transition; for the higher-lying states the energy for $S_i \rightarrow S_{i+1}$ is smaller. Each of these electronic states is subdivided in several *vibrational* states (e.g. $S_{00}, S_{01}, S_{02}, S_{03}$), separated by $\sim 0.15\ eV$. This energy is large compared to the average thermal energy ($\sim 0.025\ eV$) so usually the molecules at room temperature are in S_{00} state. When the higher singlet states ($S_2, S_3, \dots$) are excited, they quickly ($\sim ps$) de-excite to S_1 and then, in particular, to S_{10}, without emission of radiation. The transition is then between S_{10} and the vibrational states of the ground state S_0, with emission of radiation, *fluorescence* (or *prompt* fluorescence). The fluorescence decay time (τ_f) is in the order of ns (fast component). Thanks to the lower energy of decay (except of $S_{10} \rightarrow S_{00}$ transition, for which the energy can be the same) versus the absorption energy, the organic scintillators have just a small overlap (*Stokes shift*) between the two spectra (emission and absorption) and so they result almost transparent to their own fluorescence
Instead of this decay process, some excited singlet state S_1 can become a triplet state by means of an *intersystem crossing* transition. From the T_1

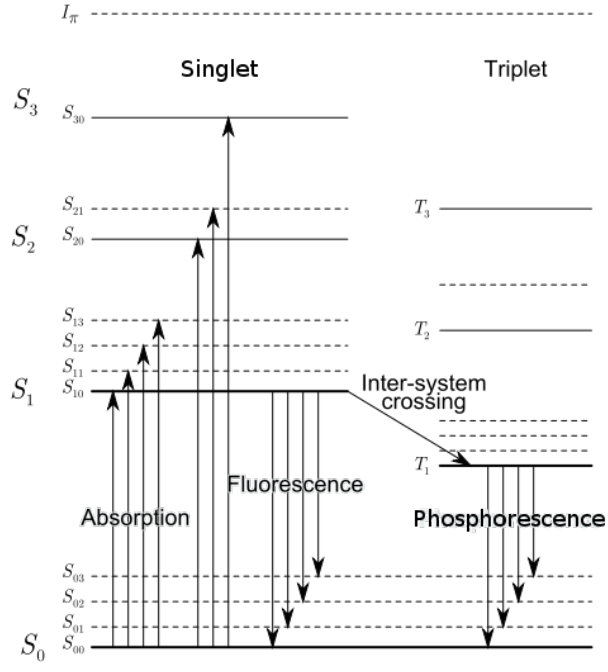

Figure 2.1: Molecular structure of organic scintillator.

state the electron can be excited back to S_1 and decay with normal fluorescence (*delayed* fluorescence) or decay to S_0. The decay time τ_s to S_0 is longer ($\sim ms$) (slow component) and the wavelength is bigger (T_1 has a lower energy than S_1); this delayed light is called *phosphorescence* [1].

When a charged particle passes through an organic scintillator, only a small fraction (scintillation efficiency, S) of energy (dE/dx) is converted into luminescence (dL/dx), depending on the particle type and energy. For fast electrons this relation is almost linear: $\frac{dL}{dx} = S\frac{dE}{dx}$. Anyway the relation is no longer linear for slower electrons or heavier particles (like α); this is due to recombination and quenching from damaged molecules, related to the ionisation density along the track of particles. This quenching leads to a *Birks* factor which deteriorates the scintillation efficiency. The relation between energy loss and luminescence follows then the *Birks' formula*:

$$\frac{dL}{dx} = \frac{S\frac{dE}{dx}}{1 + k_B\frac{dE}{dx}} \tag{2.1}$$

---

[1] The existence of these two components (τ_f, τ_s) is fundamental for the Pulse Shape Discrimination (PSD); indeed it permits Particle IDentification.

where k_B is the Birks' constant which depends on the material.

2.1.1.1 Timing properties

For timing measurements both the amount of light generated by the plastic scintillator and the time duration of the light pulse are crucial.

For timing applications the most important component of luminescence is the fluorescence; the time required to populate the levels (*rise time*) is about 0.5 *ns*; the *decay time* for fast scintillator is just three or four times greater. Considering the population of levels over time a gaussian function $f(t)$, for a decay time τ, the light output shape is given by:

$$I(t) = I_0 \; f(t) \; e^{-t/\tau} \tag{2.2}$$

with I_0 being the total intensity of the signal if the whole process was instantaneous. For time measurment both rise time and decay time are important; the rise time is related to the statistical nature of photons production, fluctuation in the emission, transmission and collection of scintillation photons.

As mentioned (Section 1.5), the amount of light and in particular its uniformity can affect the time resolution. The self absorption and reemission of the fluorescence can cause a worsening in time resolution; the spread induced is larger as the dimensions of scintillator increase:

$$I(x) = I_0 \; e^{-x/\lambda} \tag{2.3}$$

with λ attenuation length, depending on scintillator material.
This effect however is not significant compared to others; indeed an effect that has to be considered is the finite time needed by photons from the creation point to the photodetector; this is strictly correlated with the length of the scintillator and can produce a spread in time due to fluctuations from reflections on the scintillator surface. The spread on time resolution is larger for larger size scintillators. The condition at the interface between the scintillator and the external container (e.g. air, mylar) is then fundamental; the total internal reflection depends indeed on the refraction index of the internal medium n_1 and of the external medium n_2:

$$\theta_c = arcsin\left(\frac{n_2}{n_1}\right) \tag{2.4}$$

For $\theta > \theta_c$ there is the total reflection. To recapture the light that would escape from surface, the scintillator is normally surrounded by a reflector. However a total internal reflection has an exception in the contact area with the photodetector (photomultiplier window, optical grease,...); in particular

the refractive indices should be close to that of contact surface of the photo detector ($\sim 1.4 - 1.5$).
Another shrewdness that has to be taken is to cover the scintillator with a black paper to prevent detecting ambient light.

2.1.2 WLS fibres

The coupling between scintillator and photodetector can be *direct* or by means of optical fibres; this second option can be useful in case of radioactive environments, to move the detector away from the most radioactive zone.
Using a particular kind of optical fibres, WaveLength Shifting (WLS) fibres, is also possible to further optimise the wavelength for a better coupling between scintillator and photodetector.
A WaveLength Shifting material is a fluorescent material optimised to absorb a certain wavelength and emit a larger one.
A WLS fibres has a *core* doped with this kind of material.

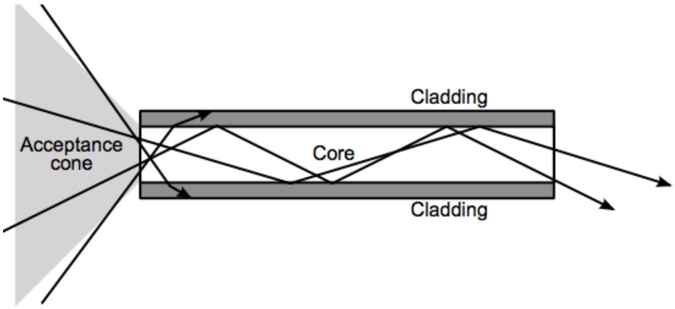

Figure 2.2: Sketch of light propagation in an optical fibres.

An optical fibre is composed of two concentric layers, the core and the surrounding *cladding*. The materials are chosen to have total internal reflection (hence $n_{cladding} < n_{core}$). Figure 2.2 shows a sketch of light propagation in an optical fibre. The light enters the core where the absorption and reemission of light at a different wavelength occurs; the light then is propagated in the core by continuous reflection along the surface separating the core from cladding.

2.2 Photodetectors

To measure the light from a scintillator, a photodetector is necessary. A large fraction of experiments in High-Energy Physics (HEP), astrophysics and medical physics makes use of this technique.

2.2.1 PM

PhotoMultiplier (PM) tubes are the most common photodetectors. The basic process arises in the photoelectric effect (Section 1.3.1). When the incident photons impinge on what is called *photocathode*, they can be converted into primary electrons. The electrons are accelerated through a complex series of dynodes to the anode. In Figure 2.3 the working principle of PMs is schematically represented.

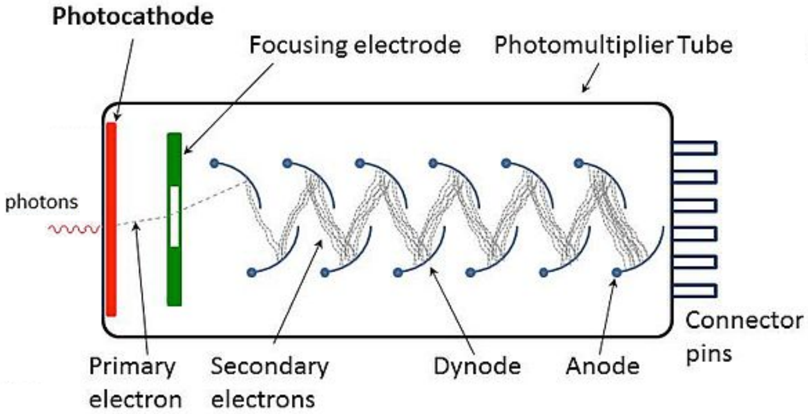

Figure 2.3: Scheme of the working principle of a PhotoMultiplier.

In particular the primary electrons are focused by an electrode to the first dynode where secondary electrons are emitted and so on, through the other dynodes, so that an avalanche multiplication is created. The avalanche is then collected at the anode. The whole system is inside a vacuum tube. In a PM the gain G is proportional to number of diodes n and to the secondary emission coefficient, δ. For a typical value of $n = 12$ and $\delta = 4$:

$$G = \delta^n \sim 1.7 \cdot 10^7 \tag{2.5}$$

Then the voltage signal due to a single photoelectron can be roughly estimated, considering a typical termination resistor of $R = 50\ \Omega$, and collection time of $\Delta t \sim 5\ ns$, as:

$$V = R\frac{\Delta Q}{\Delta t} = R\frac{\Delta(e \cdot G)}{\Delta t} \sim 27\ mV \tag{2.6}$$

with e electron charge. So single photoelectron detection is possible.

The efficiency mostly depends on the photocathode material; for a typical material made of alkali metals, it is $(10-30)\%$.

The time resolution is influenced from both fluctuations on the transit time of electrons trough the PM and on the noise. One of the key points is the region in which the electrons are focused to the first dynode; this has to be as spatially uniform as possible so that the time of arrival is independent of the impinging position on photocathode.

For the dynode structure there are several possibilities e.g. beyond the standard one (Fig.2.3), the MCP.

2.2.2 MCP-PM

The Micro Channel Plate (MCP)-PM is a photomultiplier with a particular configuration of the dynodes. The discrete dynodes of a standard PM are replaced by continuous multiplication channels of about 10 μm diameter. In Figure 2.4 a sketch of the MCP-PM working principle is shown.

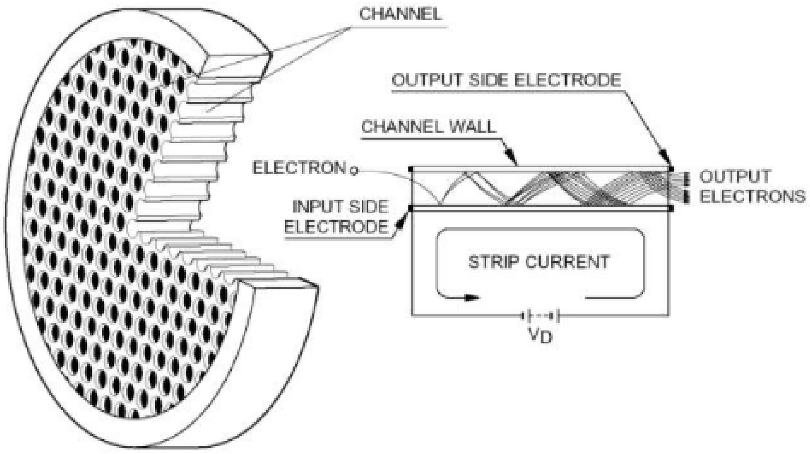

Figure 2.4: Scheme of the working principle of a MCP-PM

These channels form an array in a few mm thick glass plate. The inner channel walls have a proper electric resistance and secondary electron emission properties. The electrons are then accelerated along the channel where the avalanche takes form. The multiplication depends exponentially on $length/diameter$. Each channel have a typical gain of 10^4. Higher gain, $\sim 10^8$, can be reached putting two or more MCP in series.

In previous studies using an MCP-PMT[2], with an internal structure made of two MCP in series, coupled to a plastic scintillator of $3 \times 2 \times 2\ cm^3$, a time resolution of $\sim 125\ ps$ in a cosmic ray setup has been achieved [18].

Standard PM and MCP have a lot of good qualities. Standard PMs have high gain, low noise, high efficiency, and are really common and known detectors; some disadvantage are the non linearity, non uniform response and the fragility. MCP-PM have also high gain and efficiency and excellent time resolution; the drawback are the fragility and the cost. Moreover, the most important drawback of both kind of PMs is that they cannot be used in environments with high magnetic fields, since they are sensitive to that.

So more and more experiments are searching for detectors that can cover large areas (as in the present LHC experiments) with good performances and insensitivity to magnetic field. Other important features are a good time resolution, high efficiency, low cost, single photo detection capabilities, high gain with low voltage. Silicon PhotoMultiplier (SiPM) satisfies all these characteristics. First they are insensitive to magnetic field up to at least $7\ T$. Moreover they are insensitive to ionising radiation, i.e. nuclear counter effect, they are compact and robust, they have a low power consumption $\sim 50\ \mu W/mm^2$. The radiation hardness is about $2 \cdot 10^{10}\ n_{eq}/cm^2$ but it can be improved moving away the detector from the scintillator by means of optical fibres. There are several *R&D* projects ongoing so that different producers are available. A comprehensive review of SiPM detectors is given in Section 2.7.

2.3 Gaseous detectors

A gas-filled detector is based on the process of ionisation of the gas, following the passage of particle through it; then the electron-ion pairs created during this process are collected with an applied electric field [1–3, 14, 19]. Since the broad argument, in this section we will focus on only a certain kind of gaseous detector, optimised for timing measurements. The low density of the gas is the main limitation of gaseous detectors but the advantages are the possibility to have avalanche formation even due to a single electron (high mobility), the low price, the simplicity of operation and maintenance.

---

[2] Photonis MCP-PMT Image Intensifier PP0365E

2.3.1 General properties

In a gaseous detector the process starts with inelastic collisions between the incident particle and the gas molecules with the creation of electron-ion pairs. In a detector of thickness d, the number of primary interactions follows a Poisson distribution, see Eq.1.23, with a mean value:

$$\nu = \frac{d}{\lambda} \tag{2.7}$$

with λ the mean free path of particles. We already calculated the number of electron-ion pairs created by a MIP in Eq.1.7, considering a required energy to create an electron-ion pair of $\sim 37\ eV$; for a mixture of $C_2H_2F_4$ we got about 2 electron-ion pairs for a thickness of 250 μm.

2.3.1.1 Diffusion and drift velocity

In the absence of electric field, the created electrons and ions, at a certain temperature T, follow a Maxwell-Boltzmann distribution; the (thermal) electron average kinetic energy E_k and velocity of diffusion v_{diff} are:

$$E_k = \frac{3}{2}kT \tag{2.8}$$

$$v_{diff} = \sqrt{\frac{3kT}{m_e}} \tag{2.9}$$

, with k the Boltzmann constant and m_e electron mass. The velocity is isotropic; denoting the diffusion coefficient $D = \frac{1}{3}v_{diff}\lambda$ the fraction of particle at a certain time and position $\frac{1}{N_0}\frac{dN}{dx}$ follows a Gaussian distribution, see Eq.1.21, with $x_0 = 0$ and a standard deviation $\sigma = \sqrt{2Dt}$.

With an applied electric field, the charged particle will move in the direction of the electric field E with a drif velocity:

$$\mathbf{v_{drift}} = \mu\mathbf{E} \tag{2.10}$$

with μ the mobility of the particle which depends both on particle itslef ($\mu_{ion} \sim 1\ cm^2\ V^{-1}s^{-1}$ and $\mu_{electron} \sim 10^3\ cm^2\ V^{-1}s^{-1}$), and on the gas and its condition (temperature, pressure). Higher electric field will increase the electron drift velocity until it saturates due to collision with gas molecules. In Figure 2.5 the drift velocity in function of the electric field for several gases is reported.

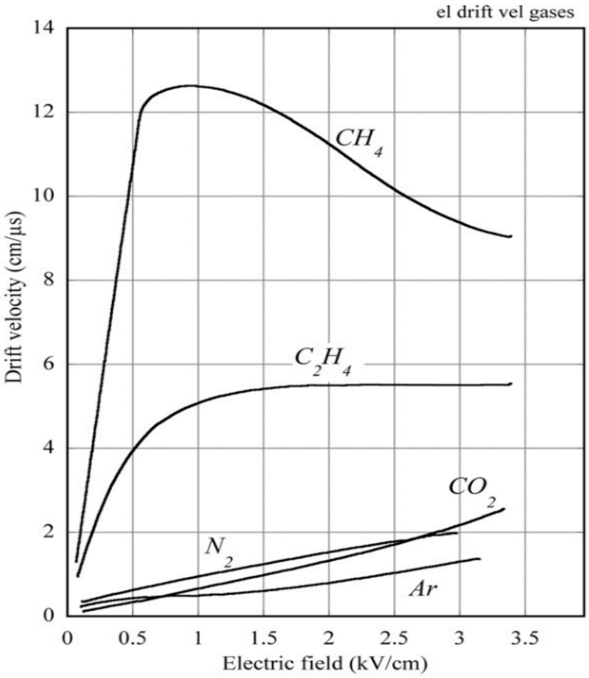

Figure 2.5: Electron drift velocity versus electric field for various gases.

2.3.1.2 Avalanche process

When the electric field is increased above $\sim kV/cm$ the primary electron created can acquire enough energy to produce inelastic collision, excitation, ionisation. If the energy of electron[3] is bigger than the ionisation potential of the molecules, it can further ionise and create secondary electrons and so on. This process is called avalanche and is described by means of the first Townsend coefficient[4], i.e. the number of ion pairs created per unit length α:

$$\alpha = \frac{1}{\lambda} = N\sigma \tag{2.11}$$

with λ the mean free path before ionisation, N the number of molecules per unit volume and σ the cross section. If dn is the increased number of

---

[3] We are talking only about the electron and not the ion because, due to the lower mobility, the velocity of ion is too low to produce further ionisation ($v_{ion} \sim cm/ms$, $v_e \sim cm/\mu s$).

[4] With electronegative gases, an important parameter is the attachment coefficient η, which considers the probability of electrons to be captured from the gas. Given this, the Townsend coefficient α is replaced by $\alpha - \eta$, i.e. the effective Townsend coefficient. A side effect of the attenuation is also a bigger fluctuation in the number of carriers.

electrons after a path dx, we have $dn = n\alpha dx$; for a uniform electric field[5] the number of electrons in a certain position and the charge multiplication (gain) factor G are:

$$n = n_0 e^{\alpha x} \tag{2.12}$$

$$G = \frac{n}{n_0} = e^{\alpha x} \tag{2.13}$$

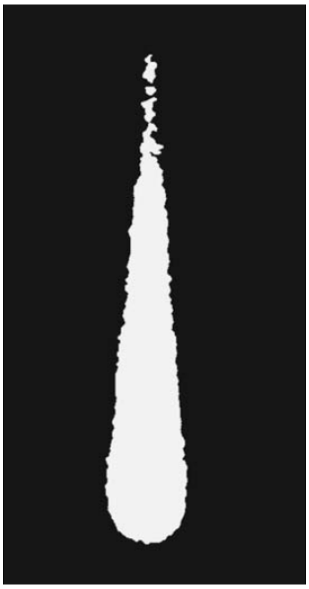

Figure 2.6: Reproduction of a detector avalanche in a cloud chamber.

Due to a lower velocity of ions, the avalanche charge distribution takes the typical drop-like form, see Figure 2.6, with the electrons at the front and ions at the tail.

If the gain is too high the avalanche can then transit to streamer mode, due to secondary processes like photon emission (from the atoms de-excitation). The streamer, if not dumped (from geometry or reduction of electric field), can bring to a spark breakdown. This breakdown can have destructive effects and can cause a big amount of dead time (see Section 1.4.1.3).

The point of transition between avalanche and streamer modes is called the Raether limit, and it consists in:

$$G < 10^8 \quad , \quad \alpha x < 18.42 \tag{2.14}$$

---

[5] Otherwise α would be a function of position $\alpha = \alpha(x)$. However for the detector treated here we can consider it independent of the position.

2.3.1.3 Signal formation

As reported in Chapter 1, in these kind of detectors the signal is formed as consequence of charge motion. In an uniform electric field, in a parallel electrode geometry, at a distance d, the induced signal can be obtained by Ramo's theorem, see Equations 1.32-1.34. Let's see for a specific case of gaseous detector.
To simplify the calculation, consider that at time $t = 0$ we have n_0 pairs produced at the cathode surface and the electrons start moving toward the anode (taking in total a time $t_- = d/v_-$) with a velocity v_- and are subject to the avalanche process. The induced charge and current, can be written, using Eq.2.12:

$$q_-(t) = \frac{en_0}{\alpha d}(e^{\alpha v_- t} - 1) \simeq \frac{en_0}{\alpha d} e^{\alpha v_- t} \tag{2.15}$$

$$i_-(t) = \frac{en_0 v_-}{d} e^{\alpha v_- t} \tag{2.16}$$

, with e electron charge. Then, after a time t_-, the total charge induced by the electrons, or rather the fast signal in an avalanche counter, is

$$Q_F = q_-(t_-) = \frac{en_0}{\alpha d} e^{\alpha d} \tag{2.17}$$

It is useful to know the fraction of fast signal, Q_F, compared to the total signal, Q_T. The total current induced is the sum of both the contributions of electrons and ions:

$$i(t) = i_-(t) + i_+(t) \tag{2.18}$$

The induced charge and current, due to ion movement, with the approximation $v_+ \ll v_-$, and considering that, while the exponential grows during electron avalanche, they are collected from cathode, can be written (at $t > t_-$) as:

$$i_+(t) = \frac{en_0 v_+}{d}(e^{\alpha d} - e^{\alpha \frac{d}{t_+ + t_-} t}) \tag{2.19}$$

$$q_+(t) = \frac{en_0 v_+}{d}\left((t - t_-)e^{\alpha d} - \frac{t_+ + t_-}{\alpha d}\left(e^{\alpha \frac{d}{t_+ + t_-} t} - e^{\alpha \frac{d}{t_+ + t_-} t_-}\right)\right) \tag{2.20}$$

, with $t_- + t_+$ drift time of ions (with $t_- << t_+$).
At the end of the process ($t = t_- + t_+$) the total charge Q_T is then:

$$Q_T = Q_F + q_+(t_- + t_+) = en_0 \, e^{\alpha d} \tag{2.21}$$

Figure 2.7 shows the total induced charge; it is evident the fast rise contribution due to electrons, and then the slower rise due to the ion motion.

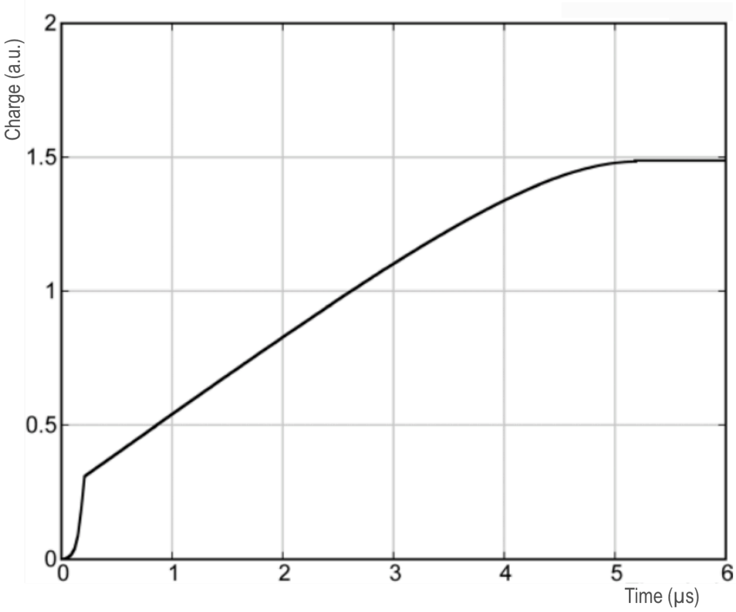

Figure 2.7: Total cathode induced charge by the avalanche multiplication [19].

The fast signal fraction of the total charge is:

$$\frac{Q_F}{Q_T} = \frac{1}{\alpha d} \tag{2.22}$$

So to get a large signal and then a good time resolution with gaseous detectors, it is important to have a large αd without exceeding the Raether limit (see Eq.2.14).
An other key parameter for a good time resolution is to limit the signal fluctuations; it is then relevant the immediate beginning of the avalanche (multiplication) as soon as the primary electrons are realesed; in this way there is no delay with the charge signal detected on electrodes [19] [6]. This is obtained in the Parallel Plate Chamber (PPC), realised in the 50's.

2.3.2 PPC and RPC

The Parallel Plate Chamber [20] is a parallel conductive electrode chamber; the electrodes are typically distant 2.5 *mm* (*gas gap*) and the chamber is filled with a mixture of argon and xylene under a pressure of 500 *mbar*. This

---

[6] E.g. this is not valid for a wire chamber, in which the avalanche starts when the electron arrives in proximity of the wire.

chamber works in streamer mode; with this kind of chamber it was possible, thanks to large signals, to get an efficiency of 95% and a time resolution of $200 - 400\ ps$. The drawback of this chamber is the critical operation: after the avalanche, the charge generated neutralises in the conductive electrodes, with discharges, causing a dead time deeply limiting the rate of particles detectable and which is propagated in the whole detector (due to low resistivity); the streamer has to be dumped by interrupting the voltage for a certain time (efficiency losses). One possible solution to avoid transition to streamer could be simply to keep a low gas gain; on the other hand this would causes a smaller signal, spoiling both the efficiency and time resolution.

To avoid this, the idea is to use high resistive electrodes (e.g. bakelite, about $10^{10}\ \Omega cm$) instead of conductive electrode, as realised in the Resistive Plate Chamber (RPC) [21]. The time needed by the electrodes to recharge is related to the resistivity; in particular, with a high resistivity, and then a low conductivity, a localised charge is ensured; in this way it is not needed anymore an external dumping of the multiplication (as in PPC), but rather the localised field drop is enough to ensure a discharge mode, avoiding streamer. For this reason the external surfaces of electrodes, of thickness $\sim 2\ mm$, were covered by graphite (resistivity $\rho \sim 200\ k\Omega/square$) that also distributes the voltage.

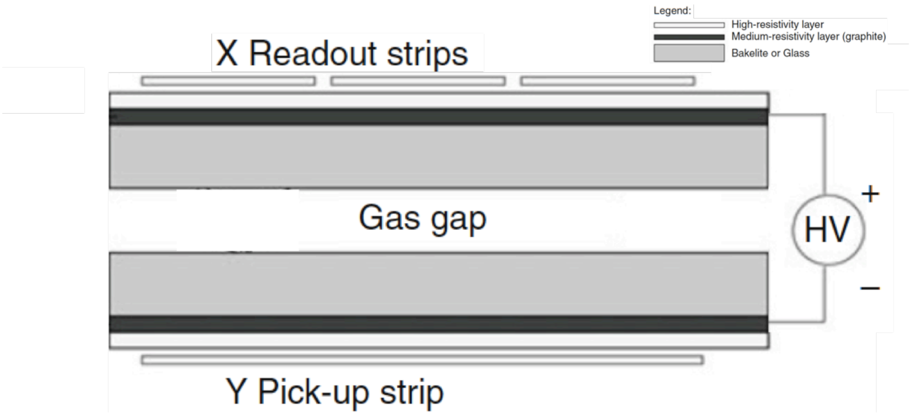

Figure 2.8: Schematic view of an RPC.

An important feature for time resolution is to have a high and uniform voltage on the whole detector; when the voltage is applied to the external coating, the movement of the charges through the electrode bulk, cancels the external electric field so that the voltage is applied across the gas layer. Another huge advantage of this kind of electrodes is the easy availability and the low cost. In Figure 2.8 a schematic view of an RPC.

To have a good time resolution it is also important a stable gain (lower current fluctuations), and then the choice of the gas mixture; a heavy gas for high efficiency is important (e.g. freon $C_2H_2F_4$) and an electronegative gas, to capture free electrons forming negative ions that cannot induce more avalanche (e.g. SF_6 or freon again).

As electrode material, instead of bakelite, glass sheets are an alternative; they are characterised by a resistivity $\rho \sim 10^{11} - 10^{12}\ \Omega cm$ and have a surface quite smooth, but with respect to bakelite electrodes, they have a lower rate capability.

The RPC can reach a high efficiency $\sim 99\%$ and a time resolution of $1\ ns$.

A thinner gas gap ($\ll 2\ mm$), with a high field for multiplication, reduces statistical fluctuations in avalanche development and then improves the time resolution. The problem is that, with a gas gap of e.g. $200\ \mu m$, the efficiency is lower and has to operate at a high gas pressure to maintain the same performance.

So, to have both excellent efficiency and time resolution a possible solution was found: the Multigap Resistive Plate Chamber (MRPC) [22].

2.4 Multigap Resistive Plate Chamber

As the name suggests, an MRPC is an RPC divided in more than one gas gap, by means of electrodes (glass sheets). The voltage is applied only on the external plates while the intermediate ones are left floating and reach a potential equilibrium dynamically. Fishing lines are stretched across gaps as spacers and they allow a gain uniformity and prevent deformation due to electrostatic force. In Figure 2.9 a schematic of a three-gaps MRPC; the external pick up electrodes are also visible .

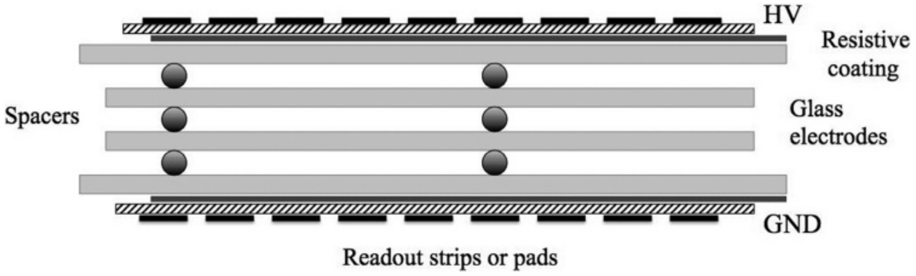

Figure 2.9: Schematic view of a three gas-gap MRPC. [19]

MRPC are able to reach a time resolution in the order of few 10's of ps; more than this, they have an efficiency of $\sim$ 99% with gas at atmospheric pressure, are easy to construct and relatively cheap, they work in avalanche mode with a high gain ($\sim 10^7$), and they have a rate capability ($\sim 1\ kHz/cm^2$) equivalent to the standard (2 mm; avalanche mode) RPC, but with a much lower power dissipation.

Thanks to their excellent time resolution these detectors are used in various experiment, e.g. for particle identification through Time Of Flight (TOF) [23] in the ALICE[7] experiment at LHC. In Section 2.5 a detailed description of the ALICE-TOF detector is reported.
Below a deeper explanation of MRPC operation [24–26] is reported.

2.4.1 Operation

To better understand the MRPC operation let's start considering a single gap MRPC, i.e. the RPC. As said, avalanche mode, compared to a streamer mode, has several benefits; for example an Argon filled (MIP $\sim$ 3 $cluster/mm$) RPC, would have an efficiency of $\sim$ 50%.
Let's do an overestimation, neglecting the fact that pick up signal electrodes are located outside of resistive electrodes plates [8]. To operate a 2 mm RPC in avalanche mode, for the Raether limit (see Eq.2.14), the Townsend coefficient has to be $\alpha < 9.2\ mm^{-1}$ ($1/\alpha d \sim 0.054$). So that, an electron starting at the cathode, will produce an avalanche of 10^8 electrons by construction; from Eq.2.22, the fast signal will be $Q_{F,2mm} = Q_T/\alpha d = 10^8 \cdot 1.6 \cdot 10^{-19} \cdot 0.054 \simeq 900\ fC$. An electron that starts at 0.25 mm from cathode will produce a fast signal ten times smaller $Q_{F,1.75mm} = 10^7 \cdot 1.6 \cdot 10^{-19} \cdot 0.054 \simeq 90\ fC$. This has to face with reality: in practice indeed, a reasonable lower threshold of charge at the discriminator can be $\sim 100\ fC$ so that only the electron produced in the first 250 μm from cathode can be detected. Knowing that in average in Argon we have 0.75 cluster per 250 μm, the efficiency of RPC in avalanche mode would be (using Eq.1.23) :

$$Eff = 1 - P(0) = 1 - \frac{0.75^0}{0!} e^{-0.75} = 53\% \qquad (2.23)$$

If, instead of Argon, a higher dense gas is used, like $C_2H_2F_4$, the efficiency would be 87% ($MIP_{Freon} \sim$ 2 cluster per 250 μm), still quite low. Moreover,

---

[7] A Large Ion Collider Experiment

[8] A bakelite sheet of 2 mm has a dielectric constant $\sim$ 2 so that the signal induced is reduced of a factor 2.

the RPCs, due to the (mechanical) variation of the gap width over the detector, are quite unstable; indeed a different width would have as a consequence a different gain.
With MRPCs this problem is solved: they can work with an high efficiency and time resolution, in perfect avalanche mode with a high and quite stable gain of about 10^7, maintaining tolerance in the gap size.
Then how is it possible; considering that the 10-gap, MRPC in ALICE-TOF have an electric field $E \sim 100\ kV/cm$, $\alpha = 126.8\ mm^{-1}$, $\eta = 8.2\ mm^{-1}$, $v = 21.62\ cm/\mu s$, $d = 0.25\ mm$ so that the multiplication factor should be $G \sim 7.5 \cdot 10^{12}$. It would be an enormous charge, but is not what is experimentally seen. This is due to the space charge effect that saturates the avalanche[9].
The space charge is due to the ions that during the avalanche stay there for a longer time than electrons, due to their slower drift velocity; moreover, the electrons, in the meanwhile, when reaching the anode, produce a drop on the electric field, creating some negative ions. The charge separation between electron and ion clouds produce an electric field opposite to applied field E,

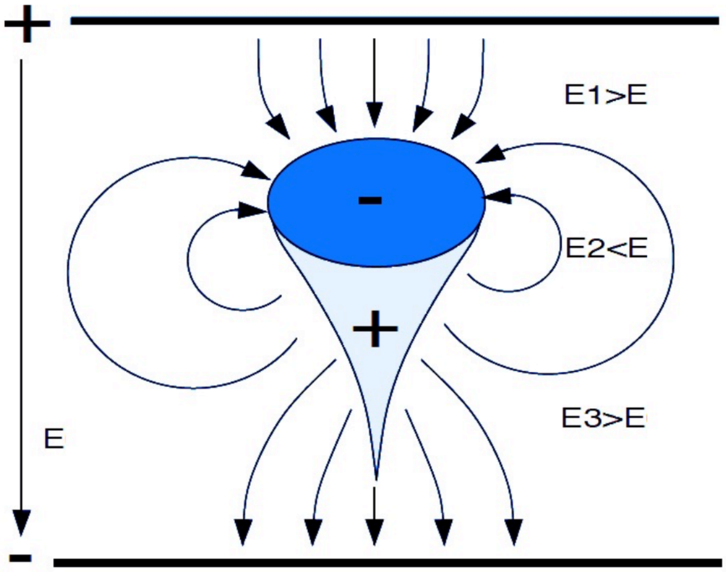

Figure 2.10: Space charge effect; during the avalanche process, with more and more slow ions, the effective electric field decrease at the avalanche core and the avalanche saturates.

---

[9] The space charge effect is present both in RPC and MRPC; anyway with smaller gas gaps, like in 250 μm MRPC, the space charges effects becomes larger.

which becomes lower and then saturate the avalanche and charge, see Fig. 2.10.
So the space charge plays a significant role: it ensures the avalanche mode, with a maximum avalanche limited to $\sim 1.6 \cdot 10^7$.
It also permits an easy construction, because the tolerance on the gap size of an MRPC of 250 μm is in the order of $10's\ \mu m$. For a PPC the tolerance was an important key to avoid discharge and permit stability; indeed it was found [27] that for a thickness of 1.5 mm the tolerance was 5 μm. If it scales with gap size, for a 250 μm the tolerance would be 1 μm and this would make the construction of the detector not easy at all. However, thanks to saturation of charge, is not like this; indeed, if the gas gap is smaller of 5% the electric field would be bigger of 5% but the maximum avalanche would be the same; so the only consequence is to make the avalanche grow quicker.

2.4.2 Rate capability

Now we can also explain the reason why the rate cabability of the MRPC, with a glass resistivity $\rho = 5 \cdot 10^{12}\ \Omega cm$, is limited at about 1 kHz/cm^2 [28–30].
To simplify the explanation let's start considering a single gas gap; when the voltage is applied to one glass electrode (which can be considered an amorphous semiconductor), the movement of charge through the electrode bulk, cancels the external electric field so that the voltage is applied directly to the gas gap, while inside the glass sheet there is no electric field. Thus one surface will be charged by negative charge, electrons, and the other by positive charge, holes.
When a particle passes through the detector creating electron-ion pairs, these charges will deposit onto the surface of the resistive plates, causing a voltage drop, limited to a small area large as the avalanche size. In particular the exhaust time needed to decay or rather the time constant describing the process $e^{-t/\tau}$, is related to resistivity of the glass so that $\tau = \epsilon_0 \epsilon_r \rho =$ 3.5 s. This for the case of ALICE-TOF, with $\rho = 5 \cdot 10^{12}\ \Omega cm$, $\epsilon_r = 8$, $\epsilon_0 = 8.854 \cdot 10^{-12} C/Vm$.

The voltage drop for low rate will not affect the functionality of the chamber; it will start to do so when the electric field will cause an amplification lower than 10^7, almost the limit for saturated amplification. When this happens, the process in the chamber will change, causing a lower gain and then worst efficiency and time resolution.

For a gas gap thickness of 0.25 mm, from $10^7 = e^{(\alpha-\eta)d}$ the corresponding limit for the effective Townsend factor is $(\alpha - \eta) \sim 65$. Looking at the Figure

2.11, this value corresponds to an electric field of about $E = 80\ kV/cm$ and then to a voltage of $V_{Eff} = E\ d = 2\ kV$.

As an example, in the ALICE TOF case (see Section 2.5), the voltage applied for single gap is about $V_{Appl} = 2.5\ kV$, with $E = 100\ kV/cm$, $\eta = 8.2\ mm^{-1}$ and $\alpha = 126.8\ mm^{-1}$. The voltage drop, per unit area, for a charge of $Q = 2\ pC$, 2 electrodes of thickness $s = 0.04\ cm$, is:

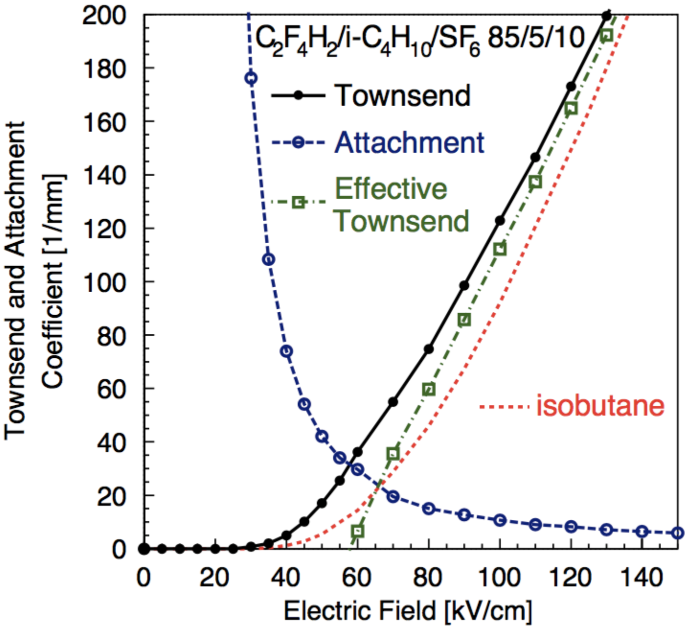

Figure 2.11: Townsend, effective Townsend and attachment coefficients with and without isobutane in the gas mixture [31].

$$\Delta V = 2s\rho Q\ Rate \tag{2.24}$$

So, the maximum voltage drop $\Delta V_{max} = V_{Appl} - V_{Eff} = 500\ V$ correspond about to a rate of $1\ kHz/cm^2$.

2.4.3 Final consideration on timing

The excellent time resolution of the MRPC can than be understood from the following considerations.

The time resolution on a single gas gap is proportional to:

$$\sigma \sim \frac{1}{(\alpha - \eta)v} \tag{2.25}$$

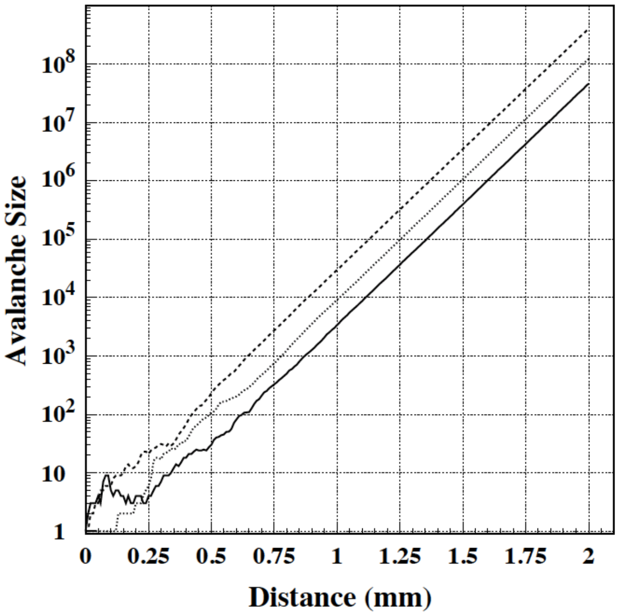

(a)

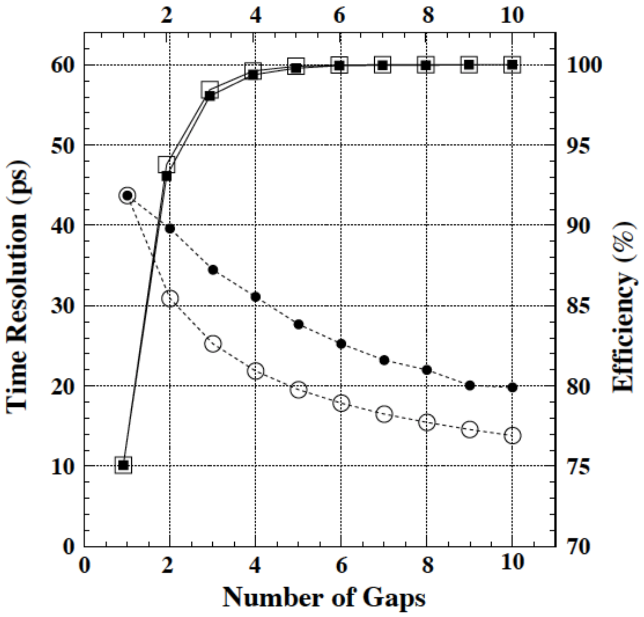

(b)

Figure 2.12: (a) Avalanches started by a single electron at $x = 0$ for a $\alpha = 13\ mm^{-1}$, $\eta = 3.5\ mm^{-1}$ in an RPC of 2 mm. It can be noticed that the very beginning of the avalanche decides on the final avalanche size. Once the number of electrons is sufficiently large the avalanche grows like $e^{(\alpha-\eta)d}$. (b) Efficiency (black squares) and time resolution (black circles) versus number of gas gaps (300 μm). The open circles represent the time resolution expected from a simple scale $1/\sqrt{n}$, with n the number of gaps. The open squares represent the efficiency expected from a scale reported in [24].

with v the electron drift velocity and $(\alpha - \eta)$ the effective Townsend coefficient. To maintain the same gain for a smaller gap size, in order to increase $(\alpha - \eta)$ (indeed the avalanche has a smaller distance to grow in, $(\alpha - \eta) \sim 1/gap\ size$), a higher electric field is needed, with a consequently higher velocity. Then, for thinner gap size, the time resolution improves.

The time resolution in an MRPC is also strictly related to the fluctuation on the rise time, which is related to the fluctuation in the avalanche; this is dominant at the level in which the avalanche is still small (as anticipated in Section 1.5.2), see Figure 2.12(a) for the case of a RPC of 2 mm. The avalanche has a stochastic behaviour until it reaches about 100 electrons; the behaviour becomes then deterministic, with an exponential grows. Then, in an MRPC, it reaches the saturated limit, due to the space charge effect.

So the time resolution will depend mostly on the first part of the avalanche, the stochastical one which correspond to the landau fluctuations; this can explain such a good time resolution in the MRPC. Indeed the MRPC Landau fluctuations are smaller. To understand it, consider that along the path an electron ionises each λ $(= 1/\alpha)$, the mean free path; in particular we have to point out that an *average* avalanche has an ionising collision every λ while an *individual* avalanche may not. Then the fluctuations (or rather the error) for more gas gaps, like in MRPC, is smaller than for a single gap. Anyway, the time resolution is then dominated by the gas gap with larger (and faster) signal. In Figure 2.12(b) the improvement of the time resolution with the gas gaps number is shown.

As a last consideration, for time measurement with the MRPC it is important to understand if the space charge affects the resolution; this was studied by Lippmann and Riegler in [31]. They concluded that the space charge affects the rise time, adding a shift in the mean time, but the effect on time resolution is negligible because this shift is similar for all signals.

2.5 ALICE–TOF

The Time Of Flight (TOF) is one of the ALICE detector and it is based on MRPC technology.

The ALICE (A Large Ion Collider Experiment) [32–34] experiment at CERN LHC (Large Hadron Collider) [35] has been designed to study the ultra-relativistic $Pb - Pb$ collisions. One of the purpose of ALICE is to gain a better understanding of QCD[10] matter produced in high-energy collisions. In fact, based on lattice calculations [36], at energy densities over 1 GeV/fm^3

---

[10] Quantum Chromo-Dynamics, the theory of strong interactions of the Standard Model

or at a temperature above $\sim 155\ MeV$, QCD predicts a new state of matter: the Quark-Gluon Plasma (QGP). In this state quarks and gluons are not confined inside the hadrons and chiral symmetry is partially restored, i.e. the quarks assume their current masses.

Such a high energy densities can be reached via high-energy nuclear collisions; in this way a QGP *fireball* is created and it immediately starts to expand and cool down. In this process, once the chemicals freezout temperature has been reached, particles with zero colour are formed and the composition is fixed; later on, at the kinematic freezout temperature, kinematic properties of all the particles are defined.

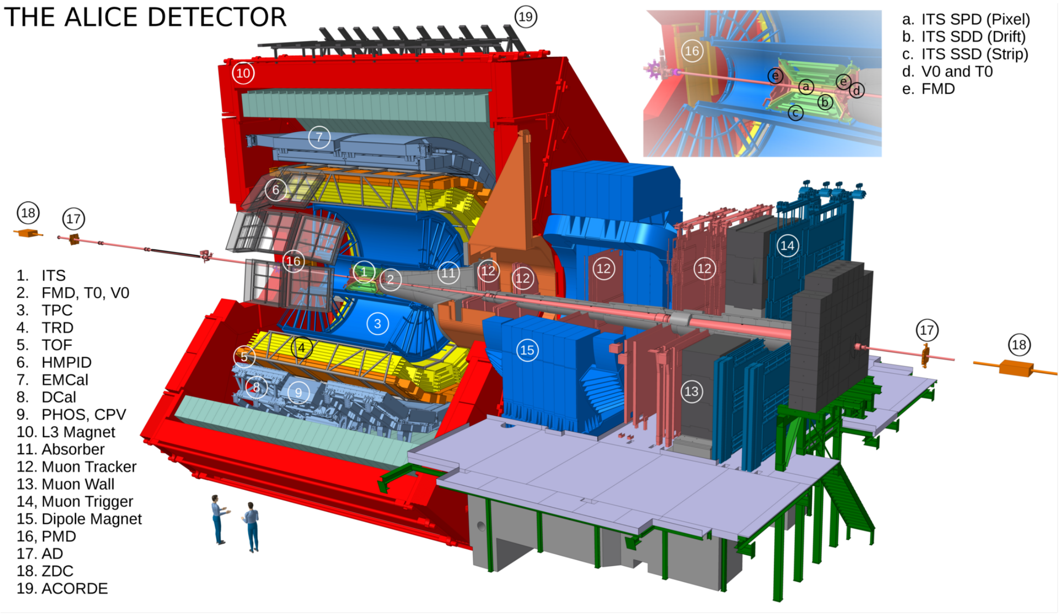

Figure 2.13: Schematic layout of the ALICE detector.

Since the start of operation in 2009, at LHC two running periods have been performed: Run1 (2009-2013) and Run2 (2015-nowadays), at energy per nucleon of $Pb - Pb$ collision of $\sqrt{s_{NN}} = 2.76\ TeV$ and $\sqrt{s_{NN}} = 5.02\ TeV$ respectively. An energy density and temperature of $\sim 12\ GeV/fm^3$ and $\sim 297\ MeV = 3 \cdot 10^{12}\ K$ have been measured respectively [34]. The fireball reached a volume of $\sim 300\ fm^3$ and a lifetime of $\sim 10\ fm/c$.

Many different results have been obtained from the collected data, contributing to a deeper understanding of the QGP properties (see a summary in [33]). Proton-proton (pp) and proton-nucleus ($p - Pb$) collisions are also analysed in ALICE; these events are studied not only because they are interesting in themselves, but also because they represent an important reference to better

disentangle the QGP properties in Pb-Pb. In fact these measurements also serve the purpose to separate the real QCD-matter signals from the cold-matter initial and final state effects.
Recent measurements [37] in pp and $p-Pb$ show phenomena that have been seen before only in $Pb-Pb$ (central) collisions. This seems to challenge some of the traditional distinction between the three systems. These results instead suggest a similar underlying physics and are leading to a better description of all multiparticle systems generated in hadronic collisions.

The ALICE experiment, shown in Fig.2.13, has a size of $16 \times 16 \times 26\ m^3$ and it weighs 10000 t; it consists of a central barrel detector system installed inside a large solenoidal magnet, which generates a magnetic field of 0.5 T, and several forward detectors.
The Inner Tracking System (ITS) and the Time Projection Chamber (TPC) are the main charged-particle tracking detectors of ALICE . The ITS is made of six layers of silicon detectors with three different technologies and resolutions (two pixel SPD, two drift SDD and two strip SSD). The TPC is a large (90 m^3) volume gas detector.
While electroweak interacting particles (photons, Z, W, . . .) pass the dense/hot medium unchanged, hadron production is strongly affected. Particle identification (PID) is then essential, as many observables are either mass or flavour dependent. ALICE makes use of almost all known PID techniques: specific ionisation energy loss (TPC, ITS), time-of-flight (TOF), transition (TRD) and Cherenkov (HMPID) radiation, electromagnetic calorimetry (EMCAL) and muon detectors (MCH).
Particle identification at low and intermediate momenta is of crucial importance since the majority of the produced charged primary particles is emitted in this range. In ALICE the range on momenta spans between a minimum 0.15 GeV/c to 20 GeV/c. In the central barrel, particle identification is performed by SDD, SSD at low momentum and by TPC up to the relativistic rise region. Hadron identification at intermediate momenta, up to 2.5/4.0 GeV/c for kaons/protons is better performed with the Time of Flight (TOF). The High Momentum PID (HMPID) extends the identification to higher momenta in a restricted solid angle. Electron and photon identification is performed with a Transition Radiation Detector (TRD) and, in restricted azimuthal regions, with an ElectroMagnetic CALorimeter (EMCAL, DCAL) and a PHOton Spectrometer (PHOS) based on crystals.
The forward region include the Photon Multiplicity Detector (PMD) and the silicon Forward Multiplicity Detector (FMD), which are dedicated to the measurement of photons and charged particles respectively. A muon spectrometer, with Muon TRigger (MTR) and CHambers (MCH), allows

an identification and a measurement of the muon momenta by means of an external dipole and an iron absorber equipped with proportional and RPC chambers. Detectors along the beam pipe are devoted to vertexing and trigger (V0), collision time (T0) and event centrality determination (V0 and the ZDC calorimeters).

The TOF [23, 38–41] is located at 3.7 m (5. in Fig.2.13) from the beam axis and covers with a large cylindrical array ($\sim$ 141 m^2 of active area) the central region ($-0.9 < \eta < 0.9$, with η the pseudorapidity[11]).
The TOF provides charged Particle IDentification (PID) in the intermediate momentum range, the minimum momentum threshold for particles to reach the TOF is $p_{min} \sim 0.3$ GeV/c. With a global time resolution of ~ 60 ps the system provides π/K and K/p separation better than 3σ up to a particle momentum of $p \sim 2.5$ GeV/c and $p \sim 4$ GeV/c respectively. The TOF also provides a trigger for cosmic ray events and ultraperipheral collisions.

2.5.1 The Time Of Flight technique

Particles are identified according to their mass and electric charge. While charge can be directly measured, the mass cannot. A magnetic spectrometer can measure the momentum by means of the rigidity $R = p/z$, where z is the charge of the particle. A simultaneous momentum and time-of-flight measure (and then velocity) can lead to an indirect mass measurement:

$$m = \frac{p}{c}\sqrt{\frac{c^2t^2}{L^2} - 1} \tag{2.26}$$

Thus two particles, i and j, with different masses but the same momentum will have a time difference after travelling a distance L:

$$\Delta t = t_i - t_j \simeq \frac{Lc}{2p^2}\left(m_i^2 - m_j^2\right) \tag{2.27}$$

The PID capability of a TOF detector is related to the number of standard deviations in the time-of-flight difference of two particles:

$$n_\sigma = \frac{\Delta t}{\sigma_{TOF}} \tag{2.28}$$

The magnetic field used to measure particle momenta could prevent low-momentum particles to reach the TOF array. For π/K a separation better

---

[11] It corresponds to $\pi/4 \leq \theta \leq 3\pi/4$. η is the pseudorapidity and it can be defined as $\eta = -\ \ln(\tan(\theta/2))$.

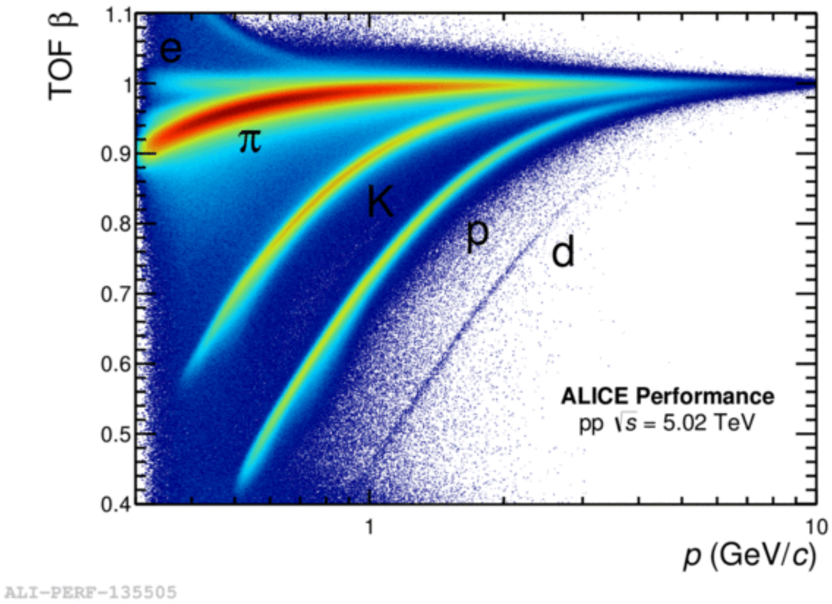

Figure 2.14: Time of Flight (β) measured by the ALICE TOF for pp interactions at 5.02 TeV.

than 3σ has been achieved for momenta below to 2.4 GeV/c while for K/p the separation extends up to 4 GeV/c. In Figure 2.14 a TOF measure for pp interactions at 5.02 TeV.

From Eq.2.26 the three contributions on mass resolution are evident:

$$\left(\frac{\delta m}{m}\right)^2 = \left(\frac{\delta p}{p}\right)^2 + \left(\gamma^2\frac{\delta L}{L}\right)^2 + \left(\gamma^2\frac{\delta t}{t}\right)^2 \qquad (2.29)$$

For high momenta the dominant term is $\delta t/t$ and then the mass resolution gets worse because of γ^2 factor[12].

2.5.2 Time resolution

The TOF time resolution is the result of several contributions:

$$\sigma^2_{TOF} = \sigma^2_{MRPC} + \sigma^2_{TDC} + \sigma^2_{FEE} + \sigma^2_{Clock} + \sigma^2_{Cal} \qquad (2.30)$$

where σ_{MRPC} is the intrinsic resolution of TOF MRPC (in the order of 30 ps), $\sigma_{TDC} \sim 20 - 30$ ps and $\sigma_{FEE} \sim 10$ ps are the read-out and front-end

---

[12] This is easier to understand expressing γ^2 as $1 + \frac{p^2}{m^2c^2}$.

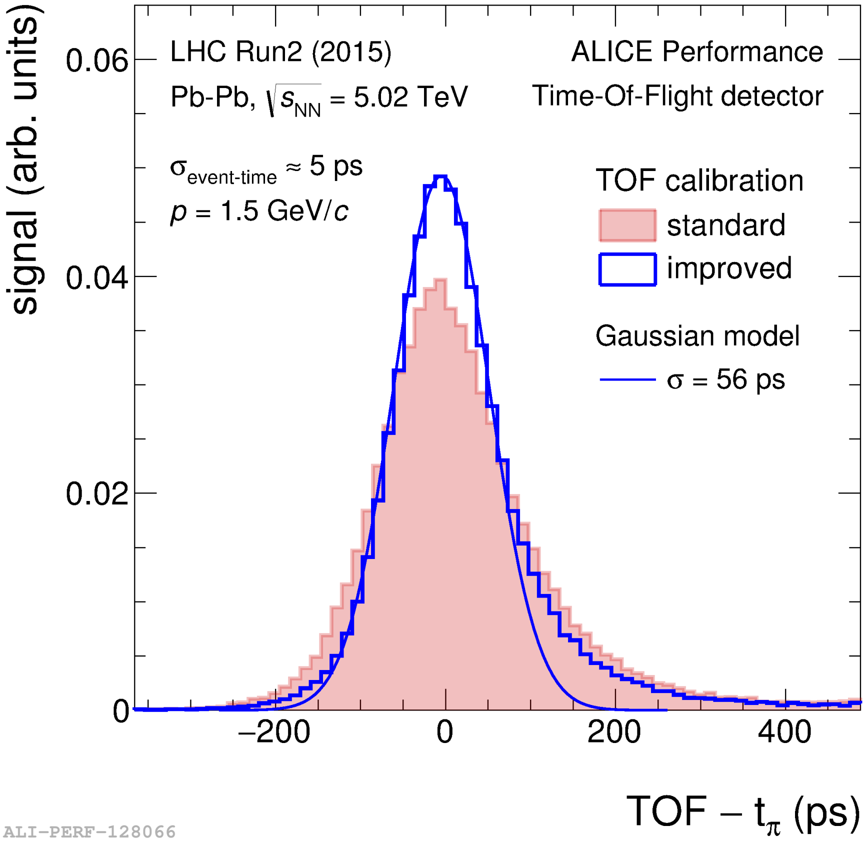

Figure 2.15: TOF time resolution of 56 ps in $Pb - Pb$ collisions at 5.02 TeV. Is underlined the recent improvement with a refined time-slewing calibration. The width of the signal distribution for pions at 1.5 GeV is measured in terms of the FWHM.

electronic time resolution, $\sigma_{Clock} \sim 20\ ps$ and σ_{Cal} are the LHC clock and calibration time resolutions; the calibration has several contributions, due to the calibration constant error, like for the length of cables, or for the time slewing calibration (see Section 1.5.3).

Moreover the total time resolution can be expressed as:

$$\sigma^2_{TOT} = \sigma^2_{TOF} + \sigma^2_{trk} + \sigma^2_{event-time} \tag{2.31}$$

σ_{trk} corresponds to the error on the tracking of the particle. Indeed after the particle is tracked by other ALICE detectors (mainly the TPC), this has also to be extrapolated to the active area of TOF; here a matching window of 3 cm for $Pb-Pb$ collisions (10 cm for $p-p$) is opened around the extrapolation point; the matching algorithm then searches for at least one signal and the nearest one is combined to the track. For momenta greater than 1 GeV/c this factor is negligible.
$\sigma_{event-time}$ is the resolution on the event time of collision; indeed to each time measured by the TOF a t_{event} has to be subtracted: $t_{TOF} - t_{event}$. The t_{event} has to be measured event by event, otherwise, due to the finite dimension of bunches that collide at LHC, it would lead to $\sigma_{event-time} \sim 80 - 200\ ps$. To avoid this, the ALICE $T0$ detector provides an accurate time measurement of t_{event}. However, the $T0$ detector has a limited acceptance; an alternative method to get a t_{event} is by using the TOF itself [42]. This is possible only when there are at least three TOF-matched tracks, assuming a common event start time. For 30 tracks[13] $\sigma_{event-time} \sim 25\ ps$. So the final t_{event} can be a weighted average with time resolution between $T0$ and TOF algorithms.

In conclusion, the PID with the TOF detector can be performed by a difference:

$$t_{TOF} - t_{event} - t_{exp_i} \tag{2.32}$$

with t_{exp_i} the expectation time for several masses ipothesis i $(\pi, K, p, \dots)$. This distribution should be centred on zero and with a σ_{TOT} standard deviation. In Fig.2.15 a $\sim 60\ ps$ time resolution has been reached in $Pb-Pb$ collisions at 5.02 TeV.

2.5.3 Layout

The TOF detector is inscribed in a cylindrical shell with an internal radius of 3.7 m and an external one of 3.99 m from the beam axis.

---

[13] Consider that for $Pb-Pb$ collisions the average number of particles reaching the TOF is ~ 600.

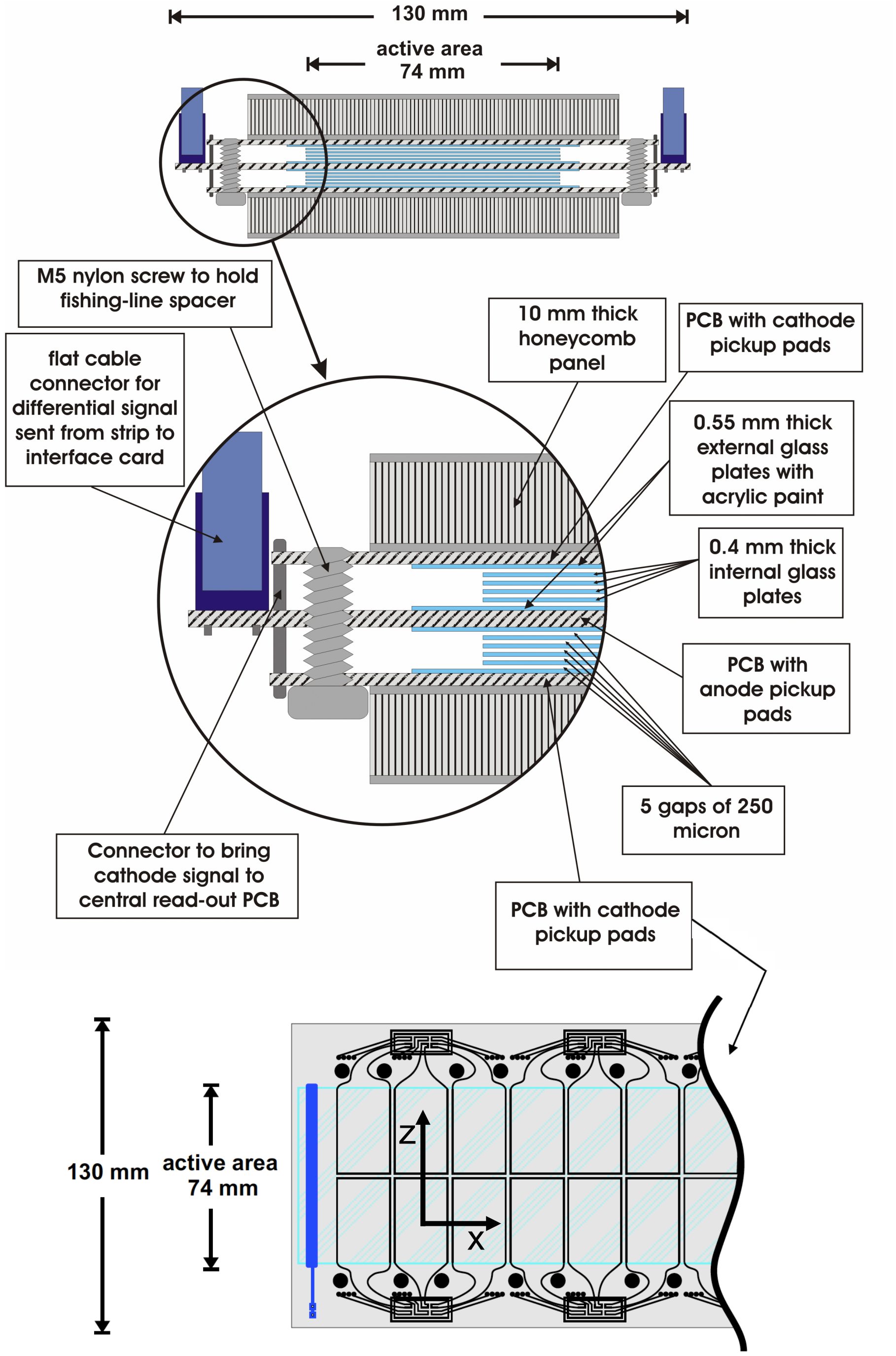

Figure 2.16: Schematic drawing (cross section and top view of the PCB) of the ALICE TOF MRPC strip.

The MRPC strip is the basic unit of the ALICE TOF detector, with a $120 \times 7.4\ cm^2$ active area.
A time of flight solution based on fast scintillators coupled to photomultipliers would have been completely impractical and prohibitively expensive; so the choice was a gaseous TOF detector. Nowadays, the use of Silicon PhotoMultipliers (SiPM) instead of the traditional vacuum PM, may allow this technology to be feasible.
The ALICE TOF array consists of 1593 MRPC strips. These strips are mounted in a gas-tight box through which the gas is circulated, with a gas mixture made of 93% $C_2H_2F_4$, 7% SF_6. The strips are tilted to face towards the interaction point so that the surface of a given pad is at the same distance from it.
A cross-section of an MRPC strip is shown in Fig.2.16. To guarantee low detector occupancy even in the highest charged-particle density scenario ($dN_{ch}/\eta = 8000$, with N_{ch} the number of charged particles and η the pseudorapidity) the MRPC strip is segmented into two rows of 48 pickup pads of $3.5 \times 2.5\ cm^2$, for a total of 96 pad for each strip and about 160000 total readout channels. There are both anode and cathode readout pads with a differential signal being sent to the front-end electronics. The TOF MRPC is based on a double-stack design: it is made of two stacks of five gas gaps instead of a single stack of ten gas gaps. The benefits of a double stack design is producing a signal twice as large as the single stack design and utilise a high voltage at half the value required for a single stack MRPC. Each gap has a width of 250 μm; the resistive plates are made with commercially available soda-lime float glass sheets. The external surface (facing the PCB) of the outer plates is painted with a resistive coating of a few $M\Omega/\Box$. This is used to apply the high voltage. The mechanical stiffness is guaranteed by two honeycomb panels, glued on the external PCBs. Connecting pins are soldered across the 3 PCB layers in order to bring cathode signals from the external PCBs to the central PCB, where anode signals are collected.

2.5.4 Electronics

The front end and read out electronics in the ALICE-TOF (see Section 2.5) are a key parameters for the excellent time resolution. As front end electronics the TOF uses a NINO ASIC chip, while an HPTDC as electronic readout.

NINO-ASIC An ASIC[14] chip has been developed for the front end of the ALICE-TOF: the NINO ASIC [43,44]. In Figure 2.17 a picture of the NINO-ASIC card is shown. This chip exploits the differential signals in output from the MRPC pads, with a consequent low noise. The tricky transfer of the signal from the NINO cards to the readout electronics is realised by means of shielded and optimised cables, the Skewclear Amphenol cables.
The NINO ASIC is a low power ultrafast amplifier and discriminator; it is a very compact chip ($2 \times 4\ mm^2$) and it has 8-channels. The NINO ASIC main characteristics, beside the differential input and LVDS[15] output signals, are:

- a leading edge of the output signal with a low jitter ($< 25\ ps$);
- a fast amplifier ($< 1\ ns$ peaking time);
- a low power consumption ($\sim 40\ mW/channel$);
- an output signal width correlated to the charge of the input signal: using of Time Over Threshold (TOT) method (see 1.5.3).

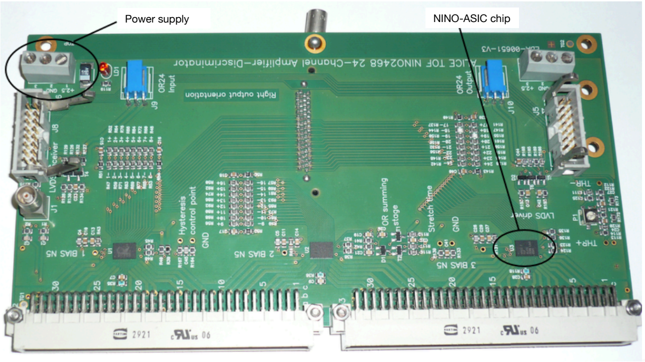

Figure 2.17: NINO-ASIC card with three chip visible.

To match the output signal (with a width between $2-7\ ns$) with the TDC used as readout electronics, the HPTDC, the signal has also to be stretched; indeed the HPTDC can simultaneously measure the leading and the trailing edges of a signal only if the width is larger than $6\ ns$.

---

[14] Application Specific Integrated Circuit

[15] Low Voltage Differential Signal

HPTDC The ALICE-TOF readout electronics is realised with a TDC readout Module (TRM) VME[16] card; it is based on an ASIC High-Performance Time-to-Digital Converter (HPTDC) [45]. As already said, it can measure the leading and the trailing edges of a signal only if the width is larger than 6 ns; the guaranteed (by NINO ASIC) input signal is 10 ns. This allows TOT measurements of the MRPC signal.
The only problem with HPTDC is that the time resolution is not as good as what we expected; indeed, even though the bin size is 25 ps, the observed time resolution is $(20 - 30)$ ps.

2.6 Silicon detectors

A silicon detector is a semiconductor device which basically is a solid state ionisation chamber. The difference mostly arises in the much higher density and on the reaction when a particle pass through it: instead of creating electron-ion pairs, it creates electron-hole[17] pairs. In the following we report the basics ingredients of silicon detectors [1,8,14,46].

2.6.1 General properties

2.6.1.1 Structure and drift velocity

Silicon is a semiconductor material based on a crystalline material whose outer-shell atomic levels exhibit an energy band structure.
A single atom in free space has quantised and discrete energy levels. When the atoms are arranged in a crystalline lattice, the electron wavefunctions overlap. This degeneracy in the outer-atomic shell energy levels breaks, due to Pauli principle; the discrete levels are now only slightly separated and form bands of states. The highest-energy band is the conduction band, where the electrons are free to move. The below band is the valence band, where the electrons are more tightly bound. The properties of a material arise from the bandgap energy E_g between the valence and conduction band; in an insulator E_g is large ($> 5\ eV$) while for a conductor there is no gap. For semiconductors there is an intermediate situation: the gap exists but has such a small

---

[16] Versa Module Europa

[17] A *hole* is a quasi particle which follows the Fermi-Dirac statistics. It is a lack of electron; as we will see, when an electron enters the conduction band leaves a hole in the valence band, which can be treated like an heavier electron. Hole motion corresponds to valence electron motion; here arises the different properties compared with a conduction electron.

size that the electrons can be excited by simple thermal energy to the conduction band. For silicon the value of the energy gap is 1.12 eV at 300 K. Silicon has four electrons in the valence band, is a IV type material; all participate in covalent bonding between atoms. At low temperature all valence electrons remain bound, staying in the valence band. At higher temperature, thermal vibrations may break the covalent bond turning out an electron free in the conduction band and leaving behind a hole in the valence band.
In an intrinsic semiconductor (pure material) the concentration of electrons in the conduction band n and of holes in the valence band p are the same, according to the mass action law:

$$n_i = n = p \tag{2.33}$$

The probability distribution of a state of energy E is then strictly related to temperature T and from Fermi-Dirac statistics:

$$f(E,T) = \frac{1}{1+e^{(E-E_F)/kT}} \tag{2.34}$$

with $k = 8.62 \cdot 10^{-5} eVK^{-1}$ Boltzmann constant and E_F Fermi energy. The Fermi energy is the highest possible energy of fermions at 0 K; for an intrinsic semiconductor it arises about in the middle of the gap (then it is shifted depending on the impurities).

The motion of a charge in a semiconductor is totally similar to the motion in gaseous material, both for diffusion and drift velocity, see Section 2.3.1. The main difference arises in the different mobility of the positive charge, the hole, which for silicon is only a factor three less than electron, $\mu_e = 1350\ cm^2\ V^{-1}\ s^{-1}$ and $\mu_h = 450\ cm^2\ V^{-1}\ s^{-1}$ at 300 K. In Figure 2.18 the drift velocity as a function of the electric field is shown; at the beginning it grows proportionally with constant μ (see Eq. 2.10) and then it saturates, above $E \sim 10^4\ V/cm$ (the mobility $\mu \rightarrow 1/E$). The saturated velocity is $\sim 10^7 cm/s$.

It has to be pointed out that in silicon the energy required to create a $e^- - h$ pair is not equal to the energy gap, 1.12 eV but it is rather larger. This because silicon is a semiconductor with an indirect bandgap structure; this means that when an electron of valence is excited to the conduction band, phonons are needed for momentum conservation. Then, the energy required to create an $e^- - h$ pair in silicon is $\sim 3.6\ eV$.

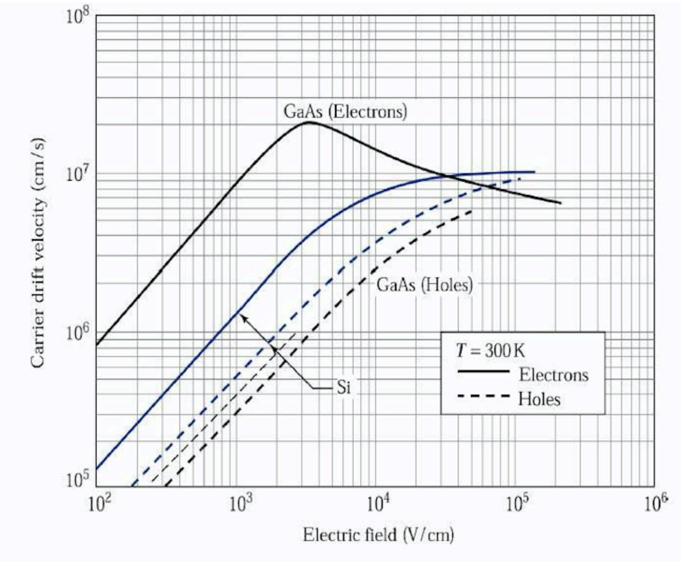

Figure 2.18: Drift velocity in silicon (and GaAs) versus electric field for both electrons and holes.

2.6.1.2 Doping

Intrinsic semiconductors are rarely used in semiconductor detectors; more often what is used is an extrinsic semiconductor, in which the electrical semiconductor properties are modified by adding some specific impurities, i.e. by *doping* the material. Depending on the dopant material, if it is a III (e.g. B, Ga) or V (P, As) type, one obtains respectively $p-type$ semiconductors with additional holes in the valence band (acceptors) or $n-type$ semiconductors with an excess of electrons in the conduction band (donors). At room temperature, and at the equilibrium $p \sim N_A$ and $n \sim N_D$, with N_A and N_D respectively the atomic concentration of acceptors and of donors.
Obviously for extrinsic semiconductors the same intrinsic concentration relation is not valid anymore; however, according to mass action law, the increase of majority carriers (electrons in the case of $n-type$ semiconductor) is compensated by a decrease of minority carriers so that :

$$n_i^2 = np = N_C N_V e^{-\frac{E_g}{kT}} \tag{2.35}$$

with N_C and N_V the effective density of states in the conduction and valence band.

The resistivity of a certain material, e.g. an n type, is given by:

$$\rho = \frac{1}{e\mu_e N_D} \tag{2.36}$$

Still, an extrinsic semiconductor can not be used exactly like it is to detect particles because the signal would be totally covered by thermally generated pairs. Indeed for a silicon intrinsic concentration $n_i = 1.45 \cdot 10^{10}\ cm^{-3}$, a thickness of $0.03\ cm$ and an area of $1\ cm^2$ the thermal pairs are about $n_i\ d\ A \sim 4.35 \cdot 10^8$. This has to be compared with a signal by a MIP which creates about $3.2 \cdot 10^4$ pairs (see Section 1.1.2.1), four order of magnitude less than the thermal ones. Somehow, to see the signal, these thermal pairs have to be reduced; there are two options, one is to reduce the temperature, which is quite unpractical, the other is to deplete the silicon volume from free charge by using a reverse biased $p-n$ junction.

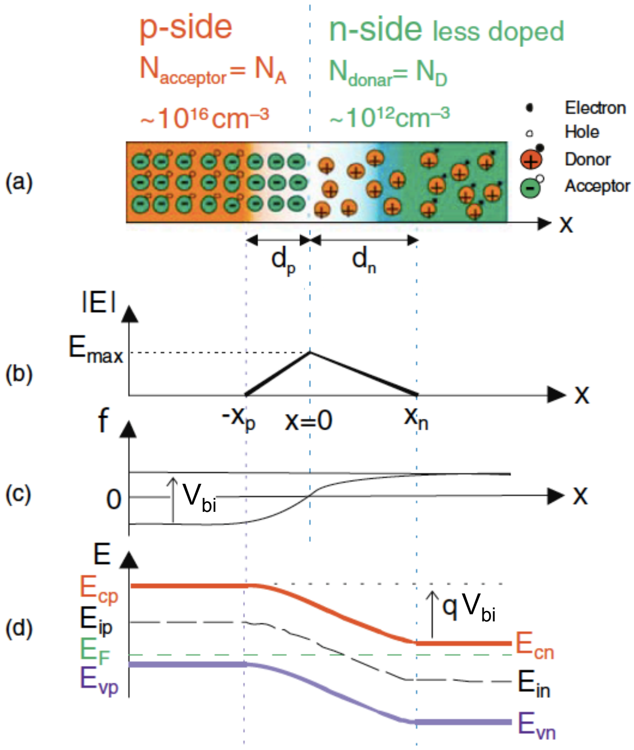

Figure 2.19: (a) A visualisation of the atomic configuration, (b)the electric field, (c)the electrostatic potential, (d) band diagram of the junction at equilibrium.

2.6.1.3 $p-n$ junction

A $p-n$ junction is a structure which shows diode characteristics. In Figure 2.19 a $p-n$ junction and its internal potential and electric field is depicted. Without application of an external voltage, when the bodies are brought in contact, the concentration gradient across the junction boundary will cause electrons to diffuse into the p region and holes in n region; in this way, immobile ions are left behind, in a *space charge* region, and this creates an electric field in opposite direction of the diffusion force, achieving an equilibrium between the two forces. The region of space charge is also called *depletion region.* The built-in voltage V_{bi} is basically obtained from the requirement that the Fermi levels have to line up in thermal equilibrium. For doping concentration $N_D \sim 10^{12}\ cm^{-3}$ and $N_A \sim 10^{16}\ cm^{-3}$, the built in voltage is $V_{bi} \sim 0.5\ V$ and the corresponding *natural* depletion region is $\sim 25\ \mu m$.

The width of the depletion region can be determined as described in the following. Starting from the Poisson's equation:

$$\frac{d^2V}{dx^2} = -\frac{\rho(x)}{\epsilon} = \begin{cases} \frac{eN_A}{\epsilon} & -x_p < x < 0 \\ -\frac{eN_D}{\epsilon} & 0 < x < x_n \end{cases} \tag{2.37}$$

with V the internal potential, $\rho(x)$ the charge density distribution, ϵ the dielectric constant and x_p, x_n are the lenght of the depletion region in the p and n side respectively, see Figure 2.19. Integrating Eq.2.37 , with the boundary conditions, $E = 0$ both in $-x_p$ and x_n, we can obtain the electric field. The electric field $E(x)$ in the depletion region is then:

$$E(x) = \frac{dV}{dx} = \begin{cases} \frac{eN_A}{\epsilon}(x + x_p) & -x_p < x < 0 \\ -\frac{eN_D}{\epsilon}(x - x_n) & 0 < x < x_n \end{cases} \tag{2.38}$$

Another integration then yield to the potential $V(x)$:

$$V(x) = \begin{cases} \frac{eN_A}{\epsilon}(\frac{x^2}{2} + x_p x) + c & -x_p < x < 0 \\ -\frac{eN_D}{\epsilon}(\frac{x^2}{2} - x_n x) + c & 0 < x < x_n \end{cases} \tag{2.39}$$

where the constant c is the same because at $x = 0$ the two equations must join. From boundary conditions $x = -x_p,\ V(x) = 0$ and $x = x_n,\ V(x) = V$, we can find the voltage V, then using the two relations:

$$V = \frac{e}{2\epsilon}(N_D x_n^2 + N_A x_p^2) \tag{2.40}$$

$$N_A x_p = N_D x_n \tag{2.41}$$

, where the second one arises from the conservation of the total charge, we can find the width of the depletion region:

$$w = x_p + x_n = \sqrt{\frac{2\epsilon}{e}\frac{N_A + N_D}{N_A N_D}V} \tag{2.42}$$

For a typical case in which one side of the junction is doped much more than the other (at least an order of magnitude), e.g. $N_A >> N_D$, the previous relation is reduced to:

$$w \simeq x_n \simeq \sqrt{\frac{2\epsilon V}{eN_D}} = \sqrt{2\epsilon V \rho \mu_e} \tag{2.43}$$

where Eq.2.36 has been used in the last equality. Then, as an aside, for a much more doped p side, the depletion region is almost all in the n side. The macroscopic properties of a highly asymmetric junction, such as resistivity and mobility, are dominated by the doping concentration of the lighter-doped side.

When an external voltage is applied, $\pm V_{bias}$, it increases or decreases, depending on the polarity, the potential barrier at the junction. As a result of the external voltage the depletion width decreases or increases. Silicon detectors are operated in reverse bias mode (the forward case will not be considered); this means that the bias voltage applied to the n side is higher compared to the p side. Then the potential barrier is higher and the widens of the depletion region increases, as can be understood from Eq.2.43, with a total voltage of:

$$V = V_{bias} + V_{bi} \tag{2.44}$$

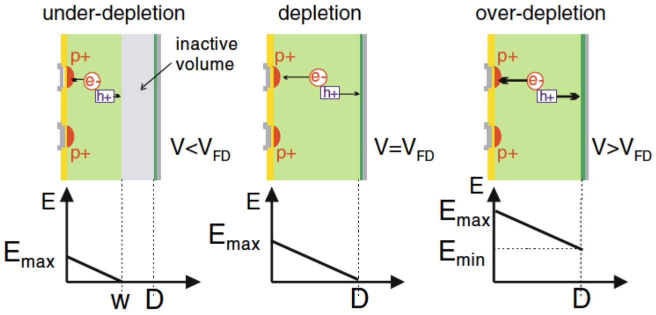

Figure 2.20: Sketch of electric field and depletion region for different values of the bias voltage; smaller, equal or greater than V_{FD} [8].

Charge created in the depletion region can be collected, while charge created in the non-depleted zone recombines with free majority carriers and is lost; the depletion region is then the active area of the detector. So to have a fully depleted detector, of thickness d, the voltage V_{FD} that has to be applied is:

$$V_{FD} = \frac{d^2}{2\epsilon\mu\rho} \tag{2.45}$$

For a bias voltage higher than V_{FD}, the overbias $V_{bias} - V_{FD}$ is translated into adding an offset electric field equal to $V_{overvoltage}/d$ (see Fig. 2.20).

To determine V_{FD} the characteristic curve of capacitance C versus voltage V or $1/C^2$ versus V can be used. Indeed the capacitance of the detector is:

$$C = \frac{A\epsilon}{w} = \begin{cases} A\sqrt{\frac{\epsilon}{2V\rho\mu}} & V_{bias} < V_{FD} \\ A\frac{\epsilon}{d} = const & V_{bias} > V_{FD} \end{cases} \tag{2.46}$$

with A area of the detector. For a 300 μm detector thickness and and a 1 mm^2 detector area, the capacitance is $C \sim 300\ fF$ (in silicon $\epsilon \sim 1pF/cm$).

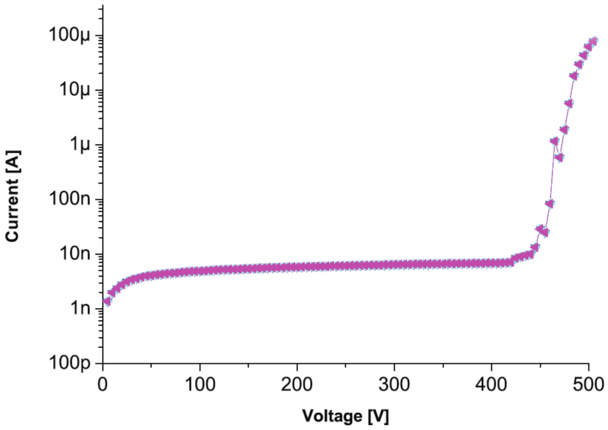

Figure 2.21: The current vs voltage characteristic for a silicon diode in the reverse bias direction. [8]

If the bias voltage increases beyond a critical level, an electrical breakdown is observed and the current increase dramatically due to the Zener or avalanche process. A too high current can cause a damage of the detector. In Figure 2.21 a typical $I - V$ curve is reported.

2.6.1.4 *PIN* diode

To have a large depletion region is then necessary to apply a higher reverse voltage (see Eq. 2.43); to avoid excessive voltage, a particular detector configuration is used. This configuration has a structure $p-i-n$ (PIN), where *i* stands for intrinsic semiconductor. In this way we can have a depletion region wide at will; moreover using an intrinsic or lightly doped region (called π if p type, ν if n type), the contact region between doped and lightly doped structure remains a contact that follows Ohm's law. The residual charge is almost zero in *i* region and then, from Eq. 2.37, the electric field across is almost constant (or slowly increasing/decreasing if π or ν); this feature can be very useful in some applications, considering that a uniform electric field and then a uniform velocity can be crucial for timing measurements, see Section 1.5.2.

2.6.1.5 Details on silicon detector structure

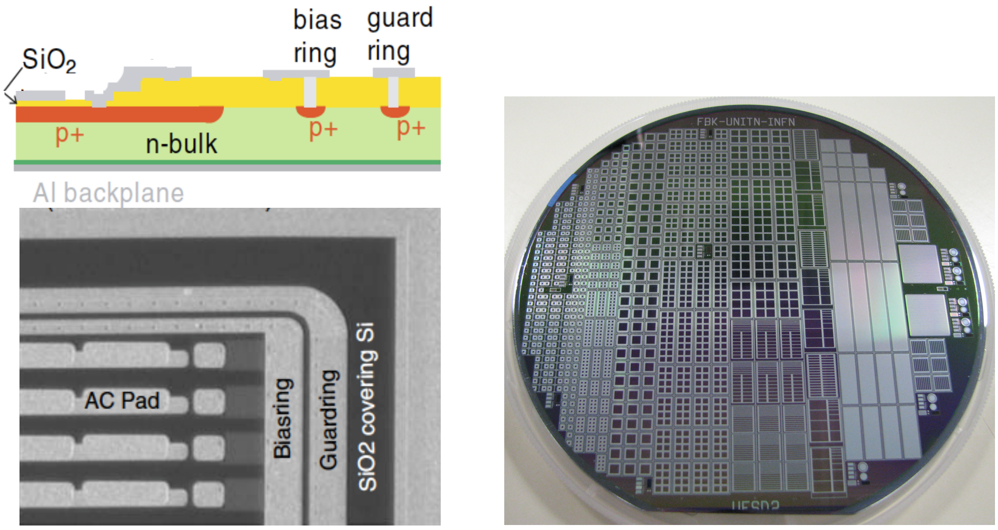

(a) (b)

Figure 2.22: A schematic representation and a photograph of a silicon detector (a); an FBK (Fondazione Bruno Kessler) silicon matrix (b).

At this point we should spend some words on some general structural details of a silicon detector.

A fundamental component for a silicon detector is the SiO_2; this is a really pure and stable material and indeed is one of the basic component for the detector. It is used to insulate the silicon. Indeed silicon, by its nature, tends to oxidise very easily, if exposed to oxygen (*native oxide*); to avoid this process the surface is usually covered (passivated) with technological oxide. This process also avoids the uncontrolled formation of surface defects (due to native oxide) and the propagation of oxidation to the first underlying atomic

layers. This material can be used also in AC coupling; inserted between the silicon and the Aluminium (the pick up electrodes), with this capacitor coupling, it reduces the leakage current, i.e. the current flowing in the reverse bias condition.
As we discussed in previous sections it is necessary to apply a bias voltage; to do it a bias ring (and backplane) is usually used: a ring all around the active area that ensures an homogeneous voltage even for several pixels.
A silicon detector can be segmented in severals substructure called pixels to optimise the spatial resolution. To shape the field inside each pixel and protecting it from edge effects, a guard ring is necessary; this can be both a single one, or several floating rings, which slowly go to ground. A schematic representation and a photograph of a silicon detector is reported in Fig.2.22(a).
Some problems can be caused from cracks along the edge due to cuts that reduce a silicon matrix to several silicon sensors; in Fig.2.22(b) a typical silicon matrix before the cutting is shown. A crack can induce a change in the behaviour near the edges, with a surface leakage current introduced due to a higher electric field, which can be compensated by adding some doping implantation.

2.6.1.6 Photon detection

When photons pass through silicon the intensity at a certain distance follows Eq. 1.12; in particular, the absorption length, the inverse of the absorption coefficient α, is proportional to the wavelength of light, see Figure 2.23.

Silicon detectors are sensitive to wavelengths between $\sim 150 - 1100\ nm$; the reason arises in the mechanism of interaction. If the energy of the photon is below of the energy bandgap, $1.12\ eV$, the photon can be absorbed only from free electrons. When the energy is larger than the bandgap, but still lower then $3.6\ eV$, the creation of $e^- - h$ pair requires a phonon of high momentum; the occurrence is small and then the absorption probability is low. For higher energy photons, lower phonon energy is required, and then the probability increases. For $E > 3.6\ eV$ a direct transition is possible, and the absorption is more probable; this corresponds to a wavelenght of $344\ nm$. Then for large λ, the absorption is limited and a photon can penetrate in the whole thickness without absorption; on the other side, for too small λ, the photon is almost immediately absorbed but the lifetime of the carriers is small and then the detector is not sensitive.

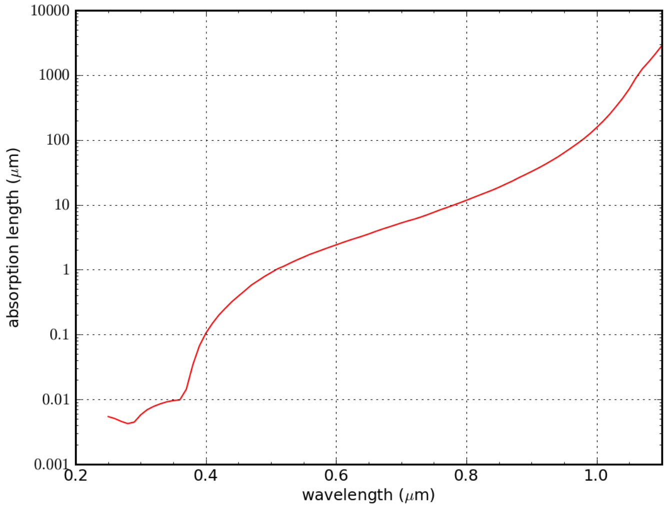

Figure 2.23: Photon absorption length in silicon versus wavelength.

2.6.1.7 Timing considerations

A fast (high slew rate) and large signal to noise ratio are the key, as already said, to improve the time resolution.

This may suggest a thicker detector, to improve the signal but as we will see, the maximum current is independent from that. Indeed, from Ramo's theorem, Eq.1.32, 1.34, and Eq.1.7, the maximum current in a silicon detector is:

$$I_{max} \propto nqv_{sat}\frac{1}{d} = Nd\ qv_{sat}\frac{1}{d} = Nqv_{sat} \tag{2.47}$$

where $N = n/d$ is the number of pairs per μm. Then, the maximum current is independent from the thickness and it is always the same; in particular, for $N \sim 10^2\ \mu m^{-1}$, $q = 1.6 \cdot 10^{-19}\ C$ and $v_{sat} = 10^7\ cm/s$, the value corresponds to $1 - 2\ \mu A$.

On the other hand, to have a fast detector one should increase the velocity of charges inside the semiconductor; however the maximum achievable velocity is limited by saturation (v_{sat}). So it is important to keep the electric field above a certain threshold which causes the saturated velocity; this corresponds to an electric filed of $E \sim 20\ kV/cm$. This should also be as uniform as possible, and to get it we can use a $p - i - n$ configuration (see Section 2.6.1.4), to have a uniform charge collection. Anyway, standard silicon detectors, have a limited time resolution; to improve it, we need another technique. Taking inspiration from gaseous detectors, the avalanche process could be the way.

2.6.2 Avalanche process

As previously said, at high applied bias the velocity saturates; at even larger voltage, the impact ionisation (or rather, the avalanche process) takes place. If kept under control below a certain threshold or stopped after a while, the avalanche is not dangerous for the detector and rather can be an improvement in a detector (see below e.g. UFSD, SiPM) for characteristics like the time resolution.
The process is totally similar to the Townsend avalanche, see Section 2.3.1.2, with a definition of gain G; indeed the impact ionisation model in silicon is based on it. The gas ionisation process is replaced by the impact ionisation in silicon, which means that the primary electron (or hole) takes enough energy to excite an electron in the conduction band, creating secondary $e^- - h$ pairs.
This process can then be parametrised with the same equation (Eq.2.12) used for gas. Of course the value of the variables here are different.
In silicon both electron and holes can start an avalanche; modelling the impact ionisation process [47,48] passes through the description of its generation rate U_{av}, which is the number of e-h pairs produced in silicon per cm^3 per unit time:

$$U_{av} = \frac{dn}{dt} = \frac{dp}{dt} = \alpha_n n v_n + \alpha_p p v_p \tag{2.48}$$

, with $v_{n,p}$ the carrier velocity of electron and holes respectively and $\alpha_{n,p}$ (cm^{-1}) represent the electron/hole ionisation coefficients; there is an empirical relation for the $\alpha_{n,p}$ related to the electric field E, following the Chynoweth empirical law:

$$\alpha_{n,p} = \alpha_{n,p,\infty}\ e^{-\frac{\beta_{n,p}}{|E|}} \tag{2.49}$$

where $\alpha_{n,p,\infty}$ and $\beta_{n,p}$ are constants of different values for electrons and holes.

In Figure 2.24 the impact ionisation coefficient $\alpha_{n,p}$ versus $1/E$ is reported. At $E \sim 300\ kV/cm$ the electron has enough energy to initiate substantial charge multiplication of 1 $pair/\mu m$ and the corresponding gain $G = e^{\alpha d} < 10$ (see Eq.2.12), for a thickness of high electric field of $d \sim 1 - 2\ \mu m$; this is a linear mode device. For higher $E \sim 400\ kV/cm$, also the holes start to ionise, with a multiplication of $\sim 1\ pair/\mu m$ (electrons $\sim 4\ pair/\mu m$). Here the mode is still linear and the gain is now $G \sim 50 - 300$. For even higher electric field ($> 400 - 500\ kV/cm$), both electrons and holes ionise

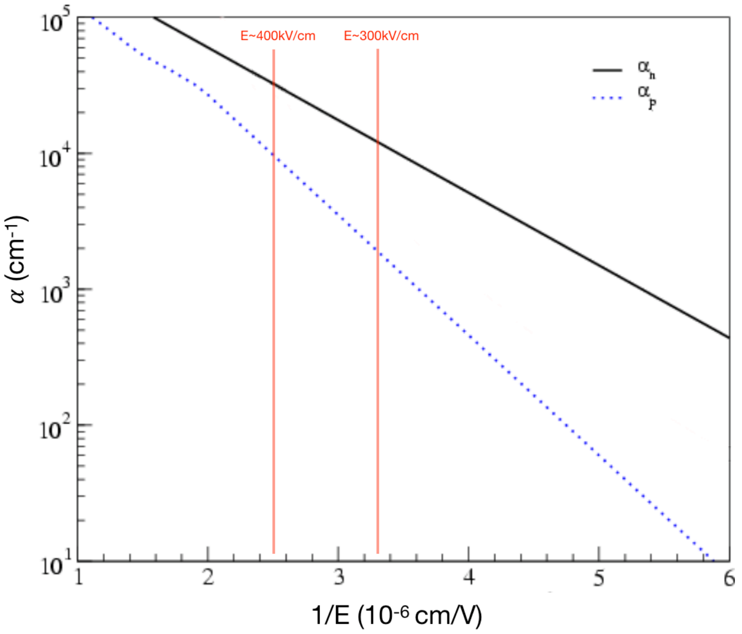

Figure 2.24: Impact ionisation coefficient for electrons (α_n) and holes (α_p) versus $1/E$; the red lines indicate two critical values of electric field E.

and the detector is in breakdown; we have a Geiger mode detector, in which the gain can tend to infinite.

2.6.3 APD

In '60s -'70s, R. J. McIntyre and P. P. Webb brought fundamental contributions to the understanding of the avalanche process in silicon and its statistical properties, with the Avalanche PhotoDiodes (APD).
This idea was born from the need to reveal even few photons; indeed a photon in silicon, creates just one pair $e^- - h$, so to detect it an internal multiplication is necessary. Typical value of gain is between $\sim 50 - 500$. The electric field needed for this is achieved by means of both the external voltage and a special gain layer added in the $p-i-n$ structure, so that we have a non uniform doping. This gain layer is the particularity of silicon detectors with gain.

Figure 2.25 shows the design of an $n - in - p$ detector with the added gain layer p near n^+, so that the structure is $n^+/p/\pi/p^+$; the electric field associated is reported in the same figure (right). As you can see, it is con-

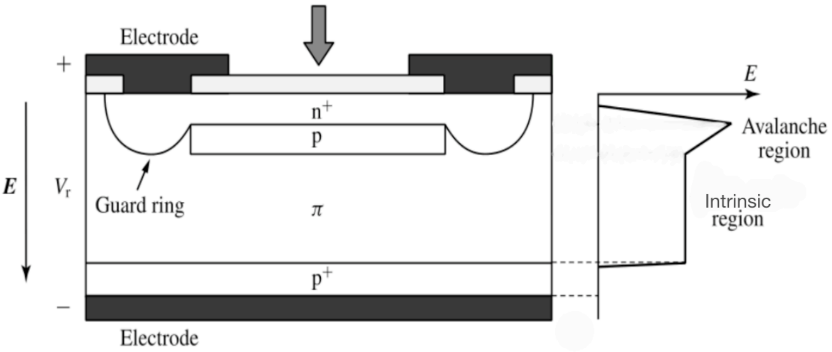

Figure 2.25: Lateral view of $n - in - p$ detector structure with the added gain layer p.

stant in the intrinsic region while has a huge step in correspondence of the junction $n^+ - p$. This high field region, usually a few μm deep, is where the multiplication happens.

The time resolution in this kind of detectors is excellent, typically 30 ps, because the gain improves directly both the slew rate and the signal amplitude and consequently the time resolution. This can be understood considering the number of $e^- - h$ pair created per time interval dt; the number of electrons per dt is given by $Nv_{sat}dt$, with N number of pairs per unit lenght (μm). Then the multiplication process takes place, with gain G so that $dn_{gain} \propto GNv_{sat}dt \propto Gdt$. The current induced in dt due to gain is then (using Eq.1.32-1.34):

$$\frac{di_{gain}}{dt} \propto \frac{G}{d} \tag{2.50}$$

with $\frac{di_{gain}}{dt} \sim \frac{dV}{dt}$.

Unfortunately APDs have some drawbacks: they have a long dead time and they can not detect single photons.

Two solutions can be identified; one more focused on detecting directly charged particles and one focused on detecting indirectly charged particles by photons.

The first one can be based on lower gain; here the dead time would be lower and moreover it can be easier segmentable (lower field); the problems or rather the key parameters here are the doping concentration and the radiation hardness (which in environments like the LHC it can be a fundamental parameter).

The second one can be based on higher gain, over breakdown; in this way we can detect charged particles by, for example, a scintillator plus silicon detector. The advantage is that the scintillator is a really common, cheap (organic plastic scintillator), manageable and known detector, with good properties of radiation hardness and dead time. The problem is that the silicon detector coupled to it has to be able to detect even single photons and then the gain has to be really high, over breakdown, and therefore the noise increases.

In this thesis both kind of detectors are treated; Ultra Fast Silicon Detector (UFSD), low-gain based, and Silicon PhotoMultiplier (SiPM), high-gain based.

2.7 Silicon PhotoMultiplier

Silicon PhotoMultiplier (SiPM) (or MPPC[18]) is a silicon detector optimised for photon detection; it consists of a matrix of pixels, Single Photon Avalanche Detector (SPAD), joined together on a common silicon substrate and decoupled from each other by resistors [49–57]. Each pixel works like a Geiger counter, which means that it can detect just the passage of one particle (photon), without any further information, like the number of incident photons per cell. So, individually, a SPAD is a binary detector. Putting in parallel many pixels, $10-10000\ pixels/mm^2$, is then possible to retrieve information about the number of incident photons. The whole SiPM is then an analogic detector, with the output A given by the sum of each pixel contribution A_i:

$$A = \sum_i A_i \tag{2.51}$$

The dynamic range of a SiPM, for a total number of pixel N_{tot}, and $N_{photons}$ incident photons, is:

$$A \sim N_{fired} = N_{tot}\big(1 - e^{\frac{-N_{photons}PDE}{N_{tot}}}\big) \tag{2.52}$$

with PDE the Photon Detection Efficiency. This is true for $N_{photons}PDE << N_{tot}$; otherwise, the signal is saturated and the dynamic range is limited.

Each SPAD is then an APD where the voltage V_{bias} is kept $(10-20)\%$ over the breakdown voltage, V_{BR}; in this way the gain can go up to 10^6 and it is then possible to detect even a single photon. Thanks to the high doping, the V_{bias} can be much smaller than for example UFSD, about 30 V or 70 V depending on the structure characteristics. In Figure 2.26 an example of carrier concentration and electric field profile versus thickness is reported.

---

[18] Multi Pixel Photon Counter

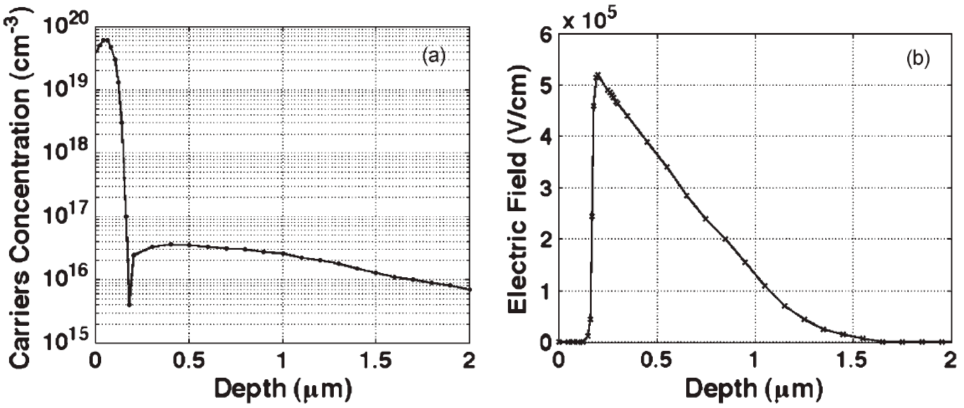

Figure 2.26: SiPM typical carrier concentration (left) and electric field (right) profiles versus detector depth. [56]

When a photon passes through the cell it may create an $e^- - h$ pair; both electron and hole can start an avalanche breakdown, creating the signal output; the result is a breakdown avalanche, with a constant current flow through the junction. To make possible the detection of subsequent photons, the cell must be reset (the process is smilar to the PPC for gaseous detector), or rather the avalanche has to be quenched. For this, each pixel is connected to a quenching resistor, R_Q.

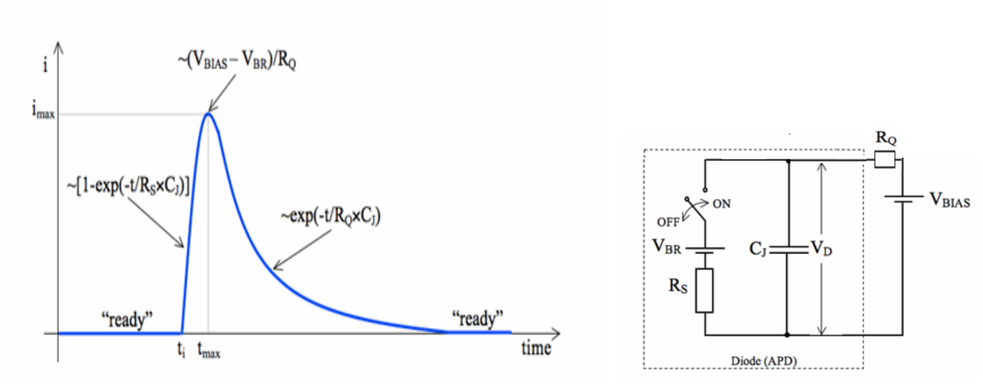

(a) (b)

Figure 2.27: Depicted signal of a single pixel (SPAD) of SiPM (a); a scheme of a pixel-SiPM circuit (b) [57].

In Figure 2.27(b) a scheme of the circuit is shown. When a particle passes through the cell, the junction capacitance, $C_j \sim 0.1\ pF$ starts to discharge

through R_s; the resistance of the detector, typically $R_s \sim 1\ k\Omega$, depends on the structure of the SiPM. The time constant leading this process is given by $\tau_r = R_s C_j \sim 100\ ps$. As the current increases, the Voltage drop on R_q increases whereas the voltage on the cell itself decreases. In this way, the impact ionisation probability falls down and the avalanche is quenched. The signal then reachs a peak $(V_{bias} - V_{BR})/R_Q$ in a typical fast pulse of 1 ns; it is then directly proportional to overvoltage $(V_{bias} - V_{BR})$. After that, the signal starts to decrease and in this time range, the cell is off and cannot detect any further photon. During the fall time the voltage on C_j increases until the voltage is totally restored and the cell is switched on again. The time constant of the falling edge is $\tau_f = R_Q C_j$.
In Figure 2.27(a) a typicall single pixel signal of a SiPM is reported.
In general, we would like to have a big signal and both rising and falling edge as fast as possible, for time resolution and dead time reasons, respectively. For the rise time, the capacitance and the resistance of the detector should be as small as possible, but of course they depend on the structure of the detectors, so many other variables are involved. The quenching resistor is a parameter that instead can be chosen independently but is still a trade off between several effects[19]. A typical value is $R_Q = 150\ k\Omega$ and then the fall time is typically 100 ns , with a time constant $\tau_f = 15\ ns$.

In Figure 2.28(a) a typical internal structure of a SiPM is depicted. What

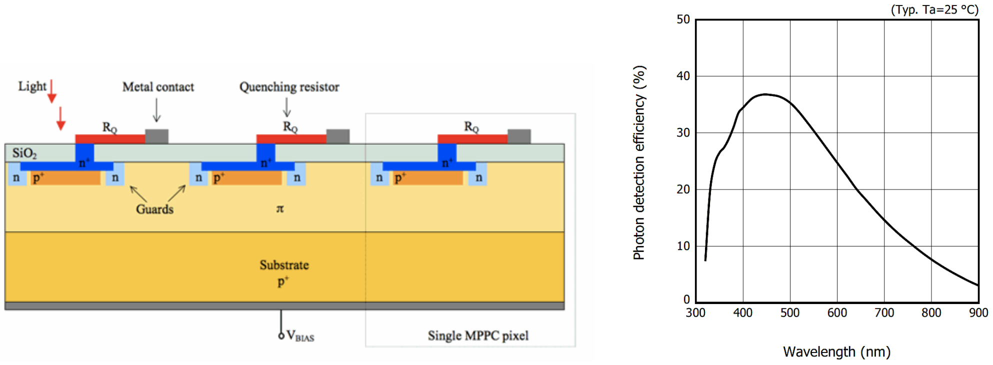

(a) (b)

Figure 2.28: Typical internal structure of a SiPM (a); PDE versus wavelength of MPPC-050P (b) [57].

---

[19] The quenching resistor R_Q has to quench the avalanche in a certain time, which would follow to big value of R_Q, but it should be as small as possible, to get a faster trailing edge.

is missing in this representation is the deep optical trench which should surround each pixel (SPAD); filled with oxide and metal it is necessary to reduce the crosstalk between cells.
The crosstalk is due to the photons created in the avalanche that can induce a fake signal in the adjacent cell; indeed in an avalanche breakdown, about $\sim 3\ \gamma/10^5$ carriers are produced; especially critical are the photons in the $850 - 1100\ nm$ wavelenght range.

In SiPMs it is of particular importance the antireflective coating, in absence of which the efficiency of the detector would be largely reduced. Indeed, when a photon passes in a different material, with greater refraction index, the photon can be reflected and then lost. The problem is in both surface, air/scintillator-SiO_2 ($n_{SiO_2} \sim 1.46$) and SiO_2-silicon ($n_{silicon} \sim 3.5$) interfaces. Adding silicon nitride improves the efficiency.
Typical values of layers thikness are: $\sim 0.16\ \mu m$ for the $SiO_2 + Si_3N_4$ layers; $\sim 0.1 - 1.5\ \mu m$ for n^+ electrode; p gain layer $\sim 1 - 3\ \mu m$; π layer $\sim 1\ \mu m$; and for the substrate p the thickness can change a lot for mechanical and handling reasons. As you can notice, the larger difference is in the π region (w.r.t. UFSD); in a SiPM this region has to be dramatically reduced for noise reasons (dark counts), which is in first approximation proportional to the volume.
In Geiger operation mode indeed the signal from a single thermally generated pair is indistinguishable from a single photon signal. The rate is $Rate_{DC} > 100\ kHz/mm^2$ at $25°C$. This dark current is the main source of noise in the detector. It is directly proportional to the gain G: $I \sim e\ G\ Rate_{DC}$. For a threshold of about 4 photons impinging the detector (i.e. 4 pixels of the SiPM switched on by photon signals) it is largely reduced ($Rate_{DC} \sim 1\ kHz$). Moreover, it decreases by a factor of 2 for a decrease of 8 degrees in temperature.

The SiPM depicted in Figure 2.28(a) is an $n - in - p$ structure, more sensitive to green light ($\sim 550\ nm$), but $p - in - n$ structures can be also useful for SiPM, more sensitive to blue light, depending on which photon radiation has to be detected. Indeed, a blue photon, $\sim 450\ nm$, and a red one, $\sim 700\ nm$, have energies of $\sim 2.8\ eV$ and $\sim 1.8\ eV$, respectively. Then a blue photon, looking at Figure 2.23, probably slewing $0.5\ \mu m$ before being absorbed. Then the pair is produced in the n^+ layer, near the junction. The average path of a red photon is on the contrary bigger, $\sim 2 - 3\ \mu m$, and is then usually absorbed in the π *region*. In Figure 2.28(b) the efficiency (PDE) versus the wavelength for an $n - in - p$ SiPM from Hamamatsu is reported.

The Photon Detection Efficiency (PDE) of a SiPM can reach 40%. It can be expressed as:

$$PDE = QE \; \epsilon_{BD} \; \epsilon_g \tag{2.53}$$

where the Quantum Efficiency QE corresponds to the number of $e^- - h$ pairs created per incident photon in the depletion region. ϵ_{BD} is the breakdown probability which depends on the electric field and on the carrier type ($\epsilon_{BD,electron} > \epsilon_{BD,hole}$ because of a larger ionisation coefficient); $\epsilon_g = \frac{sensitive\ area}{total\ area}$ is the geometrical efficiency, the fill factor; it's for example reduced by the quenching resistor on the top of the pixel or by different (smaller) number of pixels used (in this way the dead area in between the pixels is reduced). Moreover, the efficiency is related also to the recovery time of a cell, that as said is about 100 ns.

In a SiPM most of the timing fluctuations arise from statistical fluctuations in the current growth, because, due to the thickness and the gain, the signal is fast and big (even if the noise has to be kept under control). For a single cell, current fluctuations depend on the photo-conversion depth (negligible), the lateral propagation and vertical build up of the avalanche.
The lateral propagation, see Figure 2.29(a), is due to both the diffusion of carriers in parallel to the growth of avalanche and to the photon creation, the same responsible of crosstalk, that can trigger the breakdown also inside the same pixel (this time more critical for smaller wavelength, < 800 nm).
The vertical build up, see Figure 2.29(b) is the fluctuation on the avalanche growth; it can be noticed that is totally similar to the avalanche fluctuations for the RPCs, Figure 2.12(a). The current of a single photogeneration is $\sim 2 \cdot 10^{-5}$ mA; as long as the number of carriers stay under 100, which corresponds to $\sim 2 \cdot 10^{-3}$ mA, the fluctuations are more stochastic (Landau fluctuations) and cause significant noise on the current. As the number of carriers increases, the process becomes more deterministic and the fluctuations are negligible. Notice that (arrow in the Figure), the carrier may fail to produce an impact ionisation.

The time jitter resolution of a single cell (photon) σ_i can be expressed using the Eq.1.41. When n photons are detected, the total output signal of the SiPM is n times the single photon signal and then the slew rate is $n{\cdot}dV/dt$; the total noise fluctuations is instead a quadratical sum of the single ones so that the total noise factor will be $\sqrt{n}$ the single one fluctuation. Then, for the whole SiPM, with n pixels hit, the time resolution is:

$$\sigma_n \sim \frac{\sigma_i}{\sqrt{n}} \tag{2.54}$$

So the time resolution improves with the number of pixels hit by a photon.

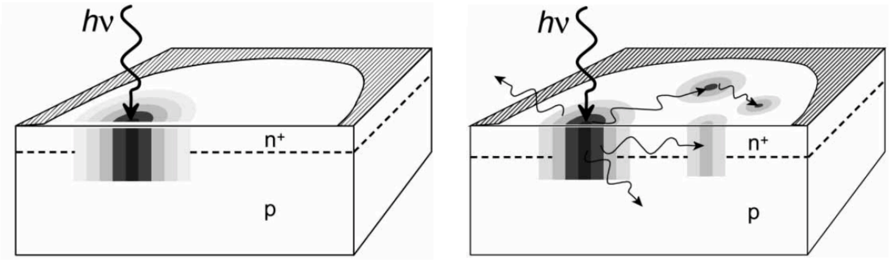

(a)

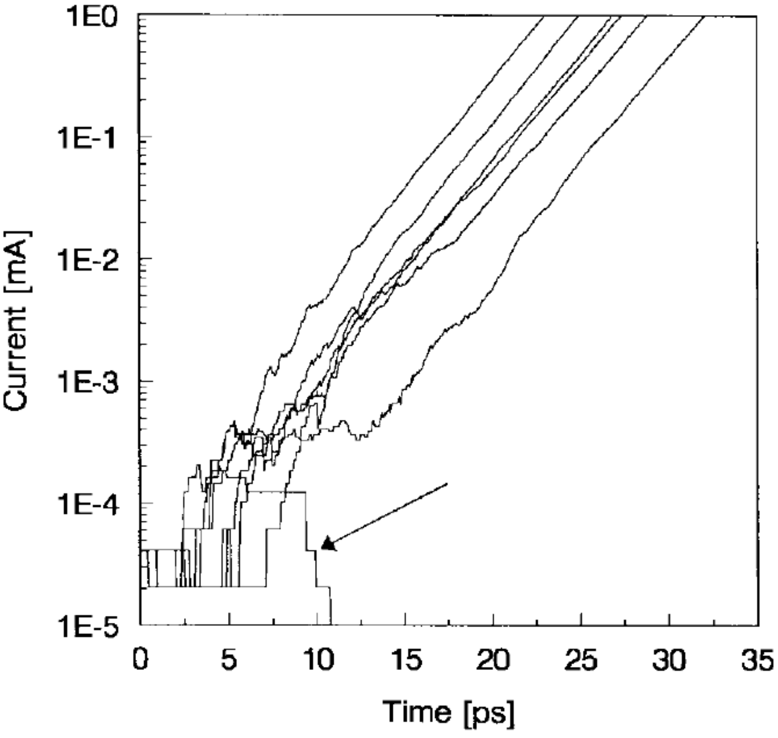

(b)

Figure 2.29: Lateral propagation of avalanche: diffusion of carriers in parallel to the growth of avalanche and to the photon creation (a) [51]; Avalanche vertical build up, the arrow indicates a failed impact ionisation by carriers (b) [49].

2.8 Ultra Fast Silicon Detector

The Ultra Fast Silicon Detector (UFSD) is a new kind of silicon detector, based on Low Gain Avalanche Detector (LGAD) technique, proposed and developed by CNM[20], presented the first time in 2014. UFSDs [16, 58–61] are optimised for time measurements, and the goal is to reach both excellent space and time resolution, combining the excellent space resolution of standard silicon detectors ($\sim 10\ \mu m$) and time resolution of APD (order of $10\ ps$). One of the challenges of the UFSD technology is to achieve the radiation-hardness, since they are designed for working in high-fluence environments (up to $5 \cdot 10^{15}\ n_{eq}/cm^2$).

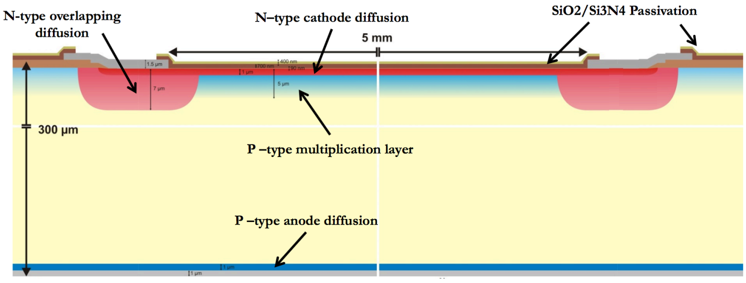

Figure 2.30: Example of the internal structure of a 300 μm thickness CNM-LGAD prototype.

Figure 2.30 shows a cross-section of the internal structure of a CNM-LGAD prototype, of $5 \times 5\ mm^2$ area and 300 μm thickness. The structure is totally similar to a single cell of the SiPM structure, without the addition of the quench resistor present in the SiPM. The main difference on the structure, arises in the thickness of the various layers. From the top, a double layer (yellow and dark brown) of silicon nitride, Si_3N_4, and dioxide, SiO_2, as antireflective and insulator coating, is visible. In red, the highly doped electrode n^+ of 1 μm thickness; the gain layer (usually Boron) p doped, 5 μm thick in blue; in yellow the π region of 300 μm; the p^+ layer of 1 μm. In figure the region named *N-type overlapping diffusion*, is more often called *guard ring*; it is needed to avoid breakdown associated with the small radius of curvature of shallow $n^+ - \pi$ junction. Moreover it also ensures a deeper junction under metal. Here the p^+ channels are not depicted; they help to stop the diffusion of electrons through adjacent diodes, and should surround the device, external to n-guard rings[21].

---

[20] Centro Nacional de Microelectronica, in Barcelona, Spain

[21] p^+ channels are necessary for a cut off, indeed they limit the lateral spreading of the depletion region, ensuring that is not extending over (channel inversion).

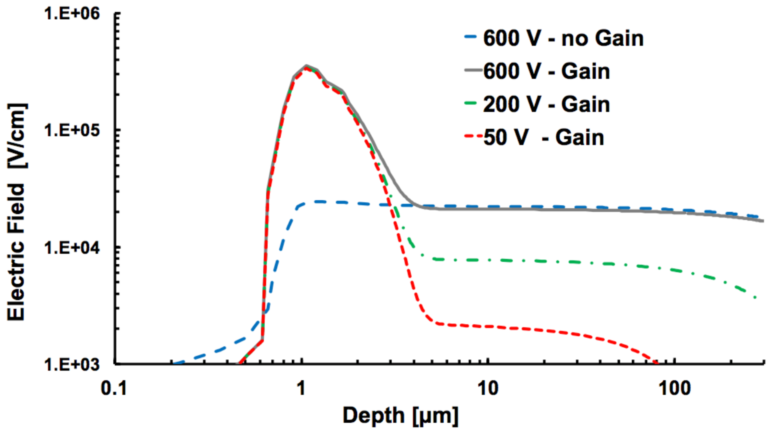

Figure 2.31: Electric field of a 300 μm thick LGAD at different bias voltages compared to a PiN (no gain) in logarithmic scale [16] .

Simulation and experimental results show that the optimised gain in UFSDs is about $10-20$; the corresponding electric field is $\sim 300\ kV/cm$. This was kept as low as possible, to permit good time resolution. The advantages of a lower gain are several: less noise, which is proportional to gain, absence of crosstalk between multiple pads in the same detector, easier segmentation, due to a lower electric field, and smaller dead time; the last one is due to the requirement of the absence of holes multiplication, which are slower. The detector is indeed kept below voltage breakdown, thanks to a precise doping concentration.

The concentration of the gain layer here is about $10^{16}\ cm^{-3}$ of Boron and it is the true key parameter for UFSD, which has to be under control within a few percent. In Figure 2.31, the electric field profile versus depth for a 300 μm detector, for different values of the external bias voltage is reported, zoomed in the high field region. The doping concentration here is quite smaller than for the SiPM (see Section 2.7), because here it is not needed such a high gain; the drawback is the higher voltage needed ($\sim$ 10 times bigger).

As explained for the APD, the field profile is divided in two regions; one, where the field is almost constant (decreases only slightly) in the whole detector, or rather the depletion region (we have a fully depleted detector); here the electric field is lower but is kept bigger than $\sim 30\ kV/cm$, to saturate the velocity. The other, in correspondence of the high field region, a few μm thick, of about $300 \sim kV/cm$. To reach this value, a voltage bias of

200 – 400 V is needed.

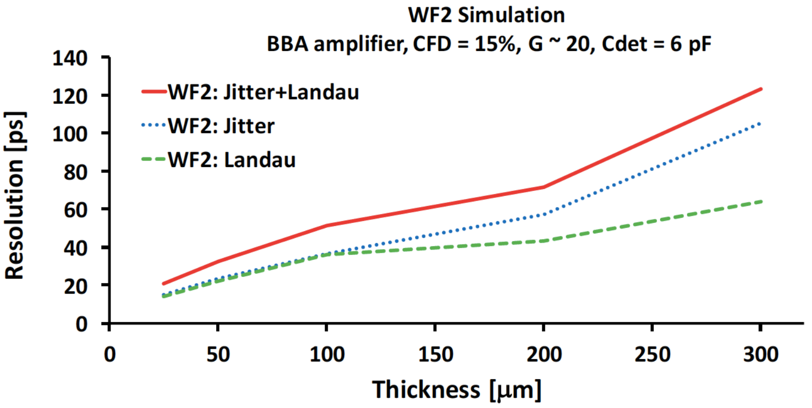

Figure 2.32: Simulation plot realised with Weightfield2 (WF2) [62]: time resolution as a function of the detector thickness [16].

Another fundamental parameter is the thickness of the detector; indeed from Eq.2.50 the thickness is the other important variable. So for thinner detectors the time resolution improves, see Figure 2.32; in practice, if we want too keep a gain of 10 – 20, it can not be too thin, otherwise the capacitance would be too big and consequently the signal too low to be readable from the readout electronics. The optimised value from simulation is 50 μm. With all these detector characteristics the time resolution expected from simulation for 50 μm thickness, was $\sim$ 30 ps; in a beam test in 2016 this result was actually obtained, see [63], in particular getting 34 ps at 200 V.

The noise contribution of these detectors is still under study; in Figure 2.33(a) a plot concerning simulations on jitter and Landau noise (i.e. current fluctuations) is reported (see Sections 1.5.2, 1.5.3 and 1.5.4). Figure 2.33(b) is more focused on Landau noise, for different thickness. Both plots are studied in function of the CFD; they are in agreement with the considerations reported in 1.5.5. As expected, the jitter (and time slewing) are larger for smaller slew rates, which means at the beginning and at the end of the signal, and for higher gain. About Landau fluctuations, there is not an analytic expression; however they are minimised using a lower threshold and for thinner detectors. On the contrary they seem independent of the gain;

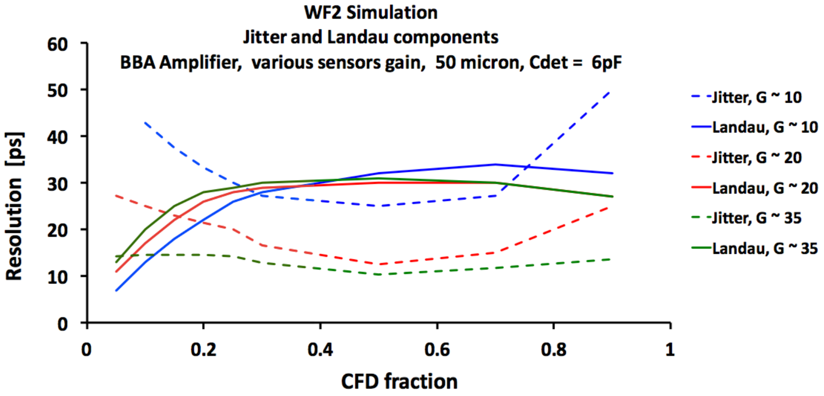

(a)

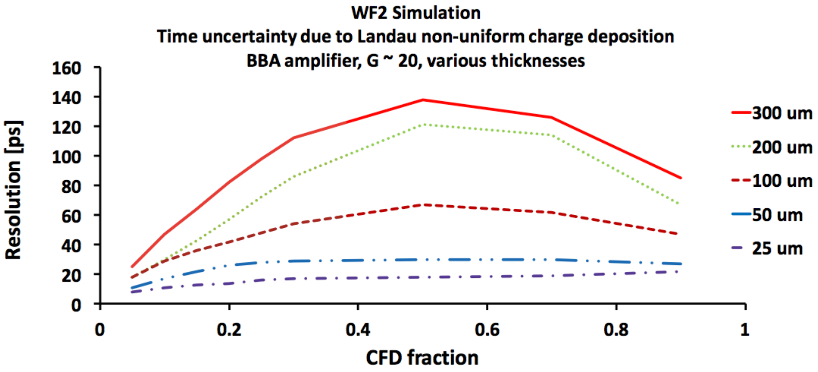

(b)

Figure 2.33: Simulation plots: jitter and Landau noise for a 50 μm detector with a BBA amplifier versus the threshold applied to a CFD (Constant Fraction Discriminator) for various gains (a) and Landau noise versus CFD for several detector thicknesses (b) [16].

this can be explained by the study of gain fluctuations, see Figures 2.12(a) and 2.29(b); indeed beyond a certain number of carriers the process seems to be more deterministic.

Chapter 3

MRPC

In this chapter, the results obtained both on existing and fully operational MRPCs, the ALICE-TOF MRPCs, and the results obtained on new chambers (built to improve the already excellent performances of standard MRPCs) are reported.
In the first part of the chapter the results of an analysis dedicated to the understanding of effects that can affect the time resolution of the ALICE-TOF MRPCs has been performed. Beside the aim of improving offline the TOF time resolution, it provides also important informations that can be included in the Monte Carlo simulation of the detector. The first part of the chapter is then dedicated to the description of this analysis and the obtained results. The second part of the chapter is dedicated to the description of two *R&Ds* on MRPCs. These detectors have been designed, built and tested to improve the MRPCs performances on timing and rate capability, yet maintaining some fundamental features, for future applications in high-luminosity colliders.

3.1 Signals clusterization in the ALICE-TOF system

In this section a study to optimise the already excellent performances of the ALICE TOF system is covered. The analysis performed to determine, and possibly correct for, some factors that can lead to a spoiling of the TOF time resolution are described. A particular attention on the cases where the signal is sensitive to the position of the avalanche induced in the detector strip has been given: in particular when only one of the MRPC pads has fired (single hit events) or when more than one pad (a cluster) is associated with the same track (multi hit events). Single hit events are affected by the time walk delays while in multi-hit events the signal is divided among different pads and should be carefully reconstructed. At the end of this section some considerations regarding the Monte Carlo simulations arising from this study are reported.

3.1.1 Single and multi-hit events in the ALICE TOF

The TOF MRPC strip (see Section 2.5.3) is segmented into two rows of 48 pickup pads of $3.5 \times 2.5\ cm^2$, for a total of 96 pads for each strip. When a particle impinges on a strip, in most of the cases (more than 80%) it induces a signal in only one pad (see Fig.2.16). In particular this pad is associated to a track according to a matching window (of 3 cm for $Pb - Pb$ collisions) around the extrapolation point (see Fig.2.5.2).
But what is the influence on timing of the impact position of the track on the pad?
With the x, z reference system defined as reported in Figure 2.16, the residual in x, Δx, or in z, Δz, can be defined as the distance of the interaction (TPC extrapolation) point from the centre of the pad. In Figure 2.16 the MRPC pad layout is visible. The point where the electrical signal is collected (pick up point) has a defined position; it is in the centre of the pad along x ($\Delta x = 0\ cm$) while along z it is positioned at the top, $\Delta z = +1.75\ cm$ (bottom, $\Delta z = -1.75\ cm$) of the pad for the top (bottom) row of the pad. As a consequence the TOF time measurement suffers a delay time due to the finite signal propagation time on the pad which is proportional to the distance of the interaction point from the pick up point. This delay time is called time walk.
From the point of view of time resolution it is then fundamental to understand if the time walk effect worsens the time resolution depending on the position of the interaction point on the pad.
Another effect which depends on the interaction point on the detector arises in the multi-hit events; these cases represent the 15% of the total events where more fired pads are associated to the same track (particle). This is related to the passage of the particle near the edge of a pad, so that the avalanche created in the detector induces a signal in more than one pad; all these pads form then a so called cluster.
For time measurement, until now, the TOF software considered only the matched pad (the one closest to the extrapolation point); the observed time resolution (65 ps) of these multi-hit cases is worse than the single hit case (57 ps), due to edge effects. A study to optimise the time resolution for multi-hit events has been performed, introducing a clusterization of the signals: the intuitive modus operandi consists in trying to get from a double

(worse) time measurement (t_1, and t_2), corresponding to two-pad hits, a single optimised time and a single position.

A study on both the time walk effect and the multi-hit events has been performed; the data used were collected in $Pb - Pb$ collisions at $\sqrt{s_{NN}} = 5.02\ TeV$ and for a selected particles momentum of $0.8 - 1.2\ GeV$ (to select a pure pion sample).

3.1.2 Time walk effect

As mentioned, the defined position of the signal pickup electrode on the pad and the finite propagation velocity of the signal on the pad, introduce a delay time on the TOF measurements, the time walk, proportional to the distance of the signal created from the pick up point.

In Figure 3.1(a) the dependences of the delay time from the residuals Δx and Δz are reported; the pick up point, at the expected values (looking at Fig.2.16) of $\Delta x = 0\ cm$, $\Delta z = -1.75\ cm$ [1] , can be easily recognised.
The distribution has been fitted using the following function:

$$F(\Delta x, \Delta z) = \frac{1}{v}\sqrt{p_0^2\ \Delta x^2 + p_1^2(1.75 \pm \Delta z)^2} + p_2 \tag{3.1}$$

where at the residual Δz a constant offset to take into account the different position of the pick up point was added. The constant $v = (2.39 \pm 0.29)10^8\ m/s$ represents the signal propagation velocity in the pad; the value obtained from an analysis performed in a beam-test [66] was used. The meaning of the parameters is the following: p_2 represents a simple offset; p_0 and p_1 are the degradation factors in the visibility of the effect due to the finite resolution in the extrapolation of the track; indeed the spatial resolution is of the order of $\sim 6 - 7\ mm$, in the selected momenta ($(0.8 - 1.2)\ GeV/c$).
In the beam test, $p_0 = p_1 = 1$; here values equal or less than 1 are expected (because of worst spatial resolution and maybe track inclination), indeed: $p_0 = 0.26 \pm 0.01$ and $p_1 = 0.20 \pm 0.01$. Then, because of a worst spatial resolution (due to the tracking resolution) and a worst alignment, the time walk effect in the actual set up is dramatically less visible than in the beam test, where the delay time (time walk) observed can reach a maximum of $\sim 140\ ps$; in the ALICE-TOF a maximum of $\sim 30\ ps$ can be observed.

---

[1] Since for the z axis there are two different positions of the pick up point, depending on the row, the bottom row has been arbitrary chosen (and so $\Delta z = -1.75\ cm$), consequently the other row has been symmetrized.

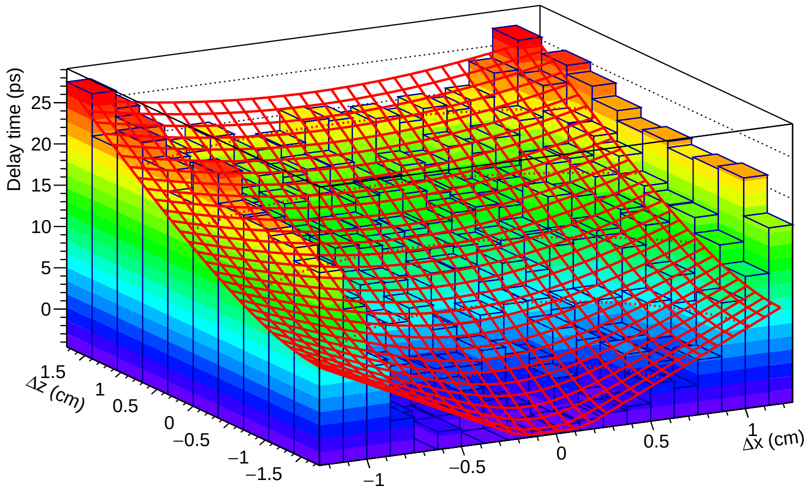

(a)

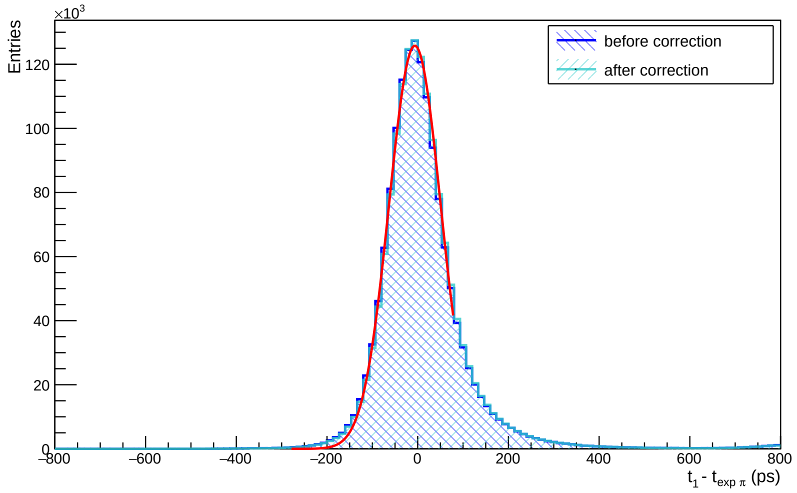

(b)

Figure 3.1: Distribution of the delay time (time walk) versus residuals Δx and Δz (a). Time distributions before and after time walk correction (b); they are almost superimposed indeed no significant improvement has been obtained. In the right part of the gaussians there are visible tails, probably of instrumental nature, which cause an asymmetric distribution.

The TOF time measurement $t - t_{exp\ \pi}$ (see Eq.2.32; the resolution of t_{ev} is 6 ps, totally negligible) has then be corrected for this residual correlation, i.e. for time walk. From the gaussian fit in Fig.3.1(b), a time distribution totally compatible with the original (uncorrected) one has been found; the distributions have a sigma of 57 ps, centred in -6 ps (see Figure 3.1(b)). This is due to the worst spatial resolution and worst alignment, if compared with the beam test setup, in which the time walk observed causes a measurable smearing in time resolution; then in that case, correcting for time walk permits to improve the time resolution of a $\sigma_{tw} = 44$ ps. With the the actual setup, a time walk correction seems instead to be totally negligible for the TOF time resolution.

3.1.3 Signals clusterization

With a better comprehension and optimisation of the single hit events, a study to optimise the TOF time resolution for multi-hit events introducing a signals clusterization has been performed. This study was focused on the double hit cases along the x axis (11%). The various analysis steps for the final optimisation are described in the following.

For a better understanding of the variables used in the analysis the number 1 (and relative observables) will indicate the matched pad, i.e. the one closest to the extrapolation point, and the other pad is the number 2.
First a cluster has to be defined; indeed signals in two nearby pads by themselves are not always due to a single track: indeed a mismatch can happen, i.e. in the LHC environment, the signals, even though associated with the same track, can come, for example, from two different nearby particles (tracks). To avoid any possible track mismatch, a time difference between the two measurements (see Fig.3.2(a)) in the interval of $|(t_1 - t_2)| \leq 150$ ps has been selected. This selection can be better understood looking at Figure 3.2(b) where the time difference versus the average time minus the $t_{exp\ \pi}$ is reported. The $(t_1 - t_2)$ distribution is expected to be Gaussian but it is indeed broadened from the indicated mismatch, due to t_1 or t_2; e.g. for a fixed t_1, t_2 spans over all the possible values, as depicted with the line t_2 mismatch. For a fixed t_2, the probability of mismatch when t_1 is the nearest seems to be suppressed (no t_1 mismatch distribution(line) in the bottom of the core).A selection of just the core of the distribution with the net majority of the events $(t_1 - t_2) \leq 150$ ps was done.
As an aside, in the same plot is also clear that the reason to select an interval of $((t_1 + t_2)/2 - t_{exp\ \pi}) \leq 800$ ps is to select only pions.

In Figure 3.3(a) the distributions of the residuals $\Delta x_1, \Delta x_2$ are shown. To

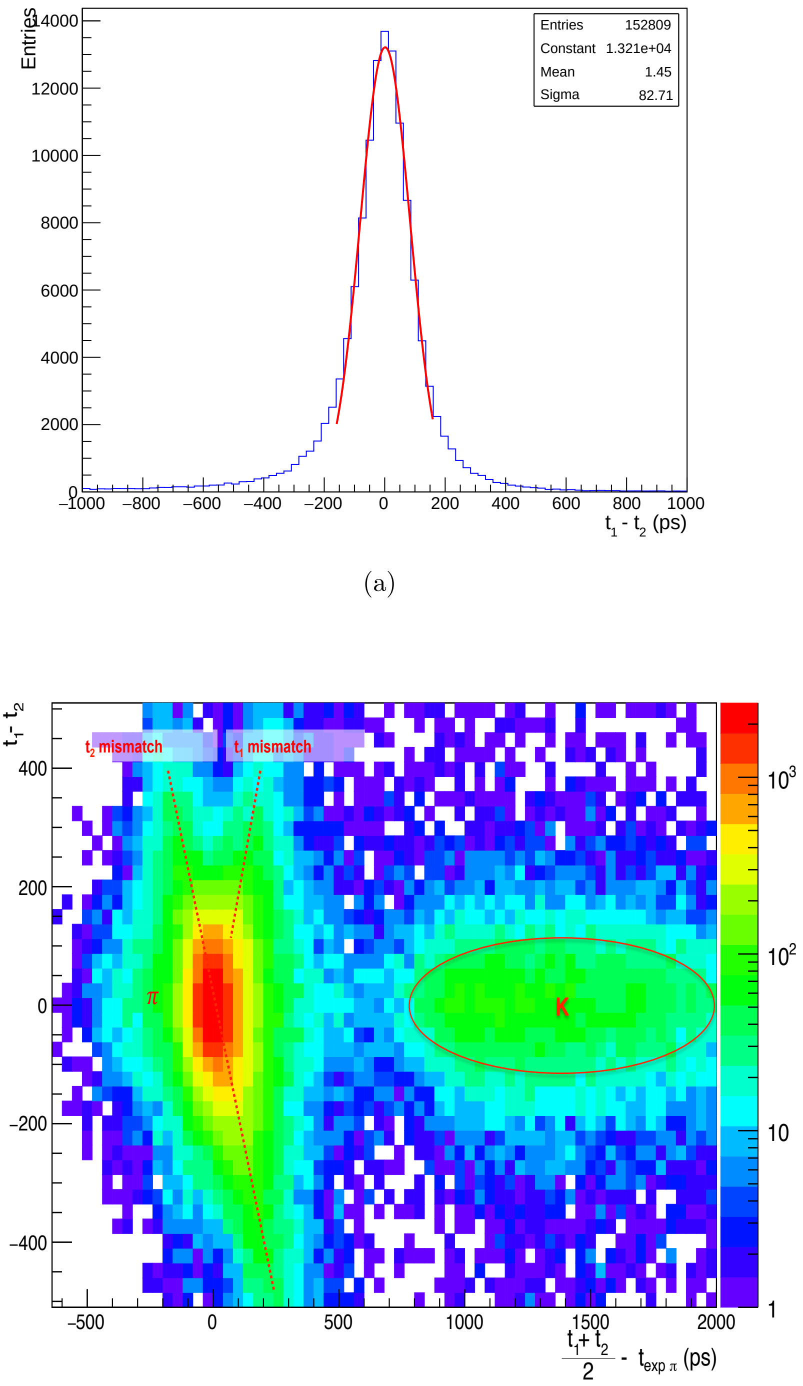

(a)

(b)

Figure 3.2: Time difference between the two pad measurements (a); time difference versus the average time minus the expected time for a pion (b), used to explain some analysis cuts (details in the text). The two (red dots) lines indicate the mismatch on t_1 and t_2 respectively; the π and K distribution are also highlighted.

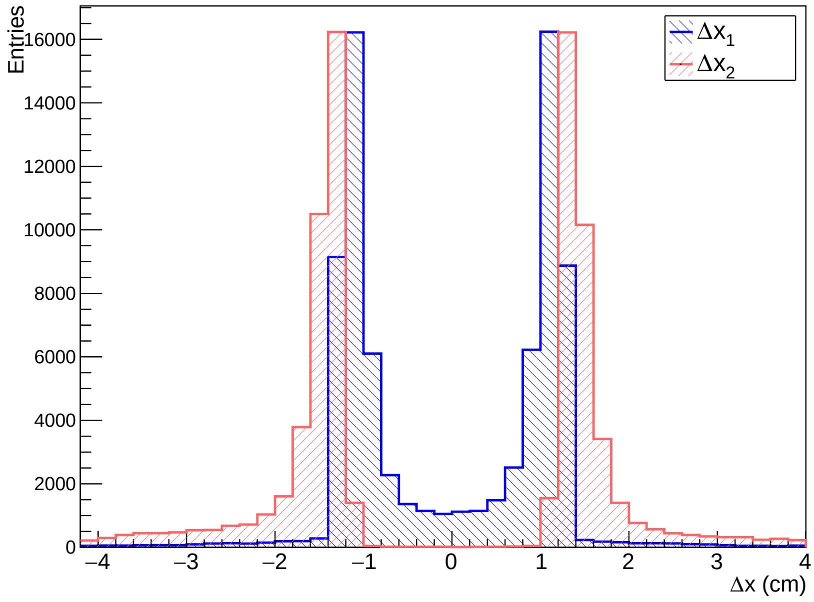

(a)

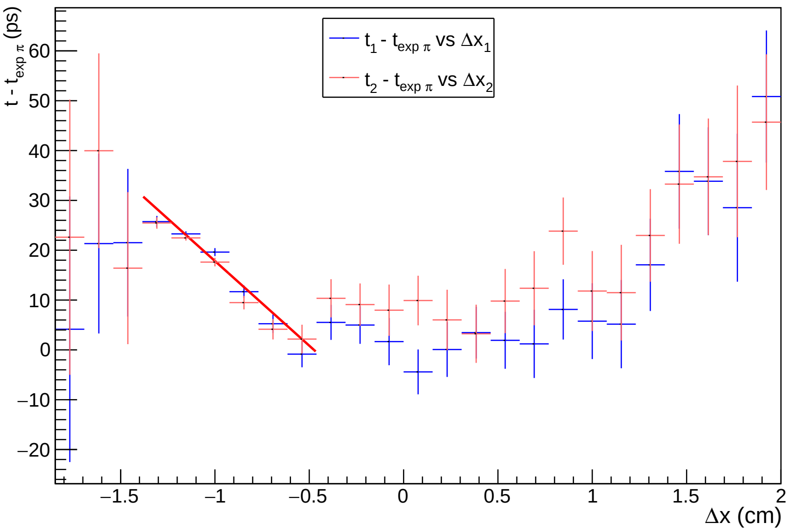

(b)

Figure 3.3: Double hit case. (a) $\Delta x_1, \Delta x_2$ residual distributions; (b) correlations between the signal position (residual) on the pad, Δx_1 and Δx_2, and time measurements, t_1 and t_2.

optimise the TOF time resolution, possible edge effects has been eliminated, i.e. correlations between the signal position (residual) on the pad (Δx_1 and Δx_2) and time measurements, t_1 and t_2; in Figure 3.3(b) the correlation plots are reported. What was observed is that, even in the double hit case, this correlation just follows what was called time walk effect (see previous section); indeed if Fig.3.3(b) is compared with Fig.3.1(a), the same behaviour is found. So, it is expected that correcting for this correlation would not lead us to any sensible improvement.

The final time measure will then be simply the average between the two time measurements[2] $(t_1+t_2)/2$; indeed putting together the two timing measurements, t_1 and t_2, starting from a time resolution of 65 ps for t_1 (and 69 ps for t_2), a final time resolution of 58 ps has been achieved, i.e. an improvement by $\sim$ 30 ps in quadrature. In Figure 3.4 the three time distributions $(t_1, t_2, (t_1+t_2)/2)$ are reported.

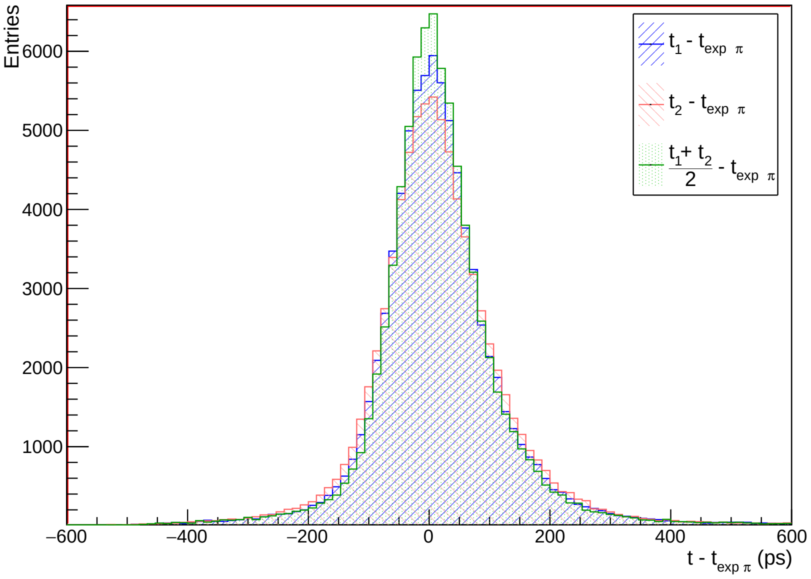

Figure 3.4: Comparison of the time distributions of the two pads, 1 and 2, and the average, minus the $t_{exp\ \pi}$.

Another goal of the clustering correction is to improve the position information. To better fit with the matching window of 3 cm, Δx has been

---

[2] One can imagine to get a better time resolution with a TOT weighted average time; instead no change has been observed, if compared to a simple average.

redefined as the distance from the edge, instead that from the centre of the pad; the recentred distance $\sqrt{\Delta x^2 + \Delta z^2}$ is reported in Fig.3.5(a) where it is compared with the initial double hit and single hit distance distribution. After the recentering (i.e. after the clusterization) the residuals appear smaller, farther from the (matching window) limit of the 3 cm.

Moreover, for the clustering analysis, we depend on the TPC tracking for the definitions of pad 1 and pad 2; if a way to define them independently from the TPC is found, there would be a double benefit: the TOF would be independent from the tracking resolution and the clustering corrections could be applied before the matching with the TPC. A way has been found, using the Time Over Threshold (TOT) measurements (in turn correlated with the charge released by the particles). Indeed a correlation between the residual Δx and the associated TOT measure was found; the pad 1(2) is redefined as the one with larger, M (smaller, m), charge (TOT); in Figure 3.5(b) the correlation between position and charge is reported. The final result is a position expressed as a function of $TOT \equiv TOT(\Delta x)$, independent from the TPC tracking.

The results obtained in the clustering studies can be applied to the real data and introduced in the Monte Carlo simulations of the TOF response, leading to a more realistic description of the system.

3.1.4 Considerations on TOF time response

To better simulate the TOF timing it is of fundamental importance to put together all the experimentally observed effects. As far as was understood from time walk and clustering corrections, it can be concluded that there are basically two observed effects: the time walk effect, and some side effects arising in the multi hit events. To simulate the TOF timing, the simulation of both the effects is needed. The whole time measurement can be divided in two parts: one due to an uncorrelated effect (same cluster, different effects) and the other due to a correlated effect (same cluster, same effects). From the multiple hit studies, the signals coming from the same avalanche can not be:

- Totally uncorrelated otherwise in the double hit case the final simulated time resolution would be less than measured, ~ 57 ps (see $(t_1 + t_2)/2$ distribution in Fig.3.4). Indeed for totally indipendent signals, the final σ would be simply the quadratic sum of the single time resolution divided by two, with $\sigma_1 \sim 65$ ps, $\sigma_2 \sim 69$ ps, i.e. 47 ps.

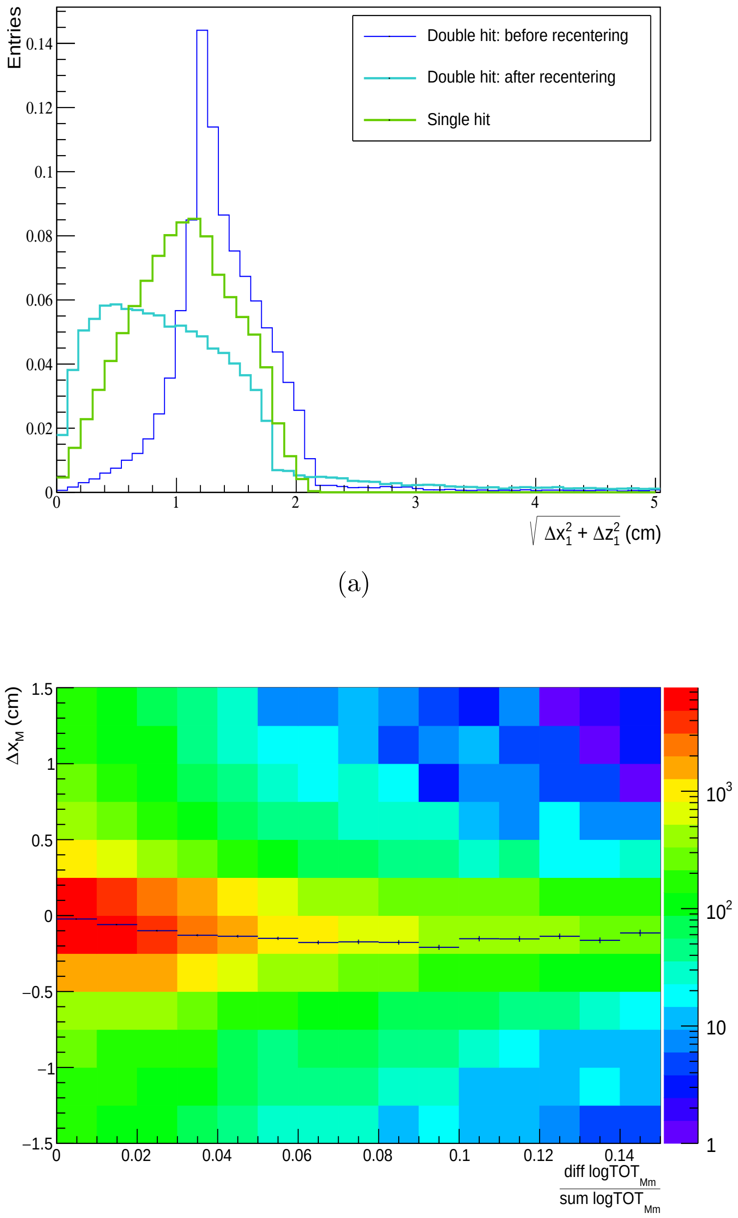

(a)

(b)

Figure 3.5: (a) Comparison of the recentred distance $\sqrt{\Delta x^2 + \Delta z^2}$ (light blue line), where the Δx has been centred in the edge between the two pads, with the initial double hit (blue line) and single hit distance, both with Δx centred in the the centre of the pad (green line). (b) Correlation between Δx and a function of TOT, with $\frac{difflogTOT_{Mm}}{sumlogTOT_{Mm}} = \frac{\log TOT_M - \log TOT_m}{\log TOT_M + \log TOT_m}$. The subscript M and m correspond to the pad with larger and smaller charge (TOT) respectively.

- Totally correlated otherwise in the double hit cases the $t1-t2$ distribution would be at zero, while it has a finite $\sigma_{diff} \sim 83\ ps$, see Fig.3.2(a).

The time resolution of a certain function $f(t_1, t_2)$ can be express by means of the covariance matrix so that:

$$\sigma_f^2 = \begin{pmatrix} \frac{\partial f}{\partial t_1} & \frac{\partial f}{\partial t_2} \end{pmatrix} \begin{pmatrix} \sigma_1^2 & \sigma_{12} \\ \sigma_{12} & \sigma_2^2 \end{pmatrix} \begin{pmatrix} \frac{\partial f}{\partial t_1} \\ \frac{\partial f}{\partial t_2} \end{pmatrix} \tag{3.2}$$

with $\frac{\partial f}{\partial t_1}, \frac{\partial f}{\partial t_2}$ the partial derivatives of the function $f(t_1, t_2)$ with respect to t_1, t_2 and σ_{12} the correlated term. In our cases, $f(t_1, t_2) = t_1 \pm t_2$ and then $\frac{\partial f}{\partial t_1} = 1$ while $\frac{\partial f}{\partial t_2} = \pm 1$. Moreover, it can be concluded that the correlation is positive $\sigma_{12} = \sigma_c^2$; indeed the time resolution of the time difference ($\sigma_{diff} \sim 83\ ps$) is smaller than the sum ($\sigma_{sum} \sim 2 \cdot 57\ ps \sim 114\ ps$). Then for each time measure there are two contributions, one uncorrelated, σ_{u_i} with $i = \{1, 2\}$, and an other positively correlated, σ_c so that:

$$\sigma_i^2 = \sigma_{u_i}^2 + \sigma_c^2 \tag{3.3}$$

$$\sigma_{diff}^2 = {\sigma_i}^2 + \sigma_j^2 - 2\sigma_c^2 \tag{3.4}$$

$$\sigma_{sum}^2 = {\sigma_i}^2 + \sigma_j^2 + 2\sigma_c^2 \tag{3.5}$$

From which:

$$\sigma_c = \frac{1}{2}\sqrt{\sigma_{sum}^2 - \sigma_{diff}^2} \sim 40\ ps \tag{3.6}$$

$$\sigma_{u_1} = \sqrt{\sigma_1^2 - \sigma_c^2} \sim 50\ ps \tag{3.7}$$

$$\sigma_{u_2} = \sqrt{\sigma_2^2 - \sigma_c^2} \sim 56\ ps \tag{3.8}$$

These results can lead to some considerations regarding the single hit cases. Indeed the time resolution of the single hit cases can be expressed as a sum of an intrinsic contribution (σ_{int}) and of the time walk contribution ($\sigma_{tw} = 44\ ps$); then, if it is assumed $\sigma_{int} = \sigma_c$, the sum of the two contributions ($\sigma_{SingleHit} = \sqrt{\sigma_{tw}^2 + \sigma_{int}^2} \sim 59\ ps$) is in agreement with what experimentally found, see Fig.3.1(b). All these correlations can then be implemented into Monte Carlo simulation to better reproduce the TOF time response.

3.2 MRPC *R&D*

With the higher pile-up of the next generation hadron colliders, $HL-LHC$ [64] and the FCC [65], the requirement of a time resolution of a few to some tens of picoseconds is becoming necessary; indeed such a good time resolution, added to the spatial information, would permit a 4-D tracking, with all the benefits, such as distinguish each track hit even in the future harsh environment.

Also under this point of view, the ALICE-TOF MRPC in still a cutting-edge detector. Indeed, as demonstrated in a beam test setup [66], it can reach a time resolution, including the whole electronic chain, of $\sim 40 - 50\ ps$ maintaining an efficiency of almost 100%; 57 ps has been achieved in the full operating ALICE-TOF detector (144 m^2). Moreover, the MRPC is relatively easy to build at a lower cost than other equivalent detectors, making it as the ideal solution to cover large areas.

However, even thought, for future plans, the ALICE-TOF MRPC is already an excellent detector, with excellent time resolution, there are some *R&D* programs which are possible: the first one concerns the improvement of the time resolution itself; the other is dedicated to improving the MRPC rate capability in view of future colliders.

It is possible to get an even better time resolution working both on the detector design itself and on the electronics (nowadays a TDC with a time resolution less than 10 ps is indeed feasible). The work presented here was focused on the study of a way to improve the time resolution of the detector itself, maintaining the others characterizing and fundamental properties.

The other fundamental *R&D* regards the rate capability; the ALICE-TOF MRPCs have indeed a limited rate capability (see Section 2.4.2) and this would exclude such an MRPC from the use in some future high rate environment. The aim of this work was to improve the rate capability of MRPC, trying to keep the other basic features of the MRPCs.

Improving time resolution: basic idea. The MRPC time resolution improves with thinner gas gaps and with the number of gas gaps (see Section 2.4.3); starting from this the idea is based on the design and construction of a chamber with a greater number of thinner gas gaps. Building an MRPC with a time resolution less than 20 ps (obtained with an oscilloscope readout), maintaining an efficiency close to $\sim$ 100%, is possible, as reported in [67]. In that work a chamber with 4-stacks and 24 gas gaps of 160 μm thickness was used. The main point of our *R&D* is to design and build an MRPC with the same performances keeping a low cost and ease of construction with respect to the 4-stack design, using less quantity of dense material as possible[3].

A chamber with the aim of improving the time resolution using a 2-stack and

---

[3] This would be important in an experiment with a calorimeter downstream the MRPC, so that the incident particle looses less energy as possible.

20 gaps has been designed and built. A schematic view of the structure of this MRPC, named MRPC(20/180), is shown in Figure 3.6(a). For details of the construction see Section 3.2.1.

Improving rate capability: basic idea. The limited rate capability of the MRPC is a big issue for future applications in a high-rate environment; the MRPCs of ALICE-TOF are made using AGC sheets of soda-lime glass as resistive electrodes, with a bulk resistivity of $5 \cdot 10^{12}\ \Omega cm$; as explained in Section 2.4.2, this high resistivity is the main factor that limits the rate capability. There are indeed low-resistivity glass sheets and ceramics being studied for use as resistive plates for high rate applications [68]. Nevertheless this kind of electrodes imply some difficulties: they are not easily produced (not common) and, as a consequence, the price is higher. In this work an attempt to improve the rate capability of MRPC, maintaining the ease of building and a low price, was made. The idea is, instead of replacing the electrode, to add a painted layer on the internal soda-lime glass sheets; with this internal resistive paint, the surface resistivity would lower, the charge will evacuate faster resulting in an increase of the rate capability.
In Figure 3.6(b) a scheme of the used structure is shown. The details of the construction are reported in the next section. The results of our *R&D* on rate capability obtained by using two different chamber designs are reported: one with both sides of the internal glass sheets painted, MRPC(4/300), and the other with only one (the *anode surface*) of the two surfaces painted, MRPC(5/250).

3.2.1 Construction of the detectors

Here the construction details of the MRPCs built for the *R&D* programs described above are reported. In particular three chambers, MRPC (20/180), MRPC(4/300) and MRPC(5/250), using the same basic materials were designed and built.
All the detectors consist of stacks of glass sheets of 280 μm thickness and $5\ 10^{12}\ \Omega cm$ bulk resistivity. The glass sheets, of $20 \times 20\ cm^2$ active area, were cut from a glass sheet of $\sim 1\ m^2$. The outer surface of the external glass sheets has been coated with a resistive paint of $5\ M\Omega/\square$; they work as electrodes where the high voltage is applied.
Due to the different application and *R&D* of the chambers the number of stacks, gas gaps and their thickness are different:

- MRPC(20/180): 20 gas gaps, 180 μm thick; double stack, 10 + 10 (Figure 3.6(a)); no internal painted layer

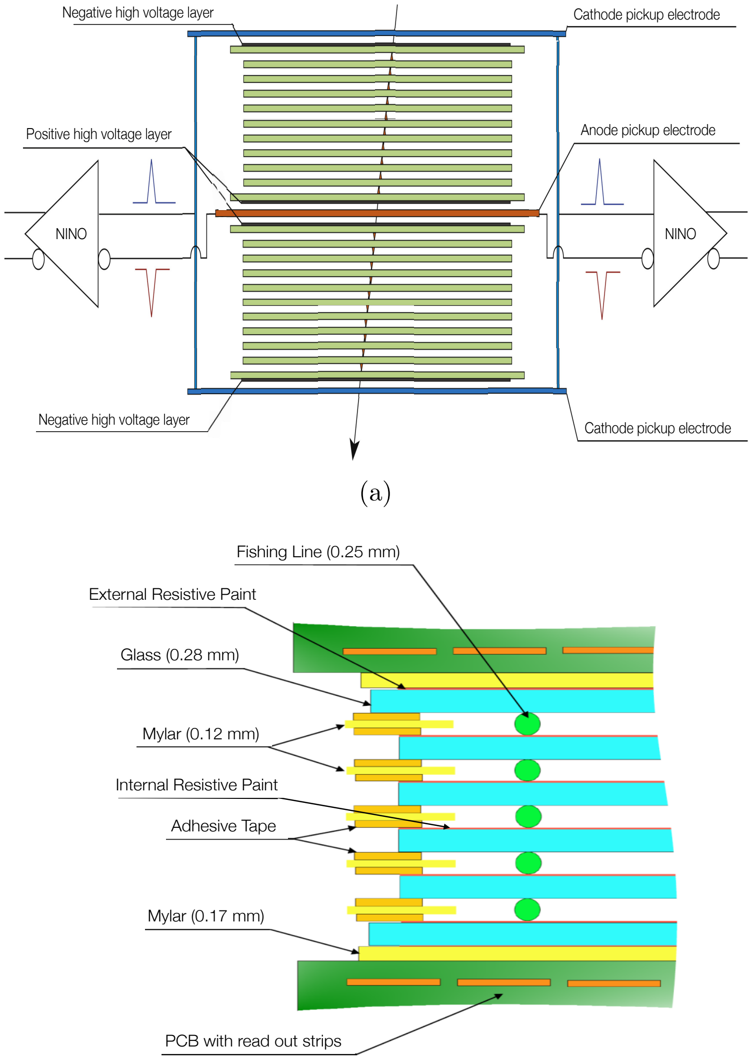

(a)

(b)

Figure 3.6: Schematic view of the design of the MRPC(20/180), the double stack structure is shown together with an inner positive high voltage layers, and two external negative high voltage layers (a). Schematic lateral view of MRPC(5/250) with construction details (b).

- MRPC(4/300): 4 gas gaps, 300 μm thick; one stack; internal resistive paint, 100 $M\Omega/\square$, on both surfaces of each sheet
- MRPC(5/250): 5 gas gaps, 250 μm thick; one stack; internal resistive paint, 100 $M\Omega/\square$, on cathode faced sheet surface (Fig.3.6(b))

The spacers between two glass sheets are mono-filament commercial fishing lines of different diameters (gas gap thickness) depending on the chamber; the fishing lines are stretched across the surface of the glass from one side to the other and around plastic screws fixed at both sides of the chamber. In Figure 3.7(a) a picture of a chamber during the assembling is reported; the fishing lines stretched across the glass sheets are visible.

The Printed Circuit Boards (PCB), three for MRPC(20/180) and two for both MRPC(4/300) and MRPC(5/250), are 1.5 mm thick and insulates 24 readout strips from the anode and cathode electrodes; the strips are (0.7×20.5) cm^2, separated by 1 mm one from the other. In Fig.3.7(b) a picture of the PCB is reported; the 24 readout strips and the connectors for the front-end electronics (in grey) are visible. Indeed each strip is readout at both sides of the strip (to improve the time resolution, avoiding the

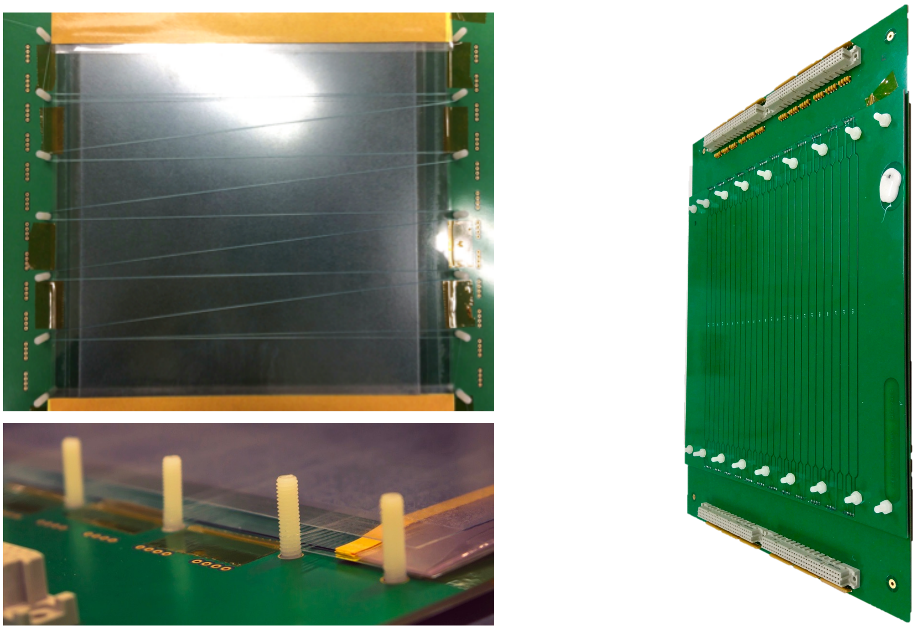

(a) (b)

Figure 3.7: Two pictures of a chamber during the assembling of the chamber: a top and a lateral view (a). A picture of the PCB used during the assembling (b).

broadening due to the hit position).

The anode and cathode boards are connected by pins, that also attach the PCBs together; thus a differential signal is sent to the front end. A honeycomb panel is attached to the PCBs with a double-sided adhesive tape, to ensure the rigidity of the structure. In Figure 3.6(b) a schematic cross section view of the chamber is reported (in particular depicted is the MRPC(5/250)). The chamber is finally enclosed in a gas-tight aluminium box and flushed with a gas mixture of 95% $C_2H_2F_4$ and 5% SF_6.

In Table 3.1 the main characteristics of the MRPCs are summarised.

	MRPC(20/180)	MRPC(4/300)	MRPC(5/250)
active area (cm^2)	20×20	20×20	20×20
No. glass sheets	22	5	6
i/e^* glass thickness (μm)	280	280	280
i/e^* glass bulk resistivity (Ωcm)	$5 \cdot 10^{12}$	$5 \cdot 10^{12}$	$5 \cdot 10^{12}$
No. gas gaps	20	4	5
gas gaps width (μm)	180	300	250
No. of stacks	2	1	1
e^* glass painted	yes	yes	yes
i^* glass painted	no	double side	one side
i^* glass paint resistivity ($\frac{M\Omega}{\square}$)	-	100	100

Table 3.1: Summary of the MRPCs main characteristics. $^*i/e = internal, external$

3.2.2 Experimental setup and electronics

After the MRPC construction, studies on their performances have been performed at the T10 test beam line at CERN. The beam was composed mainly of negative pions of 5 GeV/c momentum. For the rate capability measurement, it is of particular importance to point out that a spot illumination in a pulsed beam was used: indeed there were about 2 spills (400 ms long) per PS supercycle that has a period of approximately 22 s; this situation is different from a flood illumination.

In Figure 3.8, a schematic view of the experimental setup is reported. Three sets of scintillators coupled to photomultipliers have been used for the trigger. In particular, starting from the beam entrance, the first set ($S1-S2, S3-S4$) consists of two orthogonal scintillator bars of ($2 \times 2 \times 10$ cm^3), read at each end by photomultipliers. The second set is made of a pair of crossed scintillators ($P1 - P2$) with a crossed area of 1×1 cm^2, read by photomultipliers.

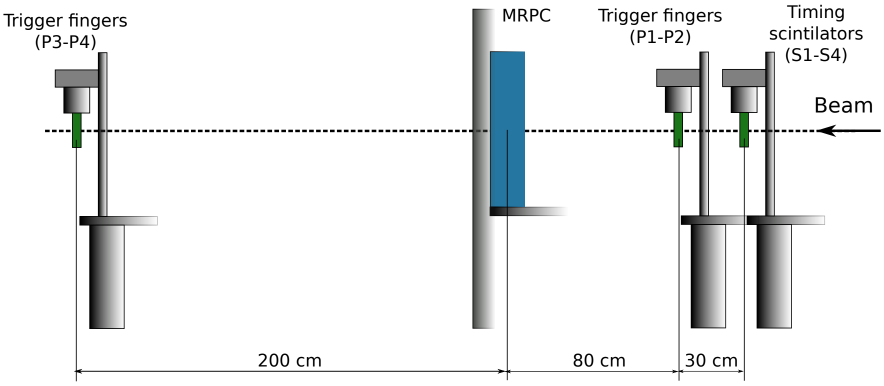

Figure 3.8: Schematic view of the experimental setup at CERN T10; the three sets of scintillators coupled to photomultipliers used for the trigger are visible.

Next there is the MRPC under test and finally the last pair of crossed scintillators ($P3-P4$), with a crossed area of $2 \times 2\ cm^2$, read by photomultipliers. $S1-S2, S3-S4$ are also used as timing reference, t_0, by means of the average between all the detectors ($(S1+S2+S3+S4)/4$). A t_0 time resolution of $40-50\ ps$ has been measured, calculated from the time difference $((S1+S2)/2-(S3+S4)/2)$.

The front end and readout electronics consist of a NINO-ASIC chip and an HPTDC, the same used by the ALICE-TOF detector and already described in Section 2.5.4. A 160 $mV(\sim 40\ fC)$ for the NINO threshold has been used.

3.2.3 Results and discussion

In this section the results obtained in the beam tests at CERN are reported. At the beginning the results obtained with MRPC(20/180) are shown and discussed.

MRPC(20/180): This chamber was built with the aim of improving the time resolution maintaining other MRPC characteristics. The efficiency as a function of the applied voltage has been measured. As shown in Figure 3.9(a), an efficiency of almost 100% at a voltage of 21 kV has been reached. The dark current as a function of applied voltage has been also measured; as expected, it increases with voltage but it never exceeded the maximum value of 0.2 μA, reached at 22 kV.

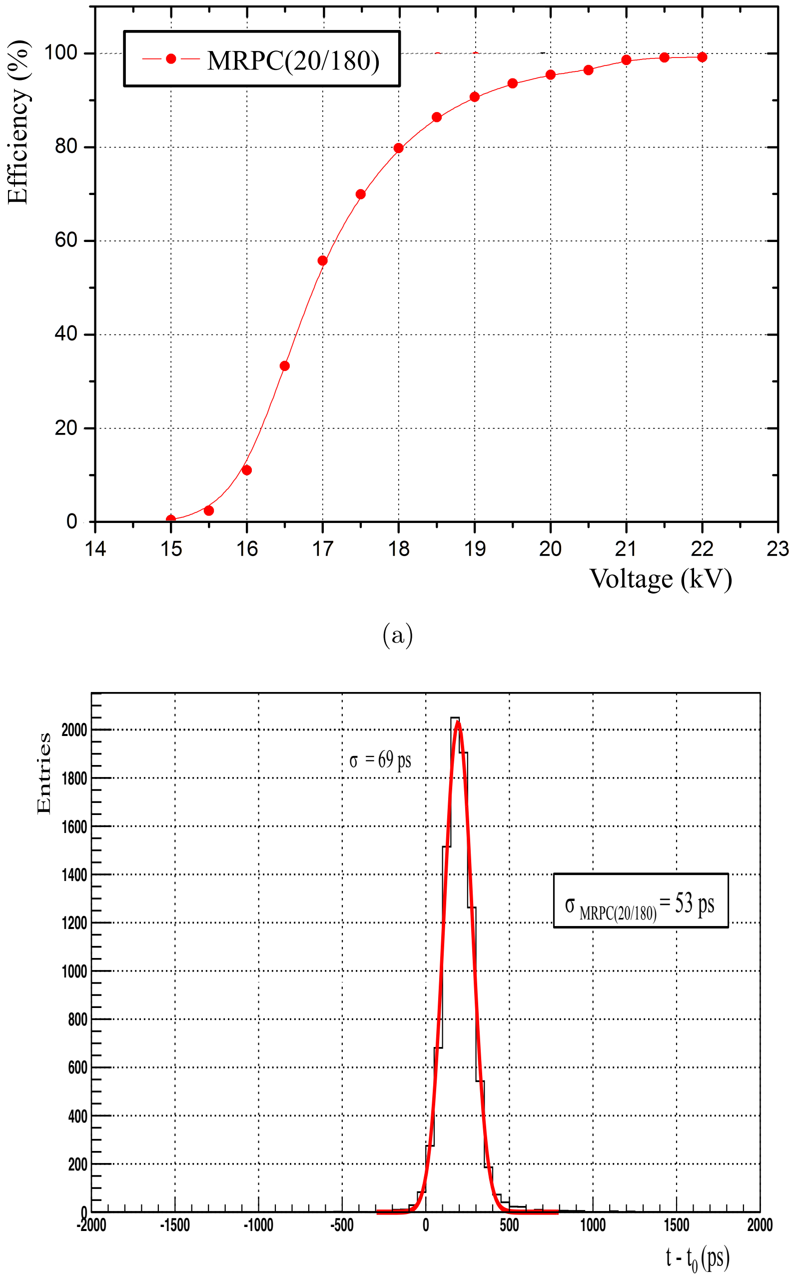

(a)

(b)

Figure 3.9: The efficiency as a function of the applied voltage (a) and the time resolution at 21 kV (b) for the MRPC(20/180).

As second step, the time resolution of the detector was investigated. In Figure 3.9(b) an histogram of the time difference measured between the MRPC(20/180) and the reference scintillators is shown. To get the final time resolution the jitter of the scintillators ($\sigma_{t_0} = 44\ ps$) has been quadratically subtracted, resulting in a time resolution of $(53 \pm 1)\ ps$.
From the results on efficiency and (dark) current, it can be concluded that the chamber is perfectly working, with a low current and a high efficiency; moreover, with our design, the difficulties on the construction (less number of stacks), the price (less material) and the quantity of dense material used (a total of three PCBs have been used and less number of thinner glass sheets) have been sharply reduced, w.r.t. a previous work [67].
Concerning the time resolution, it should be pointed out that the reported time resolution is of the whole system, including the full chain of front end and readout electronics. The results obtained are dominated by the electronic readout jitter.
The next step, after this first testing stage, would be to test the chamber with an appropriate readout electronics, with a dramatically smaller jitter, e.g. an oscilloscope (as in [67]), in order to measure the intrinsic time resolution of the MRPC(20/180).

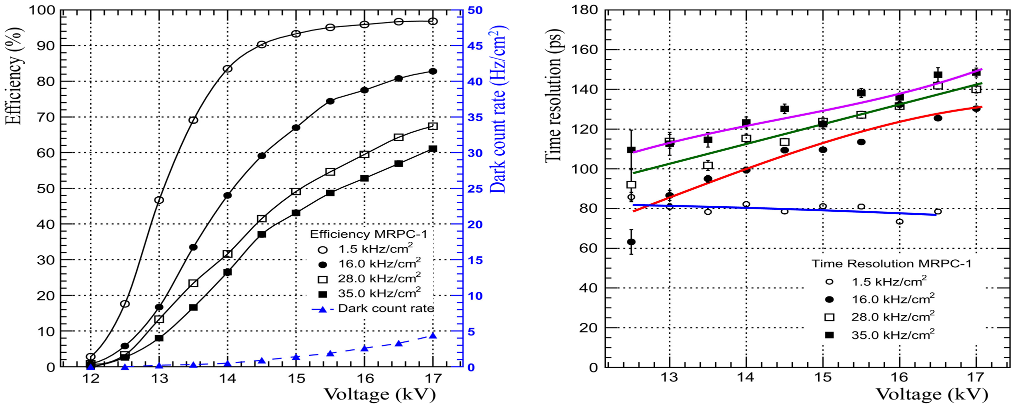

(a) (b)

Figure 3.10: Efficiency, dark count rate (a) and time resolution (b) versus the voltage as a function of the rate of particles for a standard chamber, MRPC-1.

MRPC(4/300) and MRPC(5/250): these chambers were built with different designs and with the aim of improving the MRPC rate capability; as mentioned, a spot illumination in a pulsed beam has been used. With

higher rates a degradation of both the efficiency and time resolution is expected.
This can be observed in Figure 3.10 [69] where the results of a test on a standard MRPC (without any inner painted layer added), MRPC-1, are reported. The chamber is a six gas gaps of 220 μm width. These plots will be compared with the results from MRPC(4/300) and MRPC(5/250).

To test the chambers MRPC(4/300) and MRPC(5/250), the rate of particles provided by the T10 beam line has been increased; the aim was to measure the efficiency, the dark current and the time resolution as a function of the applied high voltage and for increasing values of rate. The T10 trigger sets (see previous section) have been used to monitor the rate; the beam intensity has been changed modifying the collimator aperture. Four different rates have been tested, from 7 kHz/cm^2 to 40 kHz/cm^2.
In Figure 3.11(a) and 3.11(b) the results for the MRPC(4/300), the double side painted, are reported; in particular the efficiency, current and time resolution versus the voltage, for the various rates, are shown. In Figures 3.12(a) and 3.12(b), the same kind of plots for MRPC(5/250), the single side painted, are shown.

At the rate of 7 kHz/cm^2, the MRPC(4/300) reaches the plateau at ~ 9 kV with an efficiency of $\sim 78\%$; the MRPC(5/250) reaches the plateau at ~ 14 kV with an efficiency of $\sim 93\%$. These differencies in efficiency and voltage are just due to the different thickness and number of gaps.
Moreover, the plots show the clear dependence of the efficiency and time resolution with the rate on both detectors. It is interesting to compare the present results with those of a standard MRPC, see Fig. 3.10. In the standard chamber, starting from a rate of 1.5 kHz/cm^2 to 35 kHz/cm^2, at 16.5 kV, there is a degradation of $\sim 38\%$ in efficiency and of $\sim 44\%$ in time resolution. In MRPC(4/300) the degradation at 11 kV are of $\sim 40\%$ and $\sim 30\%$ for efficiency and time resolution respectively; while in MRPC(5/250), at 15 kV, a degradation of $\sim 15\%$ for efficiency and of $\sim 39\%$ for time resolution is observed.

The results have been obtained keeping the low cost requirement and ease of construction of the MRPCs. Concerning the time resolutions, the same behaviour of the standard MRPC have been observed.
It can be noticed that the expected better results for the double sided painted MRPC (4/300) w.r.t. the MRPC(5/250), have not been observed. It can be concluded that the *hand* painting of the inner glass sheets can lead to some non uniformity on the thickness of the painted layer; this can affect the results. Anyway, to fully compare them, two identical chambers, except for the

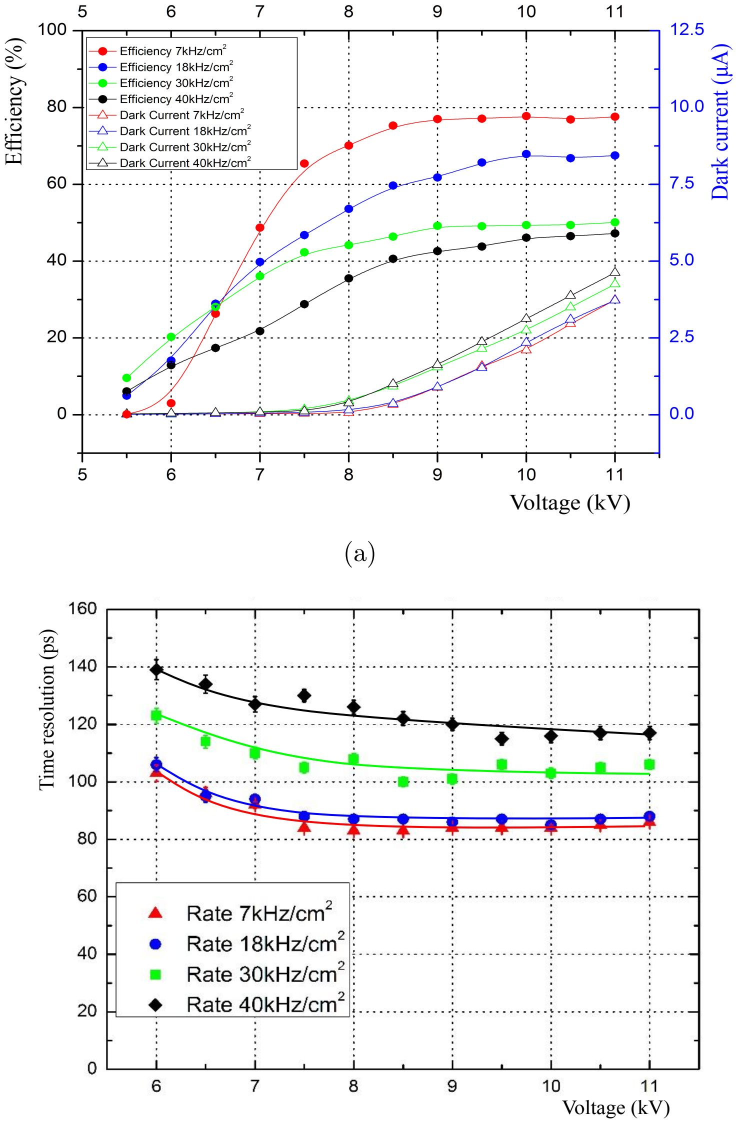

(a)

(b)

Figure 3.11: Efficiency, dark current (a) and time resolution (b) versus the voltage as a function of the rate of particles for MRPC(4/300), the double side painted. The errors are within the symbol size; the lines are to guide the eye.

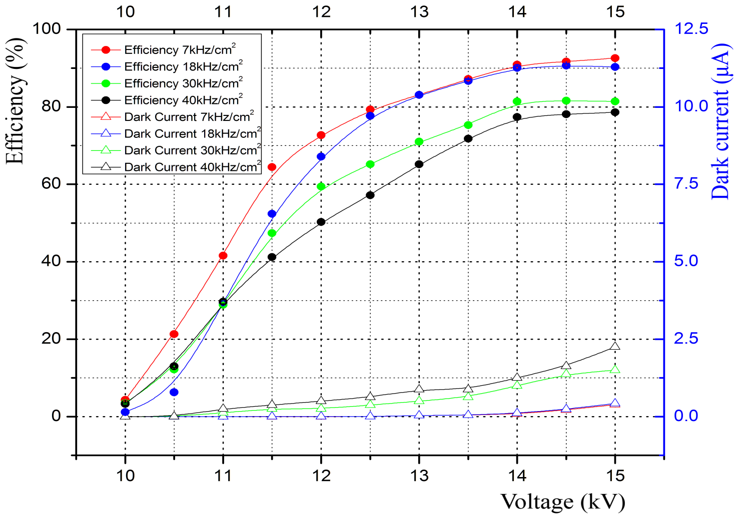

(a)

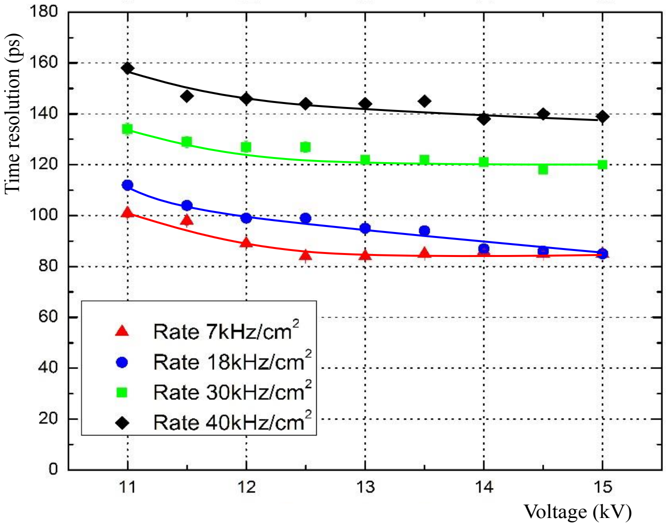

(b)

Figure 3.12: Efficiency, dark current (a) and time resolution (b) versus the voltage as a function of the rate of particles for MRPC(5/250), the one side painted. The errors are within the symbol size; the lines are to guide the eye.

different way of painting, should be built.
The results, that are a first stage of this *R&D* in rate capabilities improvements for MRPC, demonstrate that the principle is working; indeed in MRPC(5/250) a lower degradation of efficiency with increasing rate has been observed w.r.t. standard MRPCs. In Figure 3.13 the final results on efficiency are highlighted. The final step will be then to have a *factory-painted* glass sheets and repeat the tests.

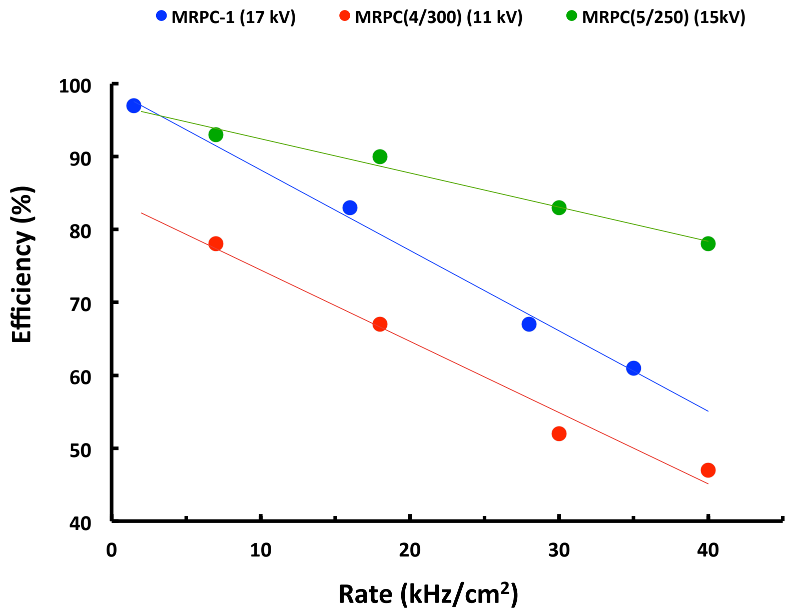

Figure 3.13: The efficiency versus the rate at a plateau voltage for a standard chamber MRPC-1 (with 6 gas gap of 220 μm) and the two chambers tested, MRPC(4/300) (double side painted) and MRPC(5/250) (one side painted). The errors are within the symbol size; the lines are to guide the eye.

Chapter 4

SiPM

More and more experiments are searching for detectors that can cover large areas (as in the present LHC experiments) with good timing performances, insensitivity to magnetic field and of low cost. A detector based on scintillators coupled to Silicon PhotoMultipliers (SiPM) can fulfil these requirements. The SiPM have also other excellent characteristics like high efficiency, single photon sensitivity, high gain with low voltage; they are also compact and robust and they have a low power consumption $\sim 50\ \mu W/mm^2$. All these excellent features if combined with an excellent time resolution can lead to a cutting-edge detector for timing application, suitable both in the next generation of collider experiments (in nuclear physics) and in medical physics.
An *R&D* on SiPM time resolution has been performed. Here the results obtained using both a cosmic ray setup and a beam test setup are reported. Both the experimental setups are illustrated together with the front-end and readout electronics used to perform the measurements. SiPMs from a manufacturer have been identified and coupled to a fast scintillator; to study the time resolution of this kind of detector a cosmic ray test setup has been installed at Bologna INFN[1] laboratories; here preliminary studies have been performed. During this phase the possibility to use optical fibers to move the sensor away from the hypothetical high-radiation area was also investigated. The study was comprehensive of a particular attention to the front-end and readout electronics used, to optimise the time measurements. Finally, dedicated measurements on the T10 test beam at CERN have been performed.

---

[1] Istituto Nazionale di Fisica Nucleare

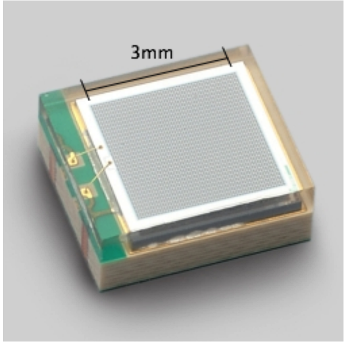

Figure 4.1: Hamamatsu S12572-050P MPPC.

Parameter	S12572-050P
Effective area (mm^2)	3×3
Pixel pitch (μm)	50
Number of pixels	3600
Fill factor (%)	62
Spectral range λ (nm)	320-900
Gain	$1.25 \cdot 10^6$
Recommended op. voltage (V)	67.6 ± 10.0

Table 4.1: Properties of S12572-050P MPPC.

4.1 Detectors and preliminary measurements

The SiPMs tested are the MPPC (Multi-Pixel Photon Counter) S12572-050P [70] produced by Hamamatsu (Figure 4.1). They have an active area of 3×3 mm^2 with a 50 μm pixel pitch. In Table 4.1 the main characteristics of this photodetector are reported. In Figure 4.2(a) the S12572-050P Photon Detection Efficiency (PDE) is reported.
The SIPMs were tested coupled both directly or by means of optical fibers to a plastic organic scintillator. The optical fibres solution was considered to test the possibility of using this photodetector away from a high-radiation environments; in particular the time resolution degradation with the fiber's length was evaluated.

The used scintillator is a plastic scintillator BC-420 [71] of $2\times2\times3$ cm^3, see Figure 4.3. This scintillator has been specially developed to perform ultra fast time measurements; in Table 4.2 the main characteristics of the scintillator are reported. The speed of photons inside the scintillator is 19 cm/ns. This means, for a 3 cm path length, a transit time of 158 ps; so the arrival time spread in 3 cm is about 46 ps ($158/\sqrt{12}$).
Figure 4.2(b) shows the light output curve of the BC-420. As you can see, the peak is in proximity of the SiPM PDE peak.

As optical fibers a plastic WLS BCF-92 [72] was used. They are fast wavelenght shifter fibres (decay time 2.7 ns); they are used here just as light guides. However, they shift the light from blue to green, with an emission peak of 492 nm (again in proximity of the SiPM PDE peak); the optical fibers main characteristics can be found in Table 4.3. The time resolution behaviour as a function of the fibre's length has been studied; fibers of two different lengths have been used: 10 cm and 35 cm.

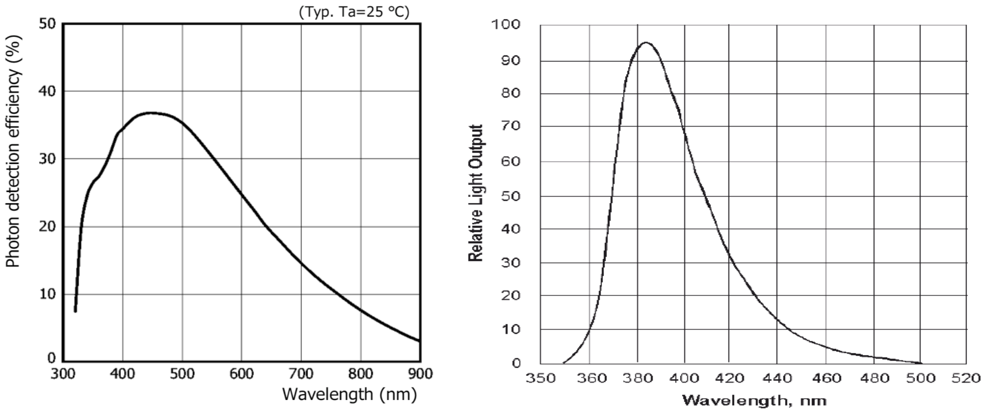

(a) (b)

Figure 4.2: S12572-050P SiPM PDE (a). BC-420 scintillator light emission curve (b).

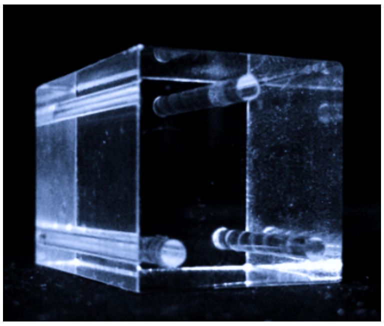

Figure 4.3: Picture of BC-420 scintillator.

Parameter	BC-420
Base	Polyvinyltoluene
Wavelength of Max. Emission	391 nm
Refractive index	1.58
Bulk Light Attenuation Length	110 cm
Ratio $H : C$ Atoms	~ 1.1
Decay Time	1.5 ns

Table 4.2: Properties plastic scintillator BC-420.

Parameter	WLS BCF-92.
Emission color	green
Emission peak	492 nm
Decay time	2.7 ns
Core material	polystyrene
Core refractive index	1.60
Cladding material	acrylic
Cladding refractive index	1.49
No. of H atoms per cc (core)	$4.82 \cdot 10^{22}$
No. of C atoms per cc (core)	$4.85 \cdot 10^{22}$
No. of electrons per cc (core)	$3.4 \cdot 10^{23}$

Table 4.3: Properties of WLS BCF-92 fibers.

The typical signal in a beam test of a track passing a scintillator directly coupled to a SiPM is reported in Figure 4.4, after an amplification by a factor ten. This signal can be compared with the single-pixel signal depicted in Figure 2.27(a).

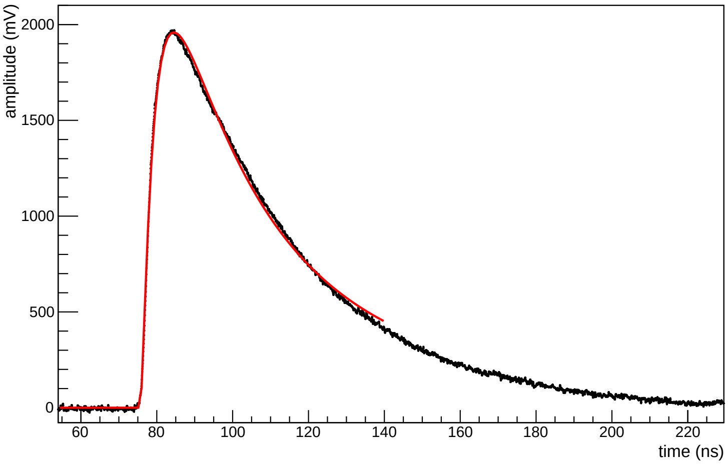

Figure 4.4: Hamamatsu S12572-050P SiPM signal, readout by an oscilloscope, after an amplification of a factor ten, in a beam test; in red a fit (using a gaussian function $G(log(x))$) of the signal.

4.1.1 Preliminary measurements

In this section some preliminary measurements are reported.
An important parameter is the voltage applied to the SiPM. So, to identify the breakdown voltage, the current as a function of the reverse applied voltage ($I-V$ curve) was measured. In Figure 4.5 the $I-V$ curves for two tested SiPMs are shown (named A and B in the legend). In both cases above 65.6 V the current starts to increase with reverse bias. The maximum operation voltage has been set to 70 V; above that value the current increases rapidly.

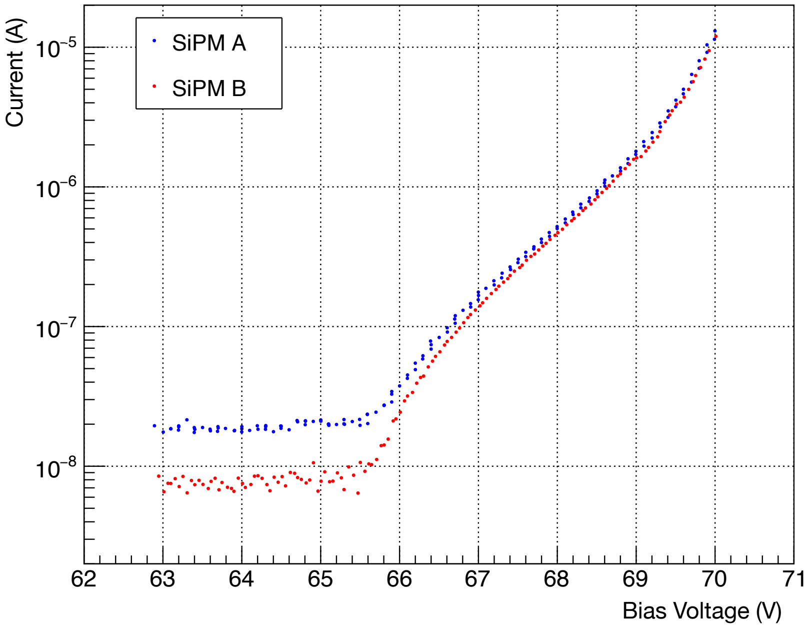

Figure 4.5: $I-V$ curves of two (A and B) tested SiPMs S12572-050P produced by Hamamatsu.

Another important parameter is the gain of the SiPM. For this purpose, the SiPM has been enlightened with a LED blue light with very low intensities. In this way it was possible to have even single photons hitting the detector. The signal from the SiPM has then been amplified by a Gali52 chip, the same used in Section 5.2.1, with an amplification of a factor 10 (20 dB). The charge photon spectrum has then been studied. This was possibile using an ADC, the same used in Section 4.2.1.
In Figure 4.6 two spectra are reported. The several peaks correspond to the

pedestal (0 photoelectron), 1 photoelectron, 2 photoelectrons, etcetera.

To study the single photon spectrum, two different methods have been used; the first one, the classic one, consisted in fitting the peaks using n gaussian functions, with n equal to the number of peak you want to fit, see Fig. 4.6(a). The output parameters will then be 3 for each fitted peak: the amplitude of the peak (first parameter), its position along the x-axis (second) and the gaussian σ (third); taking the average distance between one peak to the other, it was then possible to evaluate the gain. The second method, more elegant and innovative, consists in fitting the spectrum with a single more complex function based on a more physical interpretation of the detection process [73], see Fig.4.6(b); the output function parameters are several. In particular one of this is the gain; other interesting output parameters are the position of the pedestal (ped), the standard deviation of the pedestal (sigma0) and the average of photons detected (Av.#p.e.). As expected, with this low intensity light, the $Av.\#p.e. = 1.6$.
The gain, expressed in a.u., calculated using method one is 10.3 ± 0.1, compatible with the gain from the second method, 10.2 ± 0.1.
These measurements have been taken at a voltage of 69 V, using the ADC; to get a measurement in pC, is then necessary to convert the ADC channels. For the 12 bit used, the conversion is 4 $channel/pC$. Then dividing by ten this value (the amplification factor), the charge due to each photoelectron was $Q_{p.e.} = 0.257\ pC$. The final calculated gain G is then:

$$G = \frac{Q_{p.e.}}{q_e} = 1.6 \cdot 10^6 \tag{4.1}$$

with q_e electron charge. This value is close with the one given by Hamamatsu, see Table 4.1.

Another interesting estimate that can be done is the average number of photons detected (i.e. number of SPADs on or rather number of photoelectrons) due to the passage of a charged particle in the scintillator. In general, to perform this estimation, the charge distribution is considered; using the Landau Most Probable Value (MPV) and dividing it by the charge of a single photoelectron (see Eq.2.51), the average number of photoelectron is obtained. The photoelectron charge including amplification (a factor 10 by the Gali52, see above) is $Q_{p.e.,ampl} = 2.57\ pC$. To measure the MPV, an oscilloscope was used to measure and integrate the signal observed in the beam set up , such as the one in Fig.4.4; since the resistance is $R = 50\ \Omega$, the final results obtained is:

$$No._{p.e.} = \frac{1}{Q_{p.e.,ampl}} \frac{\int V dt}{R} = \frac{1}{2.57\ pC} \frac{80665\ mVns}{50\ \Omega} = 628 \tag{4.2}$$

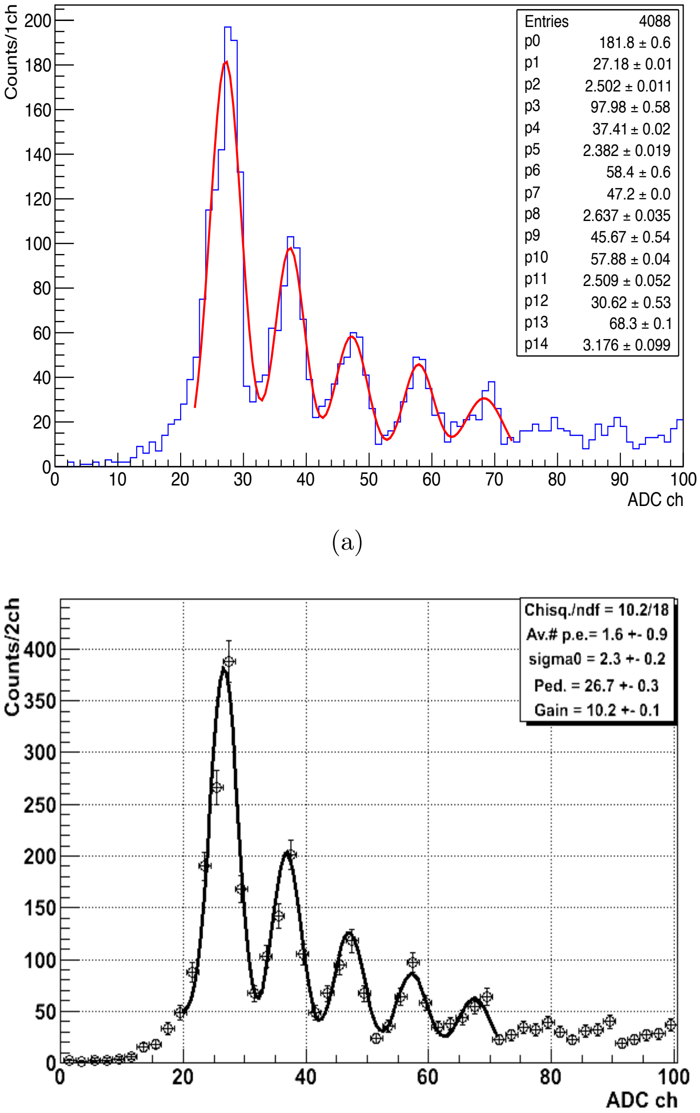

(a)

(b)

Figure 4.6: Charge single photon spectra of the Hamamatsu S12572-050P MPPC at a Voltage of 69 V, after an amplification of 10. (a) the spectrum (Counts/1ch) has been fitted using 5 gaussian functions; (b) the spectrum (Counts/2ch) has been fitted in according to [73].

To summarise, $No._{p.e.} = 628$ represents the number of photoelectrons, or rather number of the turned on pixels, after the impinging of photons created due to the passage of a track through the scintillator.

Starting from a TOT (i.e. the charge) distribution (see Fig.4.10), an alternative rough estimate of the average number of photoelectrons can be also performed. The distribution can be approximated using the Poisson distribution (see Eq.1.23); knowing that the mean ν of the Poisson distribution is proportional to the number of photoelectrons ($\nu \propto No._{p.e.}$), and then the standard deviation is $\sigma \propto \sqrt{No._{p.e.}}$, the average number of photons detected in the beam test set up is:

$$No._{p.e.} \sim \left(\frac{\nu}{\sigma}\right)^2 = \left(\frac{1.413 \cdot 10^5}{5.656 \cdot 10^3}\right)^2 = 624 \tag{4.3}$$

This number is very close with the one previously calculated.

4.2 Experimental setup and electronics

The detector performances were initially studied in a cosmic ray setup and then in a beam test setup.

As mentioned, the time resolution was measured using a direct and fibers coupling between SiPM and scintillator; in both cases two SiPMs were used. In the direct coupling the two SiPMs are placed at the surfaces of the scintillator (see Figure 4.7(a)) coupled by optical grease; the two SiPMs are then at a distance of 3 cm. In the case of coupling by means of fibers, three WLS were used, inserted into the scintillator (where previously three holes were realized, see Figure 4.3); in Figure 4.7(b) a picture of the geometrical configuration for three fibers of 10 cm is reported.

4.2.1 Cosmic Rays setup

To measure the time resolution of the SiPM a cosmic rays telescope (Figure 4.8) has been set up at Bologna INFN laboratories. The telescope is constituted of three plastic scintillators; the top (A) and bottom (C) ones ($1.5 \times 2 \times 2\ cm^3$) are coupled to standard PM and are used as trigger for the acquisition system and reference (t_0) for the time measurements. The middle scintillator (B), $2 \times 2 \times 3\ cm^3$, see below, is the one coupled to the SiPMs under test.

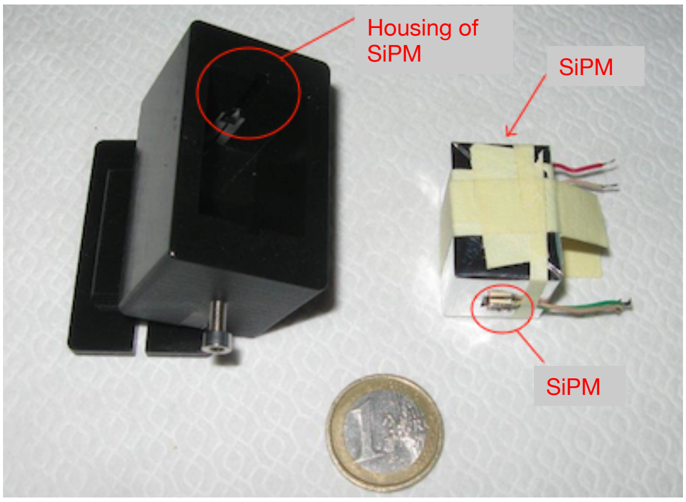

(a)

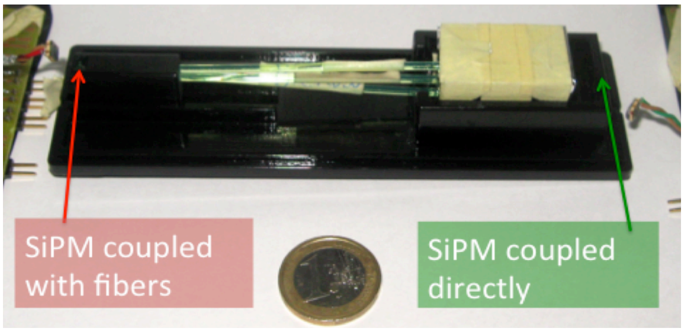

(b)

Figure 4.7: Picture showing the SiPMs couplings to the scintillator; direct (a) and by means of fibers (b).

Finally the telescope was inserted inside a box in order to maintain a constant temperature of $18^o\ C$ through a chiller. This allows to keep constant the SiPM performances; this is of particular importance in a cosmic rays test, because of the long period of data taking needed to reach an adequate statistic.

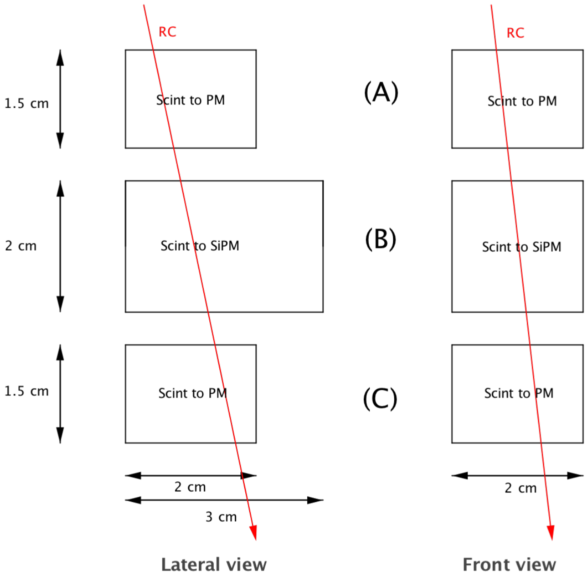

Figure 4.8: Schematic drawing of cosmic ray telescope used to measure the time response of SiPM.

As front-end electronics, a NINO-ASIC card (see Section 2.5.4) has been used. The $LVDS$ [2] output signals have been adapted to be measured using standard CAMAC modules (TDC and CIA) [74]. A CAEN Mod. C414 CAMAC Time to Digital Converter (25 ps time resolution) has been used to perform time measurements and a CAEN Mod. C205 Charge-Integrating ADC (CIA) to perform charge measurements. In this way the TOT (or rather the charge) was also measured for both the SiPM and the standard PMs.

4.2.2 Beam test setup

The same trigger and time reference setup used for MRPC tests (see Section 3.2.2) was adopted to measure the time resolution of the SiPMs (same kind

---

[2] Low-Voltage Differential Signal

of the ones used in the cosmic ray setup); see Figure 4.9 for a schematic view of the setup.

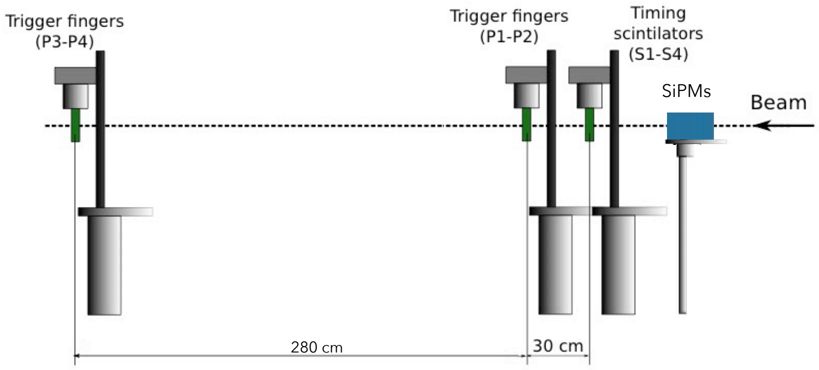

Figure 4.9: Schematic view of the experimental setup at CERN T10; the three sets of scintillators coupled to photomultipliers used for the trigger are visible.

The NINO-ASIC card as front-end electronics and the HPTDC as readout have been used, the same electronics used in the ALICE-TOF (see Section 2.5.4). Then the final time measurements were obtained with the most selective trigger, i.e. the coincidence of PMs of Figure 4.9.

4.3 Results and discussion

In this section the data analysis and the results obtained will be discussed. The common parts will be discussed first, then the results for the cosmic ray and beam test setup will be presented. In this setup for each event the time and charge collected by the PMs are recorded and can be used for the selection criteria (applied to select cosmic ray events above background). For the beam test setup the standard PMs charge was not recorded so the selection criteria were based only on the timing.

For each event (both in cosmic ray and beam test set up) the time and the Time Over Threshold (related to the charge) of the two SiPMs were measured. In Figure 4.10 a typical TOT distribution in the beam test setup is shown; to better fit it a convolution of a Gaussian and a Landau was used (see Section 1.1.2.1).

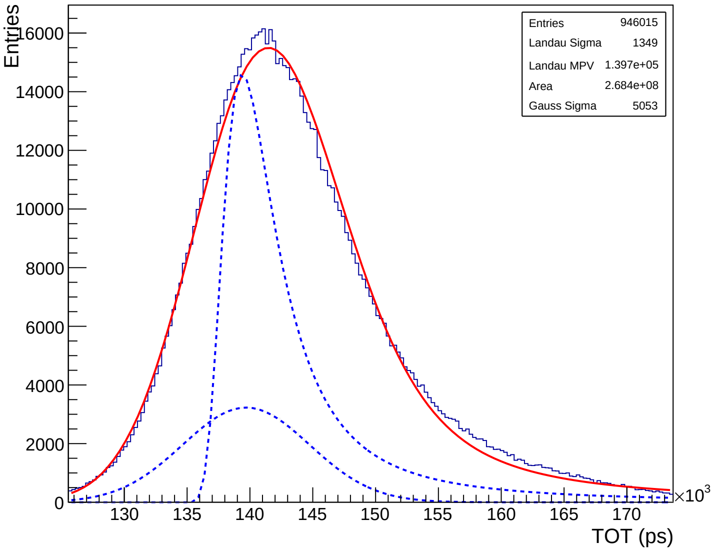

Figure 4.10: The TOT distribution of a SiPM in the beam test setup; in this particular case a threshold for the NINO of 400 mV and a voltage on the SiPM of 69.5 V were applied. To fit it a convolution of a Gaussian and a Landau was used.

The time measurements have been corrected for the time slewing effect (see Section 1.5.3). In Figure 4.11(a) the correlation between the TOT and the time of a SiPM is shown; the distribution has been fitted by means of a third degree polynomial. In Figure 4.11(b) the time measurements corrected for time slewing (subscript ts) versus TOT is reported. Through these corrections an improvement up to 16 % of the time resolution has been achieved.

To calculate the time resolution (after the time slewing corrections), a different approach has been chosen depending on the experimental setup. For cosmic ray (cr) events the difference of the arrival times of the two SiPM signals ($\Delta t = t_{SiPM\ A} - t_{SiPM\ B}$) has been considered; in this way it is possible to eliminate systematic errors due to the less controlled situation compared to the beam test. The Δt distribution obtained in various configurations (with and without fibers) has been fitted using a gaussian function; in Figure 4.12(a) the time distribution for the direct coupling is reported. The σ of this distribution is realated to the detector time resolution. In the case of direct coupling, the time resolution of the detector is obtained from

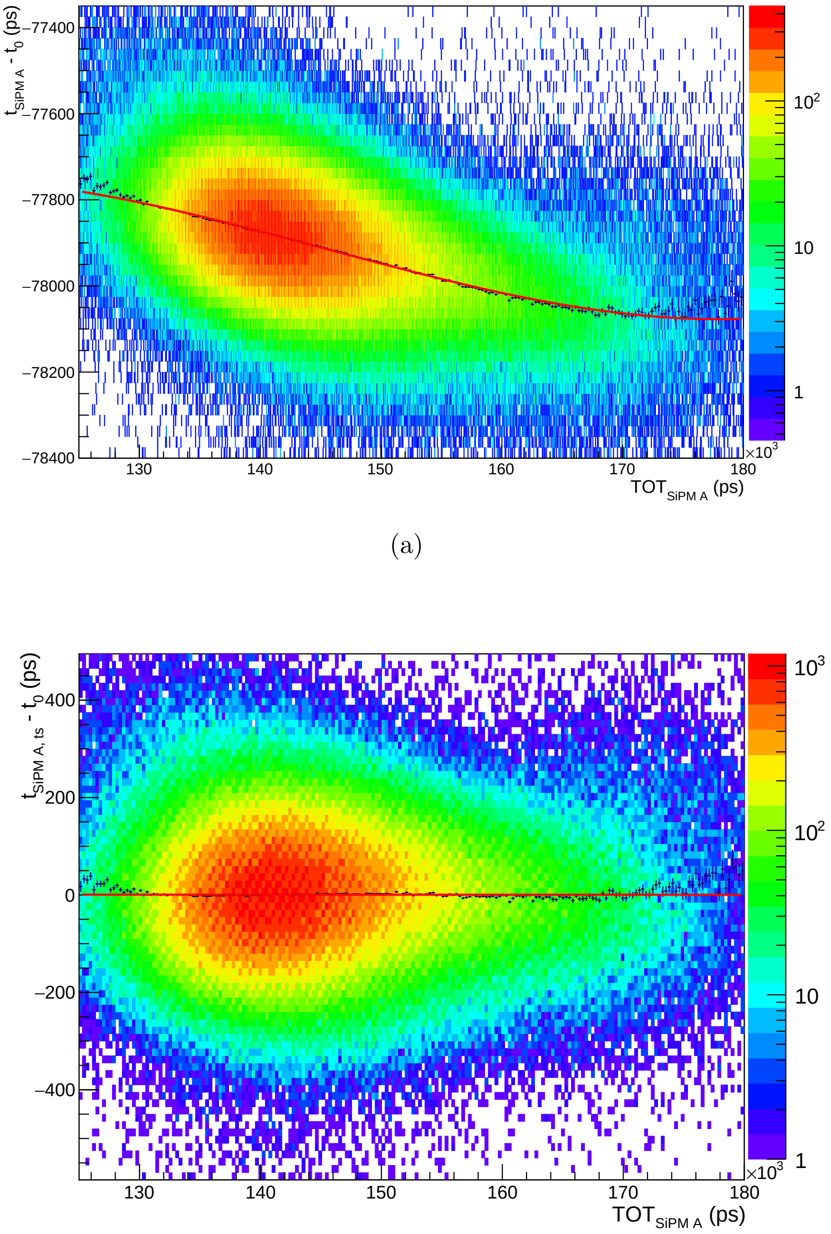

(a)

(b)

Figure 4.11: Correlation between the $TOT_{SiPM\ A}$ and the time measurement $t_{SiPM\ A} - t_0$ before (a) and after (b) time slewing correction in the beam test.

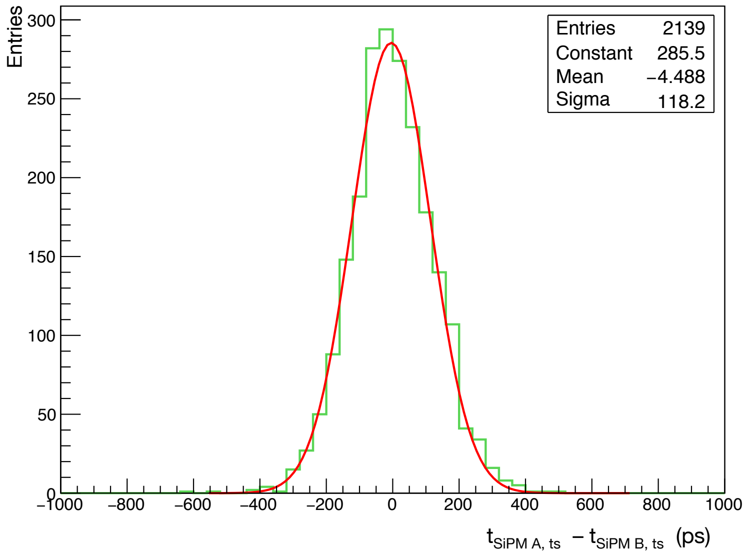

(a)

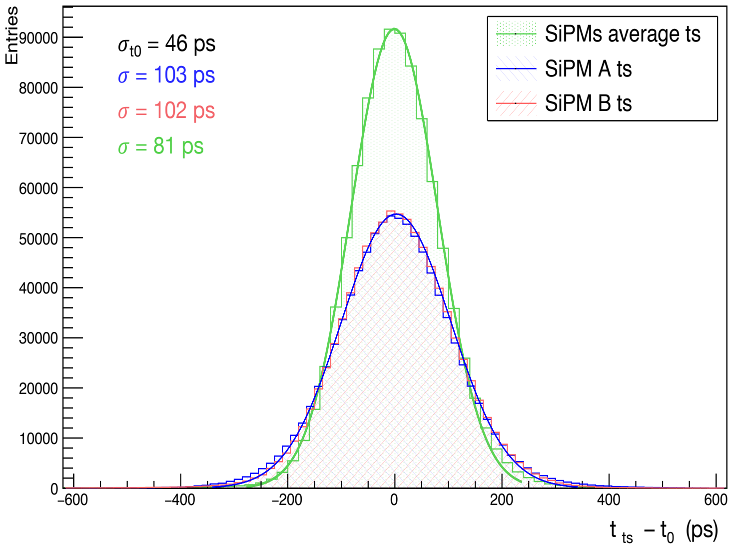

(b)

Figure 4.12: (a)Δt distribution obtained in the cosmic ray setup for the case of SiPMs directly coupled to the scintillator with an applied voltage of 68.5 V. The subscript ts indicates the measurements after the time slewing correction has been appplied. (b) Δt distributions obtained in a beam test setup with a applied voltage of 69.5 V and a NINO threshold of 400 mV; the time resolutions of the several distributions are reported in addition with the t_0 time resolution.

the σ using the following formula:

$$\sigma_{direct_{cr}} = \frac{\sigma}{\sqrt{2}} \tag{4.4}$$

Concerning the coupling by means of fibers, since in this scenario only one SiPM was coupled by means of fibers, while the other was coupled directly (see Fig.4.7(b)), the time resolution of the detector is obtained using the following formula:

$$\sigma_{fiber_{cr}} = \sqrt{\sigma^2 - \sigma^2_{direct_{cr}}} \tag{4.5}$$

where σ is the one obtained from the gaussian fit.

In the beam test (bt) setup the results both for the time of arrival of a single SiPM and of the average of the two SiPMs have been analysed considering the time difference with t_0 (given by PMs, see Sections 4.2.2 and 3.2.2). The Δt distribution obtained in various configurations has been fitted using a gaussian function (see Figure 4.12(b)). The σ of this distribution is related to the detector time resolution; in the case of the average of the two SiPMs the final time resolution will represent the one of the whole system of the scintillator plus the two SiPMs (plus electronics). The time resolution σ_{bt} of the detector is obtained from the σ of the gaussian fit using the following formula:

$$\sigma_{bt} = \sqrt{\sigma^2 - \sigma^2_{t_0}} \tag{4.6}$$

All the time resolutions reported include the contributions of the detector itself (scintillator and SiPM) and of the whole electronic chain (front-end and readout electronics).
The final results for the cosmic ray setup obtained in the various configurations are reported in Table 4.4. As expected, with increasing fiber length there is a worsening of the time resolution. A time resolution of 84 ± 5 *ps* per single SiPM has been achieved for the direct coupling.

Cosmic rays	Coupling to Scintillator	Voltage (V)	Time resolution (ps)
	Direct	68.5	84 ± 5
	Fibres 10 *cm* long	68.5	125 ± 5
	Fibres 35 *cm* long	68.5	139 ± 6

Table 4.4: Time resolution results for the cosmic ray setup.

In the beam test setup the time resolution versus both the NINO threshold and voltage applied to the SiPMs has been studied. In particular the

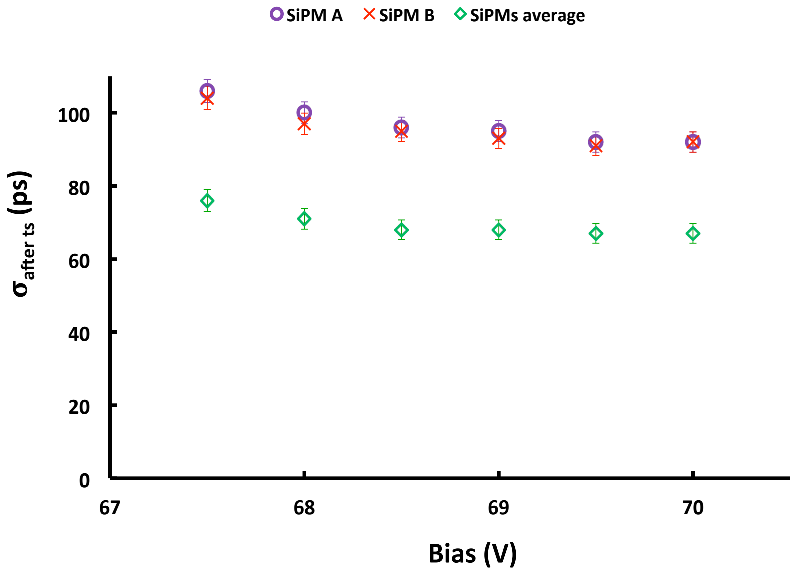

Figure 4.13: Final time resolutions $\sigma_{SiPM\ A,ts}$, $\sigma_{SiPM\ B,ts}$, $\sigma_{SiPMs\ av,ts}$ for the beam test setup after the time slewing correction versus the applied bias voltage.

Beam test	Voltage (V)	Time resolution (ps)
SiPM A	69.5	92 ± 3
SiPM B	69.5	91 ± 3
SiPMs average		67 ± 3

Table 4.5: Time resolution results for the beam test set up.

NINO threshold was changed between $(200-500)$ mV without any significant change. The voltage was modified from 67.5 V to the maximum operation voltage (70 V). The results are reported in Figure 4.13. As expected the time resolution is worst for lower voltage.

In the beam test setup the best time resolution was obtained for a voltage of 69.5 V; in Table 4.5 the results are reported. For the single SiPM a time resolution of 91 ± 3 ps; it should be pointed out that the value is compatible with the cosmic ray results. A final time resolution for the average of about 67 ps has been achieved for the complete detector, comprehensive of the two SiPMs, the scintillator and the whole electronics chain.

Chapter 5

UFSD

Ultra Fast Silicon Detector (UFSD) (see Section 2.8) is a new kind of silicon detector optimized for time measurements; the goal is to reach both excellent space ($\sim 10\ \mu m$) and time resolution ($\sim 10\ ps$). In this way it would be possible to have a 4D detector using only one sensor. This could be of great interest for the next generation of hadron colliders (HL-LHC, FCC). In particular, for the HL-LHC, ATLAS [75], CMS and TOTEM [76] are considering upgraded detectors making use of UFSDs. One of the demanding tasks that needs to be accomplished by UFSDs is to get a radiation hardness of $5 \cdot 10^{15}\ n_{eq}/cm^2$.

The UFSD are LGAD optimised for timing measurements; this technology was proposed and developed by Centro Nacional de Microelectronica (CNM, Spain) [77], and presented the first time in 2014. The first manufactured detector had a thickness of 300 μm; in 2016 a 45 μm thickness design was realised. With this last design, a time resolution of about 34 ps has been achieved for a gain of $\sim$ 20 [63]. The UFSDs were also produced by the Fondazione Bruno Kessler (FBK, Italy) and designed by FBK + INFN [78] (2015); moreover in 2017 first prototypes of UFSDs have been produced also by Hamamatsu Photonics K.K. (HPK, Japan).

In this chapter the results obtained from the study of the time resolution of USFDs are reported. The UFSDs from these three manufacturers have been studied: CNM, FBK and HPK. First a cosmic ray setup has been used to study a CNM detector at the Bologna INFN laboratories. Then, both the HPK and FBK detectors have been studied in a beam test setup, at the H8 test beam at CERN. In particular the HPK UFSDs of two different thicknesses and with different doping concentrations have been studied. The FBK UFSD has been studied with different dopants of the gain layer.

5.1 Detectors used

The CNM UFSD tested (CNM 300) has an active area of $5 \times 5\ mm^2$ and $300\ \mu m$ of thickness. In Figure 5.1(a) a picture of the detector is shown. The gain of the detector depends on the voltage, and for this study a voltage of $800\ V$ was applied, corresponding to a gain of ~ 10.

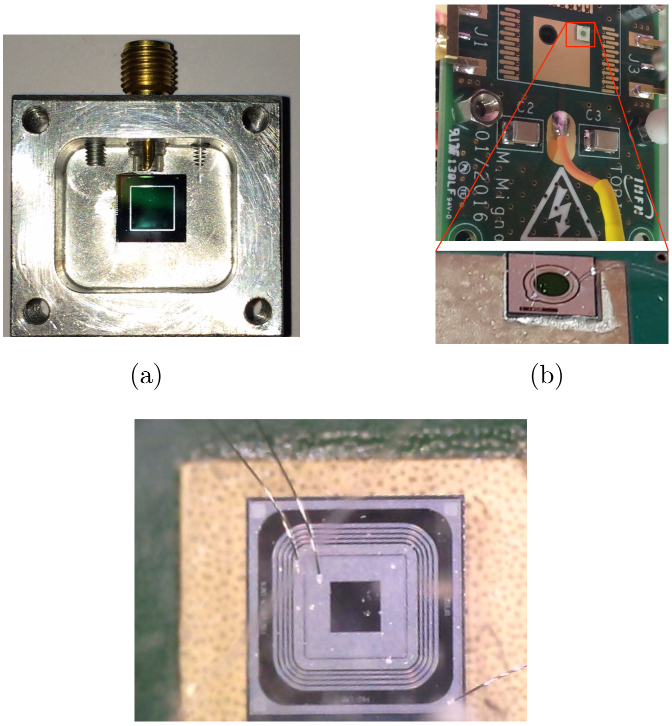

(a) (b)

(c)

Figure 5.1: (a) Picture of the CNM 300 tested; the protective box together with the signal pick-up point are visible. (b) Picture of an HPK detector in the PCB (top) and magnified (bottom). (c) Picture of an FBK detector.

The Hamamatsu tested are circular design detectors of two different thicknesses, with an active area of $0.785\ mm^2$ ($1\ mm$ of diameter); the Hamamatsu realised also four different doping concentrations (gain dose) named A, B, C, D, from lower to higher[1]. At the beginning of 2017 the first measurements on HPK UFSD have been reported at the TREDI 2017 conference [80]. Here the results on time resolution for four detectors (HPK 80C, HPK 80D, HPK

---

[1] The difference between adjacent doping concentrations is a step of about 4% of the value [79].

50C, HPK 50D) of 80 μm and 50 μm thickness are reported. The doping concentrations considered were the type C and D, i.e. the two highest since they are more interesting in terms of radiation hardness (see Section 1.4.1.4). Indeed detectors with a higher initial doping concentration maintain higher acceptor concentration even after irradiation, if compared with those with a lower initial concentration [81].

In Figure 5.1(b) a picture of one of the detectors is reported. For higher doping, the gain is expected to increase at lower voltage.

	Thickness	Active area	Voltage applied	Conc/Diff	Dopant
CNM 300	300 μm	5×5 mm^2	800 V	-	-
HPK 80C	80 μm	0.785 mm^2	$610 - 670$ V	Low	-
HPK 80D	80 μm	0.785 mm^2	$370 - 430$ V	High	-
HPK 50C	50 μm	0.785 mm^2	$370 - 430$ V	Low	-
HPK 50D	50 μm	0.785 mm^2	$250 - 290$ V	High	-
FBK 50W1	50 μm	1×1 mm^2	$240 - 300$ V	Low/Low	Boron
FBK 50W8	50 μm	1×1 mm^2	$260 - 350$ V	High/High	Boron
FBK 50W15	50 μm	1×1 mm^2	$205 - 265$ V	-	Gallium + C

Table 5.1: Summary of the UFSDs main characteristics.

In this work the FBK UFSDs were also studied; in particular in the first half of 2017, FBK realised a production of 50 μm thick UFSDs with different doping concentrations and dopants of the gain layer; in Figure 5.1(c) a picture of an FBK detector is reported. In this work the results on time resolution of three different FBK detectors, with an active area of 1 mm^2, are reported. In particular two detectors (FBK 50W1, FBK 50W8) with a different temperature of diffusion (low and standard) and different doping concentrations with standard gain layer (Boron) have been tested. Both solutions are interesting for radiation hardness; the effect of the doping concentration has been already explained, while to understand that of the temperature of diffusion a brief digression of silicon production has to be done. After the implantation of the doping profile (e.g. of the gain layer) into the silicon, the detector has to go through a thermal diffusion process, called annealing. This step has a twofold fundamental goal: one is to activate the implanted dopants (going from interstitial to substitutional), while the other is to recovery of lattice damages with the diffusion, caused by implantation itself. It must be pointed out that the implantation by itself, before the diffusion, implies a very shallow doping, with a smaller volume than after the high temperature phase. The choice of the temperature of diffusion can be then a tradeoff between

two main effects: lower temperature can lead to a worst damage repairing but the smaller volume obtained results in a higher radiation hardness (see Section 1.4.1.4).
The other detector tested (FBK 50W15) uses a different solution for the dopants of the gain layer, Gallium and a Carbon co-implanation: this is the first working Gallium UFSD production. This configuration was produced to investigate the radiation hardness. Indeed, with irradiation, the gain changes; in particular it is reduced by the acceptor removal mechanism, due to the capture of Boron atoms into interstitials (see Section 1.4.1.4). With Gallium, instead of Boron, the formation of acceptor interstitial during irradiation should be reduced (indeed Gallium is bounded more strongly or rather has a smaller diffusion mobility within the lattice); the Carbon should instead reduce the concentration of the interstitials available, filling itself the interstitials (so no more available for Boron or Gallium).

In Table 5.1 the main characteristics of the used detectors are reported in addition at the applied bias voltage.
An important measurement, to compare the results between different detectors, is the gain. The gain values of the detectors have been measured considering the charge released from a MIP and comparing that with an

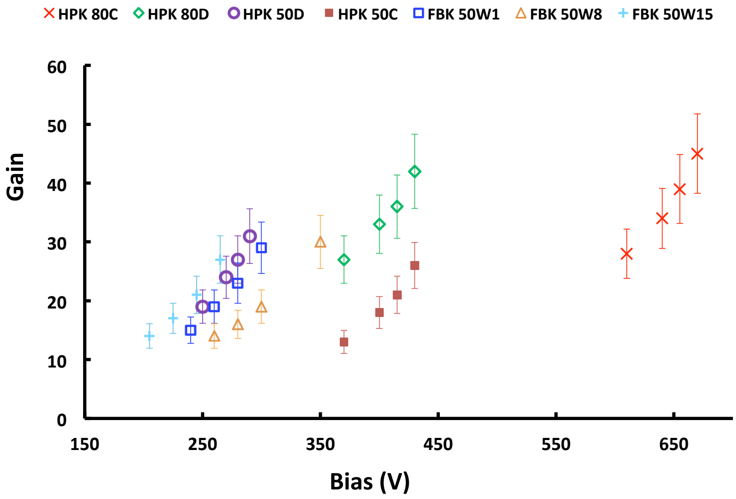

Figure 5.2: Measured gain (see text) versus bias voltage of the three FBK wafer (W) tested: $W1$, $W8$ and $W15$. The errors have been estimated as the 15% of the value, considering the fluctuations between several measurements at the same voltage bias.

equivalent detector (same thickness) but without gain. The gain of FBK UFSDs has been measured using this method (other measurements are reported in [82]); the HPK gain have been calculated in another study and reported in [83]. In Figure 5.2 a plot of the gain versus the bias voltage is reported.

In Figure 5.3 a typical signal recorded by an oscilloscope of an UFSD is shown after an amplification of a factor 100.

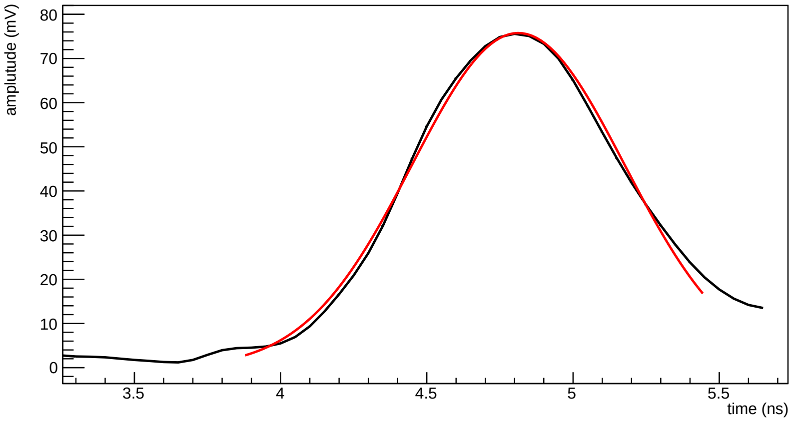

Figure 5.3: HPK 50 μm UFSD signal, readout by an oscilloscope, after an amplification of a factor 100 in a beam test. In red a gaussian fit of the signal.

5.2 Experimental setup and electronics

The detector performances were studied firstly in a cosmic ray setup at Bologna INFN laboratories and then in a beam test setup at CERN. The main goal was to study the time resolution of all the above mentioned UFSDs.

5.2.1 Cosmic Rays setup

To measure the time resolution of the CNM 300 a cosmic rays telescope (Figure 5.4) has been set up. The telescope is constituted of two plastic scintillators $2 \times 2 \times 3$ cm^3 (top and bottom) coupled to SiPMs and of the UFSDs under test (in the middle). The scintillator+SiPMs are used as the

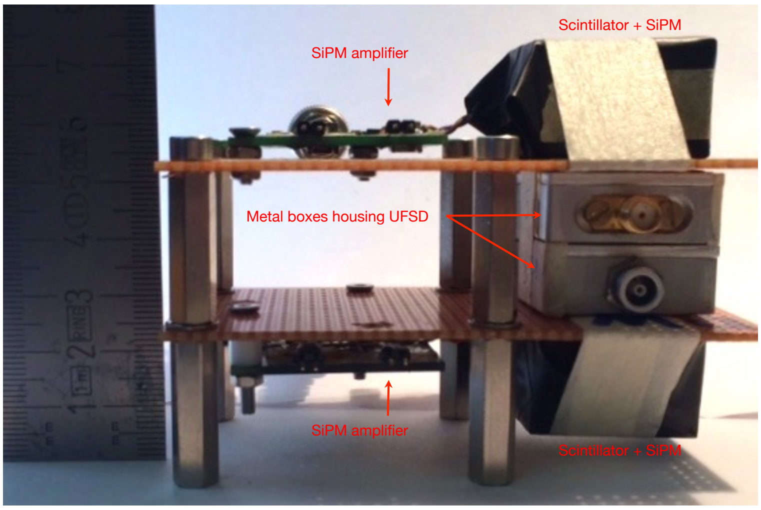

Figure 5.4: Picture of the cosmic ray telescope used to measure the time response of UFSDs.

trigger for the acquisition system and reference (t_0) for the time measurements.

The telescope was then inserted inside a box in order to maintain a constant temperature of $18^o\ C$ through a chiller. This allows to keep constant the UFSD performances; this is of particular importance, due to the long data taking period required using a cosmic ray test (in addition to such a small area detectors).

As front-end electronics two amplifiers Gali52 [84] from MiniCircuits in series have been used, getting a factor 100 of amplification; this huge amplification was necessary because the UFSD signal amplitude is less than one mV (see Fig. 5.3, where the signal was already amplified). In Figure 5.5(a) a picture of the front-end amplifier Gali52 is reported.
As readout electronics the same standard CAMAC modules (TDC and CIA) described in Section 4.2.1 have been used.

5.2.2 Beam test setup

The time resolution of HPK and FBK detectors has been studied in a beam test setup; in particular their performances have been analysed at the H8 test beam line at CERN. The beam was mainly composed of pions of 180 GeV.

In Figure 5.6 a picture of the experimental setup is reported; four layers

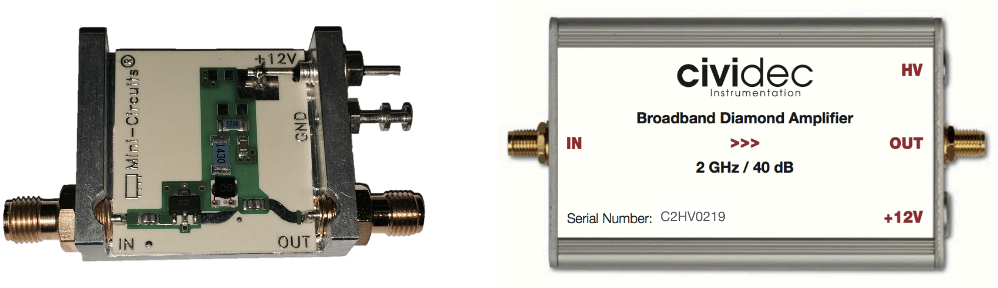

(a) (b)

Figure 5.5: (a) Front-end electronics used in the cosmic ray setup; the Gali52 chip is visible. (b) Front-end electronics used in the beam test setup: a Cividec amplifier.

(L1, L2, L3, L4) of HPK UFSDs, corresponding to the four HPK detectors under test, are visible. The trigger for data acquisition was given by the coincidence of the UFSDs themselves.
For the FBK the same configuration has been used (in this case three layers corresponding to the three detectors) in addition with a CNM detector of 45 μm thickness, for a total of four layers again. Due to a misalignment of the detectors, it was not possible to have a threefold coincidence; then the trigger for data acquisition was a twofold coincidence between CNM45 and one of the FBK detectors. The CNM45 is the one tested in [63] that reached a time resolution of 34 ps and is used as t_0.

As front-end electronics a Cividec broadband amplifier [85] has been used, with an amplification of a factor 100. In Figure 5.5(b) a picture of the amplifier is reported. As readout electronics an Oscilloscope Lecroy 640 Zi [86] has been used; the contribution of the oscilloscope to the measured time resolurtion is totally negligible.

5.3 Results and discussion

In this section the data analysis and the results obtained will be discussed.
In the cosmic ray setup, a preliminary measure using the CNM300 detector has been performed. Due to the very small UFSD active area (5×5 mm^2) combined with the low (w.r.t. beam test) rate of particles, a particularly long data taking was required to reach an adequate statistic. For each event the time and charge collected by the trigger, or rather the SiPMs, are recorded and can be used to select cosmic rays events above background.
For each event the time of arrival and the Time Over Threshold (related to

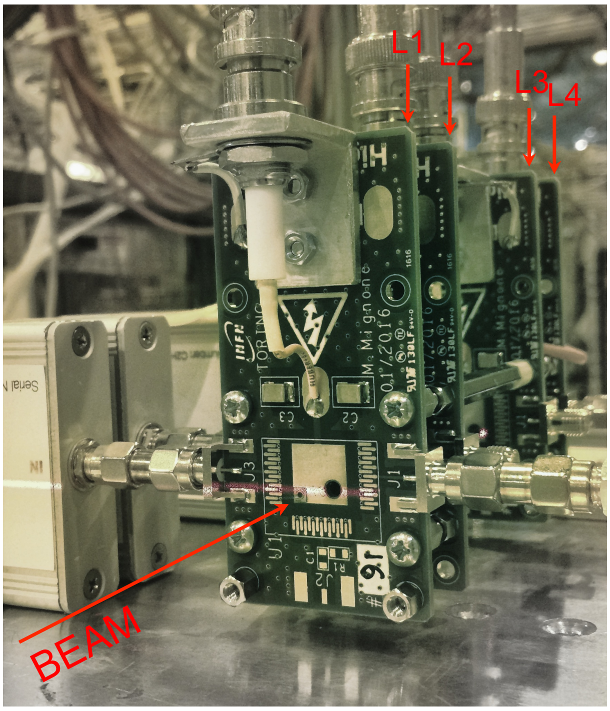

Figure 5.6: Beam test setup; four layers (L1, L2, L3, L4) of HPK UFSDs are visible.

the charge) of the UFSDs were measured. The time measurements have been corrected for the time slewing effect (see Section 1.5.3); in Figure 5.7 two plots regarding the correlation between the charge and time of the UFSD before and after the time slewing correction are shown. Through these corrections an improvement up to 24% of the time resolution has been achieved.

To calculate the time resolution (after the time slewing corrections), the difference of the arrival times of the UFSD signals and the t_0 (given by SiPMs, see previous section) $\Delta t = t_{CNM300} - t_0$ has been considered.

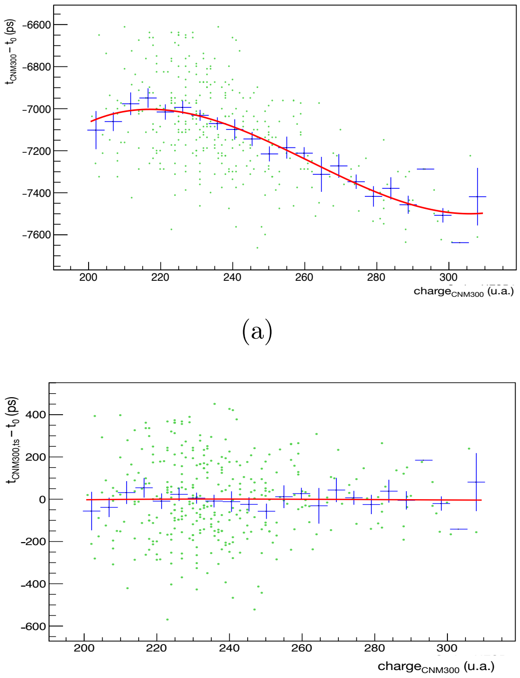

(a)

(b)

Figure 5.7: Correlation between the charge and time of the CNM300 UFSD before (a) and after (b) the time slewing correction (subscript ts); the distribution has been fitted using a third degree polynomial .

The Δt distribution obtained has been fitted using a gaussian function, see Figure 5.8. The σ of this distribution provides the UFSD+SiPM time resolution. The time resolution of the UFSD is obtained from the σ of the fit distribution, using the following formula:

$$\sigma_{CNM300} = \sqrt{\sigma^2 - \sigma_{t_0}^2} \qquad (5.1)$$

where $\sigma_{t_0} = 58\ ps$ is the time resolution of the SiPMs time reference. The final time resolution obtained was $180 \pm 10\ ps$ including the front-end and

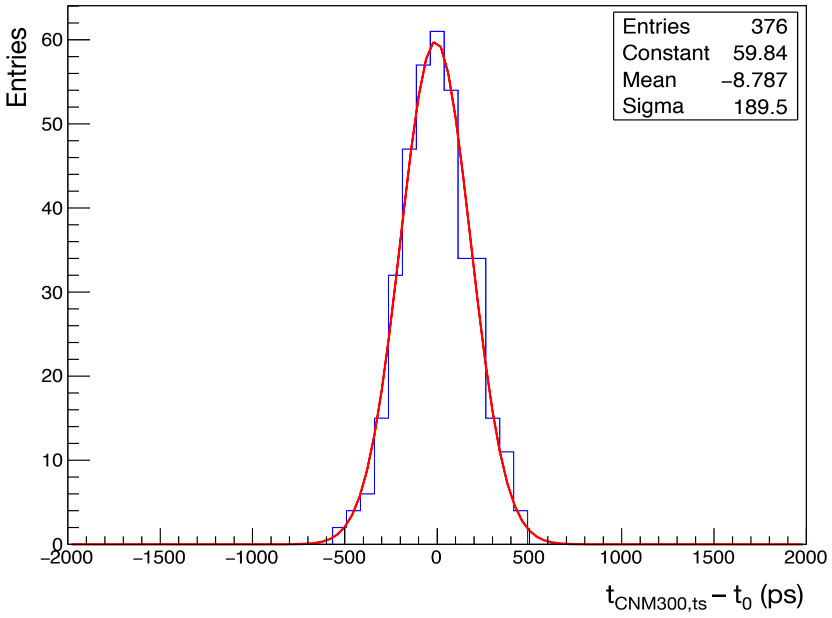

Figure 5.8: Time distribution of the CNM300 UFSD, obtained in the cosmic ray setup with an applied bias voltage of 800 V. In red a gaussian fit.

readout electronics.

In the beam test setup the HPK and FBK detectors have been studied. Thanks to the oscilloscope readout, the full waveform of the signals have been recorded. This allows to get a time resolution closer to the detector intrinsic one; hence, for all the the time difference distribution, a Constant Fraction Discriminator (CFD) technique (see Section 1.5.3) has been applied offline. In this way the time slewing corrections were not necessary. The charge has been considered looking at the amplitude of the signal.
Due to the different experimental setups (see previous section), different approaches to calculate the time resolution have been used. For HPK detectors, several time differences of the arrival times between UFSDs have been considered. Therefore, the final HPK time resolution σ_i, with i=(HPK80C, HPK80D, HPK50C, HPK50D), was:

$$\sigma_i = \sqrt{\frac{\sigma_{ij}^2 + \sigma_{ik}^2 - \sigma_{jk}^2}{2}} \tag{5.2}$$

with $i \neq j \neq k$ and σ_{ij} the time resolution of the time difference distribution between detectors i and j (similarly for σ_{ik}, σ_{jk}). In Figure 5.9(a) the time difference between two HPK detector is shown.
In Figure 5.9(b) a typical charge distribution in the beam test setup is shown; to fit it a convolution of a Gaussian and a Landau was used.

For FBK detectors the difference of the arrival times of the signals and the CNM45 (used as trigger, see previous section) for a $CFD = 25\%$ has been considered; to calculate the final time resolution, Eq.5.1 has been used: in this case $\sigma_{t_0} = \sigma_{CNM45} = 34\ ps$.

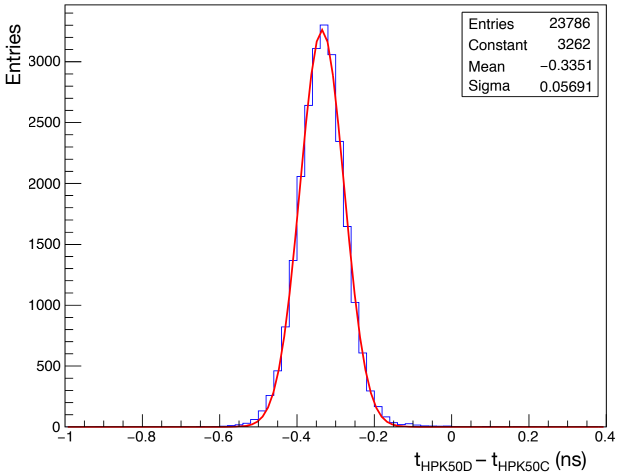

(a)

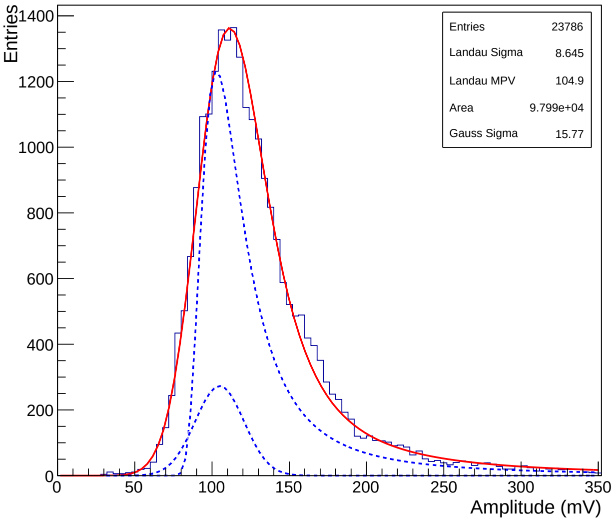

(b)

Figure 5.9: (a) Time difference distribution between two HPK detectors obtained in a beam test setup; the voltage applied was 430 V and 290 V for the HPK50C and HPK50D respectively. (b) Charge distribution obtained for HPK50D in the same configuration. To fit it a convolution of a Gaussian and a Landau was used.

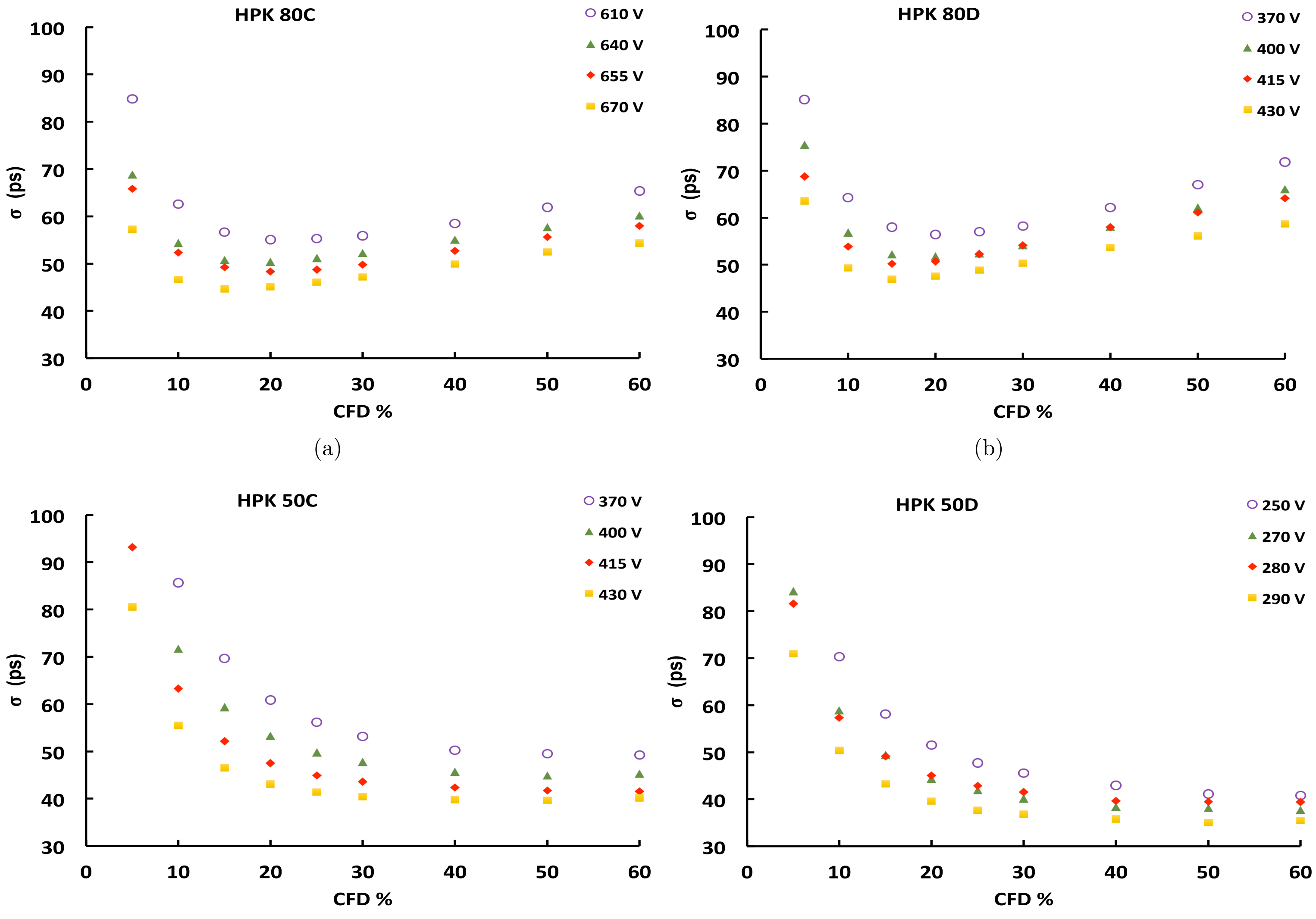

(a) (b) (c) (d)

Figure 5.10: Time resolution versus the Constant Fraction Discriminator (CFD) for several applied bias voltage for the four HPK detectors:(a) HPK80C, (b) HPK80D, (c) HPK50C,(d) HPK50D. The errors have been estimated to be about 6% of the measured value (not reported to obtain a more readable plot).

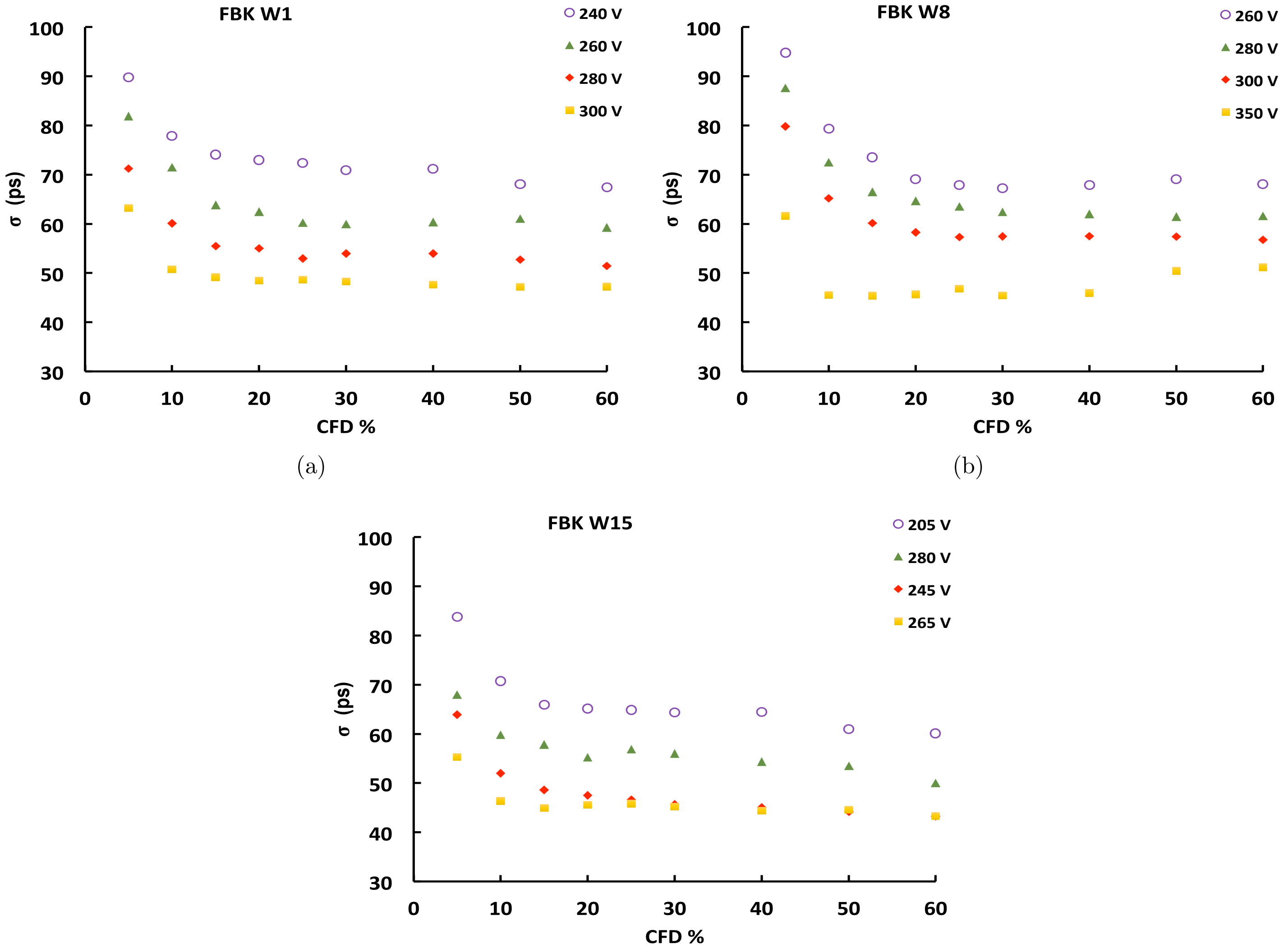

(a)

(b)

(c)

Figure 5.11: Time resolution versus the Constant Fraction Discriminator (CFD) for several applied bias voltage for the three FBK detectors:(a) FBKW1, (b) FBKW8, (c) FBKW15. The errors have been estimated to be about 15% of the measured value (not reported to obtain a more readable plot).

The final time resolution of the HPK and FBK detectors have been studied for several values of the CFD for different applied bias voltage; in Figure 5.10 -5.11 the time resolution versus the CFD for HPK and FBK detectors under test is reported. As expected from Figure 2.33, for low values of the CFD the time resolution is worse, due to the jitter contribution. For higher values of the CFD, from about $(15 - 20)\%$, the behaviour is different, depending on the thickness of the detector (see Fig. 5.10): for the 50 μm thick one, after the improving (reduction) of the resolution, the trend is flat; on the contrary, for the 80 μm thick detector, there is a rising (worsening of time resolution); this is due to the Landau contribution (see Fig.2.33), larger for thicker detectors.

From these plots, both for HPK and FBK detectors, a CFD value has been extracted as the one that minimises the time resolution; therefore, for each detector and each applied bias voltage, one value of time resolution is considered.

Figure 5.12 reports, for the HPK detectors, the trend of the time resolution versus the Landau Most Probable Value (MPV) and bias voltage (for the best CFD value). As expected, for both higher MPV and voltage (i.e. gain), the time resolution improves; moreover it can be noticed a better time resolution for thinner detectors (as expected from Fig.2.32).

Figure 5.13 reports the comparison among the HPK and FBK UFSDs time resolution versus the gain.

All the detectors tested work, with a time resolution better 50 ps, for a gain larger than 25. In particular, for the 80 μm thick HPK sensors, a time resolution of 45 ± 3 ps has been achieved, for a gain of about 45. For the thinner HPK sensors, as expected, an even better time resolution has been reached: 35 ± 2 ps for HPK50D, for a gain of about 31. Anyway the measurements for HPK detectors of same thickness showed results totally comparable, even considering different doping concentration; the time resolution improves with the gain, like a solely sensor.

The results concerning the FBK sensors were obtained with a reduced statistics (see Section 5.2.2); indeed the three detectors results are still compatible, due to larger systematic error. Except for FBKW15, the other two FBK sensors reached a worst time resolution, w.r.t. HPK detectors. A different trend of time resolution versus the gain between the two productions can be noticed: indeed, in the tested range of gains, the improvement with the gain is larger for FBK detectors w.r.t. HPK sensors. Anyway, the best time resolution reached for FBK detectors was 40 ± 7 ps for the FBK 50W15 with a gain of about 27. In Table 5.2 the best time resolutions achieved (which correspond to the higher gain value) for all the seven detectors (4HPK+3FBK)

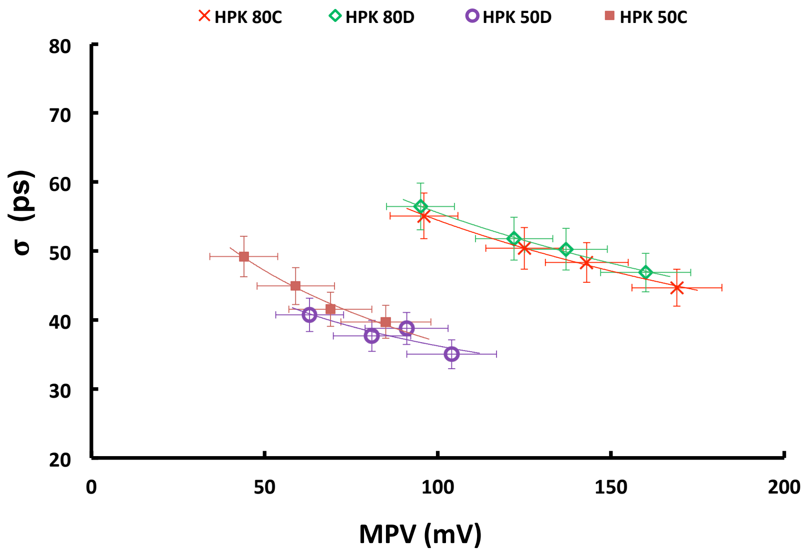

(a)

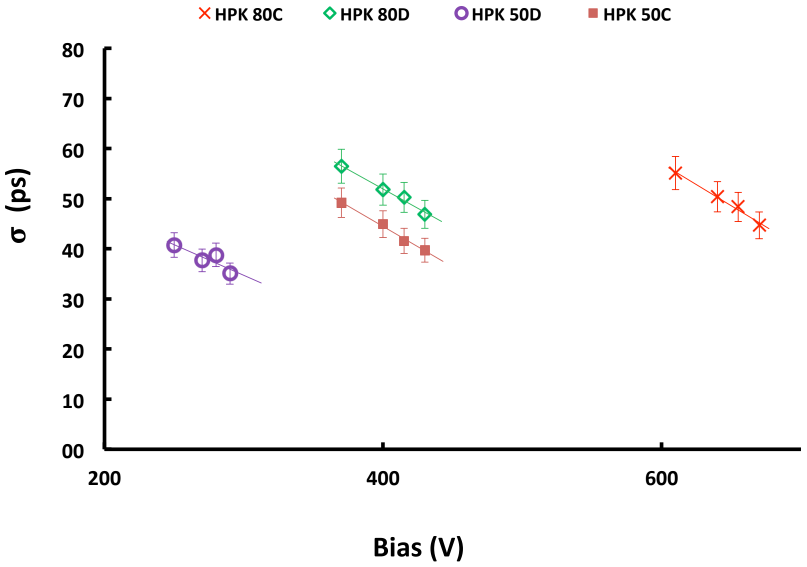

(b)

Figure 5.12: Time resolution of HPK UFSDs versus the Most Probable Value (a) and the bias applied bias voltage (b).

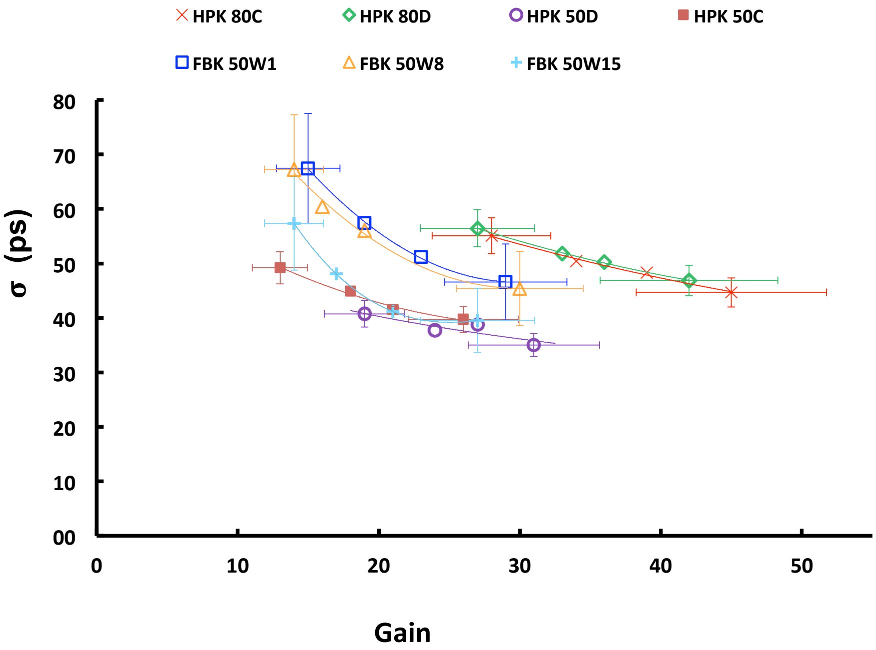

Figure 5.13: Time resolution of HPK and FBK detectors versus the gain. The error bars have been reported only for the smaller and bigger gain value for each detector to obtain a more readable plot. Anyway the errors for the time resolution of HPK and FBK detectors have been estimated as 6% and 15% of the value respectively, while the error on the gain has been estimated as the 15% of the value.

are reported.

Beam test	Gain	Time resolution (ps)
HPK 80C	45 ± 7	45 ± 3
HPK 80D	42 ± 6	47 ± 3
HPK 50C	26 ± 4	40 ± 3
HPK 50D	31 ± 5	35 ± 2
FBK 50W1	29 ± 4	46 ± 7
FBK 50W8	30 ± 5	44 ± 7
FBK 50W15	27 ± 4	40 ± 7

Table 5.2: Time resolution results for the beam test set up.

In conclusion, the first beam test results on time resolution of the first production of Hamamatsu and FBK of 50 μm (with several solutions for radiation hardness) UFSDs have been studied; both the productions are perfectly working, see Table 5.2 for the time resolutions obtained. It should be pointed out that in particular the Gallium FBK production are the first working Gallium UFSDs produced.
Moreover the results obtained for CNM, HPK and FBK can be compared with the simulations, as reported in Figure 5.14. The trend as a function of the thickness is very similar in data (beam tests and cosmic rays) and simulations. A huge improvement between 3×3 mm^2 and 1×1 mm^2 is observed, due to the lower capacitance. Thanks to a thinner design (50 μm), a resolution of about 35 ps is obtained both in the measured FBK and HPK prototypes and in the simulation.

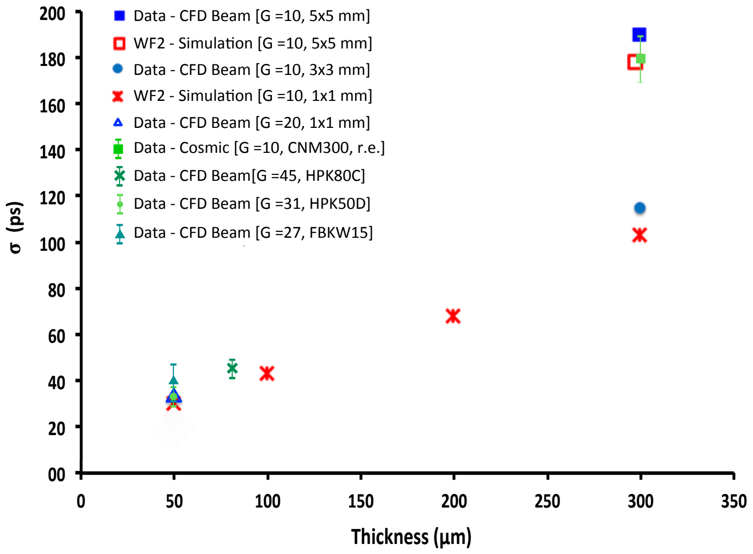

Figure 5.14: Time resolution versus the UFSD thickness; in green some of the results obtained in this work. In red and blu the results obtained with simulation (WF2 [62]) and earlier beam tests [63] respectively. For each value the respective gain (G) is reported. In the caption: r.e.=readout electronics included, CFD Beam = Data from beam test using a Constant Fraction Discriminator technique.

Chapter 6

Conclusions

In this thesis an *R&D* and optimisation of time resolution for various detectors have been performed. Indeed high-resolution timing detectors are ubiquitous in both particle and medical physics. Moreover for the next generation of colliders, a time resolution of tens of picoseconds would be necessary; indeed the time information associated to each track would provide a 4-D tracker.

The *R&D* regarded detectors based on different technologies: MRPC, SiPM and on a new prototype of silicon detector, the UFSD. Moreover an optimisation based on data analysis has been carried out on existing and fully operational MRPCs, the ALICE-TOF MRPCs.

In this study, factors that can lead to a spoiling of the TOF time resolution have been studied, focusing on the effect of the particle impinging position on the detector. In particular two main cases have been studied and corrected, a single event case (corrected for time walk) and a double event case (corrected with clusterization), where the signal was induced on more than one readout pad. The results have shown, with the actual TOF setup, no relevant improvement concerning the time walk corrections (confirming a time resolution of 57 *ps*); instead with the clusterization, an improvement on time resolution from 65 ± 1 *ps* to 58 ± 1 *ps* (same time resolution of single event case) has been achieved; with the last correction, for the double hit cases, in addition to get a single improved time resolution, a space information, independent from the tracking, was also achieved and optimised. Moreover, the study of these effects, will lead to an improvement of the Monte Carlo simulations of the TOF signals.

One of the MRPC *R&D* concentrated on the designing and building of a new chamber prototype (MRPC(20/180)) with the aim of improving the already excellent time resolution, using an increased number of thinner gas gaps. The results have shown an efficiency of about 100%, demonstrating the chamber

functionality. The time resolution achieved was 53 ± 1 *ps*. Anyway this value was totally dominated by the readout electronics, indeed the next step would be to test the chamber using an oscilloscope as readout; the expected time resolution is less than 20 *ps*.
For the next generation of colliders, another fundamental requirement for the detectors is the capability of the sensor to withstand the very high rate of particles; therefore, two chambers (MRPC(4/300) and MRPC(5/250)) have been built for this purpose. The modus operandi consisted in an innovative way to reduce the electrode resistivity, maintaining the other MRPC characteristics properties; a painted layer has been added to the surfaces of the inner glass sheets, with two different designs (on both side of the glass for MRPC(4/300), on only one side for MRPC(5/250)). Both chambers have shown (at normal rate) a time resolution of about 80 *ps*. The results regarding the MRPC(4/300) have shown no improvement, w.r.t. a standard chamber. On the contrary, MRPC(5/250) has shown a lower degradation of efficiency with increasing rate, w.r.t. a standard chamber, demonstrating the validity of the method. All the chambers have been tested in a beam test setup, at the T10 beam line at CERN. These promising results deserve further optimisation of the proposed technique.
The *R&D* concerning the SiPM has been performed both in a cosmic ray setup, in the Bologna INFN laboratories, and in a beam test setup, at the T10 beam line at CERN. The time resolution of the SiPM coupled to a plastic scintillator has been studied; different ways of coupling to the scintillator have been also used, to study the time resolution degradation going from a direct coupling to a coupling by means of optical fibers. The results have shown a time resolution of 139 *ps* and 125 *ps* in the cosmic ray setup for a coupling by means of fibers of different lengths, 35 *cm* and 10 *cm* respectively, while a time resolution of about 90 *ps* for the direct coupling, both in cosmic and beam setup, has been reached. Moreover a final interesting time resolution of 67 ± 3 *ps* has been achieved, in a beam test setup, with two SiPM coupled to the same plastic scintillator. All the results are comprehensive of the full electronic chain, from the front-end to the readout electronics.
The UFSD *R&D* was again focused on time resolution; the study has been performed both in a cosmic ray setup, in the Bologna INFN laboratories, and in a beam test setup, at the H8 beam line at CERN. Detectors with several thickness values, 300 μm, 80 μm and 50 μm have been tested, from different manufacturers: CNM, Hamamatsu(HPK) and FBK. The tested detectors were also designed with different doping concentrations and dopants of the gain layer (standard Boron, Gallium, added Carbon); the aim of these kinds of UFSD is to reach the challenging radiation hardness that would be needed for future colliders. A total of 8 different UFSDs have been studied.

The CNM300 (300 μm thick) has achieved a time resolution of 180 ± 10 ps in the cosmic ray setup, totally compatible with data from beam test and simulations. A much more interesting time resolution has been achieved for the other detectors, thanks to a thinner design: for the HPK 80C (80 μm) and the HPK 50D (50 μm) a time resolution of 45 ± 3 ps (comparable with HPK 80D) and 35 ± 2 ps (comparable with FBK 50W15) have been achieved. Moreover, as a side remark, the results reported in this thesis regarded the first beam test results on time resolution of the first production of Hamamatsu and FBK of 50 μm (with several solutions for radiation hardness); it should be also pointed out that in particular the Gallium FBK production are the first working Gallium UFSDs produced and tested.

All these detectors can then be a candidate for the next generation of colliders. Their use will depend on the choice of the technology, depending on the needs: gaseous detectors, scintillators coupled to SIPMs and silicon detectors, can all be important to build an up to date experiment in particle physics. Anyway, semiconductor detectors probably perform better very close to the interaction region, where a high segmentation is required for a high space resolution. But at large radius, where large areas have to be covered, it is unrealistic to use anything other than gaseous detectors or scintillators coupled to SiPMs. In the intermediate region all the technologies are competitive, depending on the requirements.
Figure 6.1 summarises the results obtained in the present thesis on time resolution for the various detector technologies.

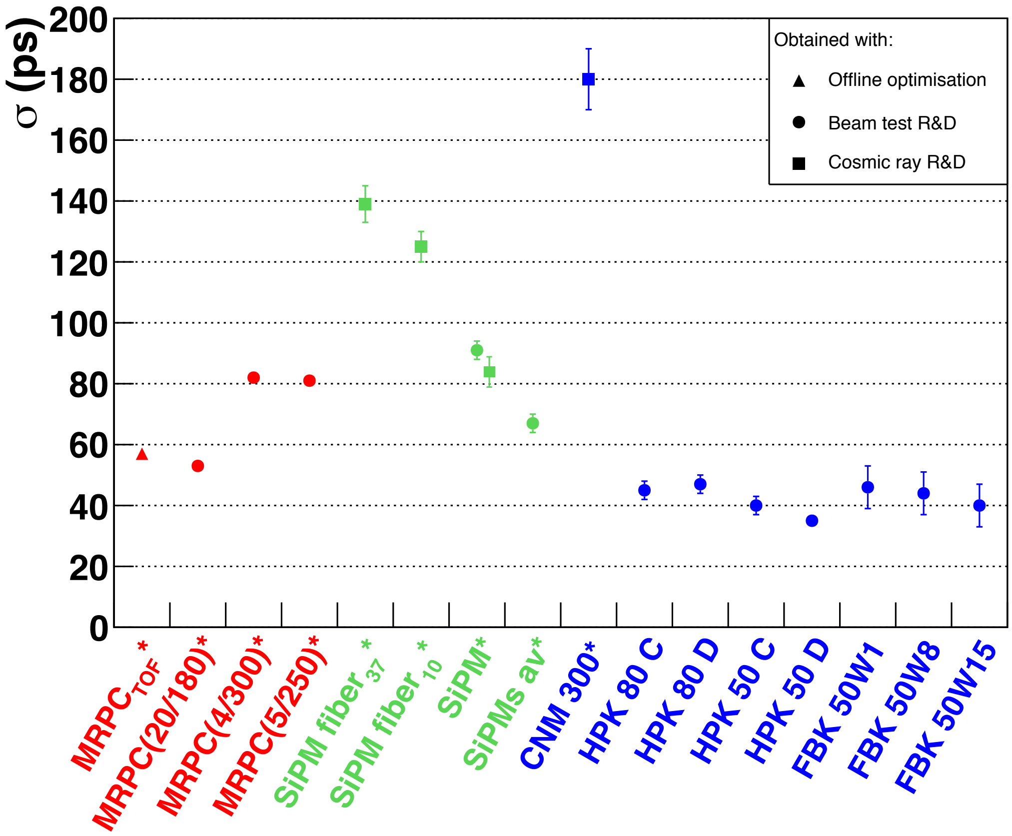

Figure 6.1: Summary of the results on time resolution obtained for various detector technologies. Where not visible, the error is within the symbol size. (*=including the readout electronic board jitter)

Bibliography

[1] W. R. Leo, *Techniques for nuclear and particle physics experiments.* Springer-Verlag, 1994.

[2] **Particle Data Group** Collaboration, C. Patrignani *et al.*, "Review of Particle Physics," *Chin. Phys.* **C40** no. 10, (2016) 100001.

[3] G. F. Knoll, *Radiation Detection and Measurement, 3rd ed.* John Wiley and Sons, New York, 2000. `http://www.slac.stanford.edu/spires/find/books/www?cl=QCD915:K55:2000`.

[4] A. Bettini, *Introduction to elementary particle physics.* Cambridge, UK: Univ. Pr. (2008) 431 p, 2008. `http://www.cambridge.org/catalogue/catalogue.asp?isbn=9780521880213`.

[5] C. Grupen and B. Schwartz, *Particle detectors.* Cambridge, UK: Cambridge Univ. Pr. (2008) 651 p, 2008.

[6] U. Fano, "Ionization Yield of Radiations. 2. The Fluctuations of the Number of Ions," *Phys. Rev.* **72** (1947) 26–29.

[7] **ALICE** Collaboration, A. Alici, "The MRPC-based ALICE Time-Of-Flight detector: status and performance," *Nucl. Instrum. Meth.* **A706** (2013) 29–32, `arXiv:1203.5976 [physics.ins-det]`.

[8] F. Hartmann, *Evolution of silicon sensor technology in particle physics.* Springer tracts in modern physics. Springer, Berlin, 2009. `https://cds.cern.ch/record/1100830`.

[9] W. Shockley, "Currents to conductors induced by a moving point charge," *Journal of Applied Physics* **9** no. 10, (1938) 635–636. `http://dx.doi.org/10.1063/1.1710367`.

[10] S. Ramo, "Currents induced by electron motion," *Proc. Ire.* **27** (1939) 584–585.

[11] Z. He, "Review of the Shockley-Ramo theorem and its application in semiconductor gamma-ray detectors," *Nuclear Instruments and Methods in Physics Research Section A* **463** no. 1, (2001) 250 – 267. `http://www.sciencedirect.com/science/article/pii/S0168900201002236`.

[12] J. C. W. Song and L. S. Levitov, "Shockley-ramo theorem and long-range photocurrent response in gapless materials," *Phys. Rev. B* **90** (Aug, 2014) 075415. `https://link.aps.org/doi/10.1103/PhysRevB.90.075415`.

[13] A. Alberigi Quaranta, M. Martini, and G. Ottaviani, "The pulse shape and the timing problem in solid state detectors - a review paper," *IEEE Trans. Nucl. Sci.* **16N2** (1969) 35–61.

[14] C. Grupen and I. Buvat, *Handbook of particle detection and imaging, vol. 1 and+ vol.2*. Springer, Berlin, Germany, 2012. `http://www.springer.com/978-3-642-13270-4`.

[15] H. Spieler, *Semiconductor Detector Systems*, vol. v.12 of *Semiconductor Science and Technology*. Oxford University Press, Oxford, 2005. `http://www.oup.co.uk/isbn/0-19-852784-5`.

[16] H. F. W. Sadrozinski, A. Seiden, and N. Cartiglia, "4-Dimensional Tracking with Ultra-Fast Silicon Detectors, 2017," `arXiv:1704.08666 [physics.ins-det]`.

[17] P. Jarron, E. Garutti, M. Goettlich, H. Hillemanns, P. Lecoq, W. Shen, H. C. Schultz-Coulon, and C. Williams, "Time based readout of a silicon photomultiplier (sipm) for time of flight positron emission tomography (tof-pet), 2010,".

[18] `https://www.google.it/search?client=firefox-b-ab&dcr=0&q=carnesecchi+sipm+tesi&spell=1&sa=X&ved=0ahUKEwjji7XNwIXYAhXFaxQKHb98BDIQvwUIJCgA&biw=1356&bih=785`. Thesis, 2014.

[19] F. Sauli, "Gaseous Radiation Detectors," *Camb. Monogr. Part. Phys. Nucl. Phys. Cosmol.* **36** (2014) pp.1–497.

[20] J. W. Keuffel, "Parallel-Plate Counters," *Review of Scientific Instruments* **20** no. 3, (1949) 202–208. `http://dx.doi.org/10.1063/1.1741489`.

[21] R. Santonico and R. Cardarelli, “Development of resistive plate counters,” *Nuclear Instruments and Methods in Physics Research* **187** no. 2, (1981) 377 – 380. `http://www.sciencedirect.com/science/article/pii/0029554X81903633`.

[22] E. Cerron Zeballos, I. Crotty, D. Hatzifotiadou, J. Lamas Valverde, S. Neupane, M. C. S. Williams, and A. Zichichi, “A New type of resistive plate chamber: The Multigap RPC,” *Nucl. Instrum. Meth.* **A374** (1996) 132–136.

[23] **ALICE** Collaboration, G. Dellacasa *et al.*, “ALICE technical design report of the time-of-flight system (TOF),”.

[24] W. Riegler, C. Lippmann, and R. Veenhof, “Detector physics and simulation of resistive plate chambers,” *Nuclear Instruments and Methods in Physics Research Section A* **500** no. 1, (2003) 144 – 162. `http://www.sciencedirect.com/science/article/pii/S0168900203003371`. NIMA Vol 500.

[25] M. C. S. Williams, “Space-charge limitation of avalanche growth in narrow-gap resistive plate chambers,” *Nucl. Instrum. Meth.* **A525** (2004) 168–172.

[26] K. Doroud, H. Afarideh, D. Hatzifotiadou, J. Rahighi, M. C. S. Williams, and A. Zichichi, “Recombination: An important effect in multigap resistive plate chambers,” *Nucl. Instrum. Meth.* **A610** (2009) 649–653.

[27] A. Arefiev *et al.*, “Parallel Plate Chambers, a fast detector for supercollider experiments,” *Nucl. Phys. B, Proc. Suppl.* **32** (1992) 223–229. 8 p. `https://cds.cern.ch/record/242884`.

[28] C. Lippmann, W. Riegler, and N. Sharma, “Rate effects in resistive plate chambers,” *Nucl. Phys. B, Proc. Suppl.* **158** (2006) 127–130.

[29] M. Abbrescia, “The dynamic behaviour of Resistive Plate Chambers,” *Nucl. Instrum. Meth.* **A533** (2004) 7–10.

[30] D.Gonzalez-Diaz, P.Fonte, J.A.Garzon, and A.Mangiarotti, “An analytical description of rate effects in timing rpcs,” *Nuclear Physics B - Proceedings Supplements* **158** (2006) 111 – 117. `http://www.sciencedirect.com/science/article/pii/S092056320600435X`. Proceedings of the 8th International Workshop on Resistive Plate Chambers and Related Detectors.

[31] C. Lippmann and W. Riegler, "Space charge effects in resistive plate chambers," *Nucl. Instrum. Meth.* **A517** (2004) 54–76.

[32] **ALICE** Collaboration, K. Aamodt *et al.*, "The ALICE experiment at the CERN LHC," *JINST* **3** (2008) S08002.

[33] **ALICE** Collaboration, B. B. Abelev *et al.*, "Performance of the ALICE Experiment at the CERN LHC," *Int. J. Mod. Phys.* **A29** (2014) 1430044, `arXiv:1402.4476 [nucl-ex]`.

[34] L. Cifarelli, R. Nania, F. Noferini, E. Scapparone, and A. Zichichi, "Insights from the ALICE quark-gluon coloured world at the LHC," *Riv. Nuovo Cim.* **39** no. 10, (2016) 1.

[35] L. Evans and P. Bryant, "LHC Machine," *JINST* **3** (2008) S08001.

[36] F. Karsch, "Lattice QCD at high temperature and the QGP," *AIP Conf. Proc.* **842** (2006) 20–28, `arXiv:hep-lat/0601013 [hep-lat]`. [,20(2006)].

[37] **ALICE** Collaboration, J. Adam *et al.*, "Enhanced production of multi-strange hadrons in high-multiplicity proton-proton collisions," *Nature Phys.* **13** (2017) 535–539, `arXiv:1606.07424 [nucl-ex]`.

[38] **ALICE** Collaboration, P. Cortese *et al.*, "ALICE: Addendum to the technical design report of the time of flight system (TOF),".

[39] A. Akindinov *et al.*, "Performance of the ALICE Time-Of-Flight detector at the LHC," *Eur. Phys. J. Plus* **128** (2013) 44.

[40] M. C. S. Williams, "Particle identification using time of flight," *J. Phys.* **G39** (2012) 123001.

[41] A. Akindinov *et al.*, "The ALICE Time-Of-Flight system: Construction, assembly and quality tests," *Nuovo Cim.* **B124** (2009) 235–253.

[42] **ALICE** Collaboration, J. Adam *et al.*, "Determination of the event collision time with the ALICE detector at the LHC," *Eur. Phys. J. Plus* **132** no. 2, (2017) 99, `arXiv:1610.03055 [physics.ins-det]`.

[43] F. Anghinolfi, P. Jarron, A. N. Martemyanov, E. Usenko, H. Wenninger, M. C. S. Williams, and A. Zichichi, "NINO: An ultra-fast and low-power front-end amplifier/discriminator ASIC designed for the multigap resistive plate chamber," *Nucl. Instrum. Meth.* **A533** (2004) 183–187.

[44] F. Anghinolfi, P. Jarron, F. Krummenacher, E. Usenko, and M. C. S. Williams, "NINO: An ultrafast low-power front-end amplifier discriminator for the time-of-flight detector in the ALICE experiment," *IEEE Trans. Nucl. Sci.* **51** (2004) 1974–1978.

[45] `http://tdc.web.cern.ch/TDC/hptdc/docs/hptdc_manual_ver2.2.pdf`.

[46] G. Lutz, *Semiconductor Radiation Detectors: Device Physics*. Springer, New York, 1999. `http://www-spires.fnal.gov/spires/find/books/www?cl=QC787.C6L88::1999`.

[47] W. Maes, K. D. Meyer, and R. V. Overstraeten, "Impact ionization in silicon: A review and update," *Solid-State Electronics* **33** no. 6, (1990) 705 – 718. `http://www.sciencedirect.com/science/article/pii/003811019090183F`.

[48] M. Mandurrino *et al.*, "Numerical simulation of charge multiplication in Ultra-Fast Silicon Detectors and comparison with experimental data ,". `https://www.eventclass.org/contxt_ieee2017/online-program`. EEE NSS MIC RTSD 2017 conference.

[49] A. Spinelli and A. L. Lacaita, "Physics and numerical simulation of single photon avalanche diodes," *IEEE Transactions on Electron Devices* **44** no. 11, (Nov, 1997) 1931–1943.

[50] P. Buzhan *et al.*, "Silicon photomultiplier and its possible applications," *Nucl. Instrum. Meth.* **A504** (2003) 48–52.

[51] S. Cova, M. Ghioni, A. Lotito, I. Rech, and F. Zappa, "Evolution and prospects for single-photon avalanche diodes and quenching circuits," *Journal of Modern Optics* **51** no. 9-10, (2004) 1267–1288. `http://www.tandfonline.com/doi/abs/10.1080/09500340408235272`.

[52] V. Golovin and V. Savaliev, "Novel type of avalanche photodetector with geiger mode operation," *Nuclear Instruments and Methods in Physics Research Section A* **518** (2004) 560 – 564.

[53] D. Renker, "Geiger-mode avalanche photodiodes, history, properties and problems," *Nuclear Instruments and Methods in Physics Research Section A* **567** no. 1, (2006) 48 – 56. `http://www.sciencedirect.com/science/article/pii/S0168900206008680`. Proceedings of the 4th International Conference on New Developments in Photodetection.

[54] N. Otte, “The Silicon Photomultiplier: A New Device for High Energy Physics, Astroparticle Physics, Industrial and Medical Applications,” *eConf* **C0604032** (2006) 0018.

[55] D. Renker and E. Lorenz, “Advances in solid state photon detectors,” *JINST* **4** (2009) P04004.

[56] R. Pagano, D. Corso, S. Lombardo, G. Valvo, D. N. Sanfilippo, G. Fallica, and S. Libertino, “Dark current in silicon photomultiplier pixels: Data and model,” *IEEE Transactions on Electron Devices* **59** no. 9, (Sept, 2012) 2410–2416.

[57] `https://www.hamamatsu.com/us/en/community/optical_sensors/articles/physics_and_operation_of_mppc/index.html`.

[58] H. Sadrozinski *et al.*, “Sensors for ultra-fast silicon detectors,” *Nuclear Instruments and Methods in Physics Research Section A* **765** (2014) 7 – 11. `http://www.sciencedirect.com/science/article/pii/S0168900214005051`.

[59] N. Cartiglia *et al.*, “Design optimization of ultra-fast silicon detectors,” *Nucl. Instrum. Meth.* **A796** (2015) 141–148.

[60] H. Sadrozinski *et al.*, “Ultra-fast silicon detectors (UFSD),” *Nuclear Instruments and Methods in Physics Research Section A* **831** (2016) 18 – 23. `http://www.sciencedirect.com/science/article/pii/S0168900216301279`.

[61] N. Cartiglia *et al.*, “Tracking in 4 dimensions,” *Nucl. Instrum. Meth.* **A845** (2017) 47–51.

[62] `http://personalpages.to.infn.it/~cartigli/Weightfield2/Main.html`.

[63] N. Cartiglia *et al.*, “Beam test results of a 16 ps timing system based on ultra-fast silicon detectors,” *Nucl. Instrum. Meth.* **A850** (2017) 83–88, `arXiv:1608.08681 [physics.ins-det]`.

[64] `http://cds.cern.ch/record/2116337`.

[65] `https://cds.cern.ch/record/2110736?ln=it`.

[66] A. Akindinov *et al.*, “Latest results on the performance of the multigap resistive plate chamber used for the alice tof,” *Nuclear Instruments and Methods in Physics Research Section A: Accelerators, Spectrometers,*

Detectors and Associated Equipment **533** no. 1, (2004) 74 – 78. http://www.sciencedirect.com/science/article/pii/S0168900204014081. Proceedings of the Seventh International Workshop on Resistive Plate Chambers and Related Detectors.

[67] S. An and all, "A 20ps timing device – A Multigap Resistive Plate Chamber with 24 gas gaps," *Nuclear Instruments and Methods in Physics Research Section A: Accelerators, Spectrometers, Detectors and Associated Equipment* **594** no. 1, (2008) 39 – 43. http://www.sciencedirect.com/science/article/pii/S0168900208008619.

[68] I. Deppner *et al.*, "The cbm time-of-flight wall," *Nuclear Instruments and Methods in Physics Research Section A: Accelerators, Spectrometers, Detectors and Associated Equipment* **661** no. Supplement 1, (2012) S121 – S124. http://www.sciencedirect.com/science/article/pii/S0168900210021996. X. Workshop on Resistive Plate Chambers and Related Detectors (RPC 2010).

[69] R. Forster *et al.*, "Study of the counting rate capability of mrpc detectors built with soda lime glass," *Nuclear Instruments and Methods in Physics Research Section A: Accelerators, Spectrometers, Detectors and Associated Equipment* **830** no. Supplement C, (2016) 182 – 190. http://www.sciencedirect.com/science/article/pii/S0168900216304739.

[70] https://www.google.it/url?sa=t&rct=j&q=&esrc=s&source=web&cd=4&cad=rja&uact=8&ved=0ahUKEwi89PLNkbDXAhWB1hoKHXxzCKoQFgg6MAM&url=https%3A%2F%2Fseltokphotonics.com%2Fupload%2Fiblock%2F118%2F1186141f87bc6da48efe2c465195e38d.pdf&usg=AOvVaw2vrYK_lzvHRcQ_OnTl1MeP.

[71] https://www.google.it/url?sa=t&rct=j&q=&esrc=s&source=web&cd=1&cad=rja&uact=8&ved=0ahUKEwju--TFk7DXAhWHvBoKHZkBCRAQFggpMAA&url=http%3A%2F%2Fwww.crystals.saint-gobain.com%2Fsites%2Fimdf.crystals.com%2Ffiles%2Fdocuments%2Fsgc-bc418-420-422-data-sheet_69699.pdf&usg=AOvVaw38W-Fq4XjcXsiGekwHmFPc.

[72] http://www.crystals.saint-gobain.com/products/scintillating-fiber.

[73] V. Chmill *et al.*, “On the characterisation of SiPMs from pulse-height spectra,” *Nucl. Instrum. Meth.* **A854** (2017) 70–81, `arXiv:1609.01181 [physics.ins-det]`.

[74] `http://www.caen.it/servlet/SearchLibraryByType?type=Manuals`.

[75] D. Zerwas, “Ecfa, high luminosity lhc experiments workshop, 2016,”. `https://indico.cern.ch/event/524795/contributions/2237331/attachments/1349507/2036492/161006_AixLesBains.pdf`.

[76] C. Royon and N. Cartiglia, “The AFP and CT-PPS projects,” *Int. J. Mod. Phys.* **A29** no. 28, (2014) 1446017, `arXiv:1503.04632 [physics.ins-det]`.

[77] G. Pellegrini *et al.*, “Technology developments and first measurements of low gain avalanche detectors (lgad) for high energy physics applications,” *Nuclear Instruments and Methods in Physics Research Section A: Accelerators, Spectrometers, Detectors and Associated Equipment* **765** no. Supplement C, (2014) 12 – 16. `http://www.sciencedirect.com/science/article/pii/S0168900214007128`.

[78] G.-F. D. Betta *et al.*, “Design and tcad simulation of double-sided pixelated low gain avalanche detectors,” *Nuclear Instruments and Methods in Physics Research Section A: Accelerators, Spectrometers, Detectors and Associated Equipment* **796** no. Supplement C, (2015) 154 – 157. `http://www.sciencedirect.com/science/article/pii/S0168900215003551`.

[79] `https://drive.google.com/drive/folders/0ByskYealR9x7bFY1ZS1pZW9SRWs`.

[80] `http://tredi2017.fbk.eu/`.

[81] J. Lange *et al.*, “Gain and time resolution of 45 μm thin Low Gain Avalanche Detectors before and after irradiation up to a fluence of 10^{15} n_{eq}/cm^2,” *JINST* **12** no. 05, (2017) P05003, `arXiv:1703.09004 [physics.ins-det]`.

[82] M. Ferrero *et al.*, “Developments in the Production of Ultra-Fast Silicon Detectors,”. `https://www.eventclass.org/contxt_ieee2017/online-program`. Presentation at the IEEE NSS MIC RTSD 2017 conference.

[83] Z. Galloway *et al.*, “Properties of HPK UFSD after neutron irradiation up to 6e15 n/cm2,” `arXiv:1707.04961 [physics.ins-det]`.

[84] `https://www.google.it/url?sa=t&rct=j&q=&esrc=s&source=web&cd=1&ved=0ahUKEwjj-5aH58vXAhXH5xoKHTP7DNcQFggmMAA&url=https%3A%2F%2Fwww.minicircuits.com%2Fpdfs%2FGALI-52%2B.pdf&usg=AOvVaw3q5PKCVGA-3uxZySYIwiJv`.

[85] `https://www.google.it/url?sa=t&rct=j&q=&esrc=s&source=web&cd=1&ved=0ahUKEwii1bCgv8_XAhVRyKQKHYVHDloQFgg1MAA&url=https%3A%2F%2Fcividec.at%2Findex.php%3Fmodule%3Dpublic_action.act_download_PIS%26id%3D33%26formcheck%3D72aSNeFJt9m5&usg=AOvVaw0hRE_PKQ2IqhUpg2hbdq86`.

[86] `http://teledynelecroy.com/oscilloscope/oscilloscopemodel.aspx?modelid=4778`.

Acknowledgement

I would like to thank the people I have collaborated with for my Ph.D thesis. My gratitude goes to my Supervisor and Co-supervisor Professor G. Scioli and Dr. R. Nania, and my unofficial Co-supervisor Professor M. Basile, for their continuous support during all the period of my Ph.D.
I would also like to thank D. Cavazza, with whom I spent most of the time in the INFN Bologna laboratories, and Dr. F. Noferini, for his precious collaboration.
Moreover, I am grateful to the Bologna ALICE TOF group as a whole and the Centro Fermi; in particular I am grateful to Professor A. Zichichi and Professor L. Cifarelli for their support to my work; they also made possible my permanence at CERN.
I would like to thank the group I have been working with during the period I spent at CERN, under the experienced guide of Dr. M. C. Williams and the help of Dr. R. Zuyeuski, Dr. O. Maragoto Rodriguez and Dr. Z. Liu.
Last but not least, many thanks to Dr. Cartiglia (with FBK's partnership) and the other members of the group, Dr. M. Mandurrino, Dr. V. Sola, Dr. M. Ferrero, Dr. F. Cenna, Dr. R. Arcidiacono and Dr. A. Staiano, for the productive collaboration.